Ulm University

Institute of Applied Physiology

Director: Prof. Dr. Birgit Liss

Functional Consequences of Two Critical Point Mutations in the Skeletal Muscle Excitation-Contraction Coupling Complex

Dissertation submitted to obtain the doctoral degree of

Human Biology (Dr.biol.hum.)

at the Medical Faculty of Ulm University

Yuan Pan

born in Nanjing, China

2019

Acting Dean: Prof. Dr. Thomas Wirth

1st Reviewer: PD Dr. Werner Melzer

2nd Reviewer: Prof. Dr. Manfred Frick

Date of Graduation: 25.10.2019

Contents

List of Abbreviations

ACH	Acetylcholine
AID	α-interaction-domain
AM	Acetoxymethyl (ester)
4-AP	4-Aminopyridine
APP	Atypical periodic paralyses
ATP	Adenosinetriphosphate
BAPTA	1,2-Bis(o-aminophenoxy)ethane-N,N,N′,N′-tetraacetic acid
BTS	N-benzyl-p-toluene sulphonamide
CaMKII	Ca^{2+}/calmodulin-dependent protein kinase II
CCD	Central core disease
CICR	Calcium-induced calcium release
4-CMC	4-Chloro-m-cresol
CPA	Cyclopiazonic acid
Cryo-EM	Cryo-electron microscopy
CSQ	Calsequestrin
DHPR	Dihydropyridine receptor
ECC / e-c coupling	Excitation-contraction coupling
ECCE	Excitation-coupled Ca^{2+} entry
EGTA	Ehylenglycol-bis-(2-aminoethyl)-N,N,N',N',tetraacetic acid
EK	E1014K mutation in $Ca_V1.1$
ER	Endoplasmic reticulum
FBS	Fetal bovine serum
GK	Guanylate kinase
HEPES	4-(2-Hydroxyethyl)-1-piperazineethanesulfonic acid
IVCT	In-vitro contracture test
JP	Junctophilin
K_D	Dissociation constant
KI	Knock-in
KO	Knock-out
K_{off}	Dissociation rate constant
K_{on}	Binding rate constant
L-type	Long lasting calcium channels
MH	Malignant hyperthermia
MHS	Malignant hyperthermia susceptibility

MmD	Multiminicore disease
NC / ncDHPR	Non-conducting / non-conducting dihydropyridine receptor
NCX	Sodium-calcium exchanger
PMCA	plasma membrane calcium ATPase
RNS	Reactive nitrogen species
ROS	Reactive oxygen species
RyR	Ryanodine receptor
SEM	Standard error of the mean
SERCA	Sarco/endoplasmic reticulum Ca^{2+}-ATPase
SF	Selectivity filter
SOCE	Store-operated calcium entry
SR	Sarcoplasmatic reticulum
STIM1	Stromal interaction molecule 1
TC	Terminal cisternae
TEA	Tetraethylammonium
TEM	Transmission electron microscopy
TEVC	Two electrode voltage clamp
TRPC	Transient receptor potential channel
TT / T-tubule	Transverse tubule
TTX	Tetrodotoxin
VSD	Voltage-sensing domain
WT	Wild-type
YFP	Yellow fluorescent protein
YS	Y522S/Y524S mutation in the RyR1

Declaration

Parts of this dissertation have been published in the following journal article:

Dayal A, Schrötter K, Pan Y, Föhr K, Melzer W & Grabner M (2017). The Ca^{2+} influx through the mammalian skeletal muscle dihydropyridine receptor is irrelevant for muscle performance, Nature communications 8, 475.

Available online: https://doi.org/10.1038/s41467-017-00629-x

1 Introduction

1.1 Skeletal muscle anatomy

Skeletal muscle is a type of striated muscle which can be voluntarily controlled by the nervous system. It is one of the three major muscle types besides cardiac and smooth muscle. It serves great importance to multiple body functions. In human, skeletal muscle makes up about 40% of the total body weight. It converts chemical energy to mechanical forces. (Frontera and Ochala, 2015)

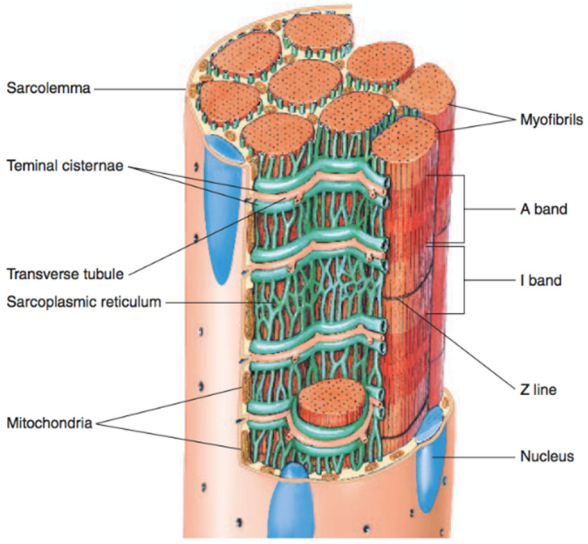

Figure 1: The skeletal muscle cell anatomy (figure from Fox, 2004, p. 338).

At the structural level, skeletal muscle consists of many muscle fibers (muscle cells), which are the basic units of a muscle as shown in Figure 1. A muscle cell still contains many chains of myofibrils. Myofibrils are composed of proteins including actin, myosin, and titin, and some others. The long proteins are organized into thick and thin filaments, which form the repeating contractile units – sarcomeres. A sarcomere is the segment between two Z-lines. Inside of a muscle cell, multiple nuclei and a network of mitochondria are bounded by the external membrane sarcolemma. Sarcolemma goes deeply into the cell by the network of transverse (T-) tubules which are the key to the travel of action potential along the sarcolemma. The Ca^{2+} storage organelle in muscle fiber is the sarcoplasmic reticulum (SR). It is also responsible for Ca^{2+} release and re-uptake upon activation. In skeletal muscle, two terminal cisternae (TC), which are enlarged parts of the SR and one transverse tubule form a triad. A triad is a functional unit of Ca^{2+} release when receiving a stimulus from the motor neuron (Ackermann, 2002).

1.2 Excitation-contraction coupling in skeletal muscle

Excitation-contraction coupling (e-c coupling) is the sequence of events which start with an action potential (an electrical event) in the sarcolemma of the muscle cell, activating the Ca^{2+} transient which initiates the cross-bridge force production (a mechanical event) (Cech and Martin, 2012; Donatelli, 2007). In the resting state, Ca^{2+} is stored in the SR, mainly in its terminal cisternae that are adjacent to the T-tubules. There are Ca^{2+} release channels located in the membrane of SR called ryanodine receptors (mainly RyR1 in mammalian skeletal muscle). The sarcoplasmic signal to initiate contraction is an elevated concentration (to above 10^{-6} M) of Ca^{2+}. The initiation of e-c coupling is when action potential in motor neuron releases acetylcholine (Ach), a neuron transmitter, to the myoneural junction. Acetylcholine then binds to the nicotinic Ach-receptors causing a local depolarization, the so-called end-plate potential. When the depolarization is large enough to activate the voltage-gated Na^{+} channels, an action potential is generated. The action potential propagates on the sarcolemma and deeply into the muscle cells along the T-tubules. Dihydropyridine receptors (DHPR), a type of voltage-gated L-type Ca^{2+} channel located in the T-tubules, are activated by the action potential. Through the mechanical coupling between the DHPR and RyR1, the ryanodine receptors are activated to release Ca^{2+} from the SR to the sarcoplasm. Free Ca^{2+} binding to troponin enables the cross-bridge cycle that eventually leads to muscle contraction. There are Ca-ATPase pumps in the plasma membrane and SR membrane (SERCA) responsible for removing the Ca^{2+} from the cytosolic space. When the action potential is over, the cytosolic Ca^{2+} concentration drops again, and muscle relaxation occurs. (Fox, 2004)

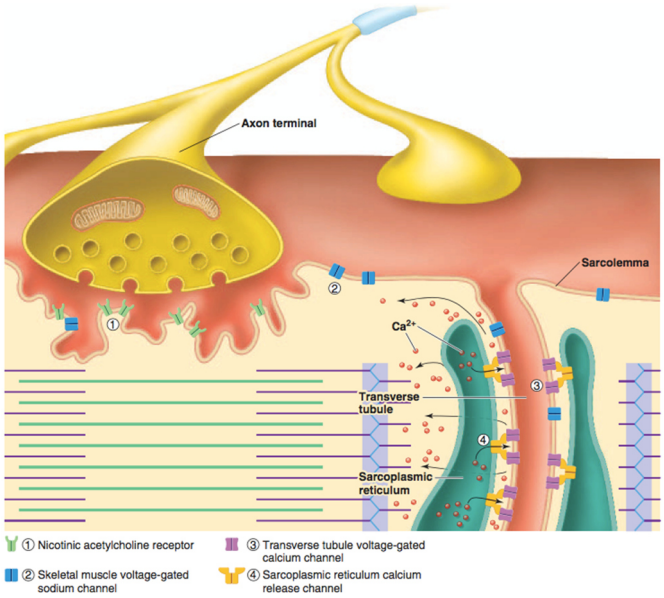

Figure 2: Some major players involved in excitation-contraction coupling (figure from Fox, 2004, p. 339).

It was known since the 1970s that e-c coupling in skeletal muscle requires no extracellular Ca^{2+} entry (Armstrong et al., 1972) but relies on the outward movement of the gating charge particles (Schneider and Chandler, 1973). It is further supported by research that showed failed e-c coupling from primary myoblast culture of late-fetal and new-born animals in a lethal dysgenic mouse line lacking slow Ca^{2+} current (Beam et al., 1986). It was also demonstrated that dihydropyridine antagonist nifedipine inhibited both the charge movement and e-c coupling (Ríos and Brum, 1987). When the expression of $Ca_V1.1$ was reintroduced into dysgenic (DHPR-null) myotubes, the L-type current, charge movement, and e-c coupling were all restored (Adams et al., 1990; Tanabe et al., 1988). The unique mechanism of skeletal muscle e-c coupling relying on the conformational change of the DHPR and RyR1 rather than the entry of extracellular Ca^{2+} is also called conformational coupling.

The structural link between DHPR and RyR is supported by the freeze-fracture studies showing that DHPRs are organized in tetrads as in Figure 3, i.e., groups of four DHPRs located at the corners of small squares (Block, 1988; Takekura et al., 1994). The arrangement of tetrads and RyR in developing junctions indicates that incorporation of DHPRs in junctional domains of the surface membrane proceeds gradually and is highly coordinated with the formation of RyR arrays. The incorporation of individual DHPRs into tetrads occurs exclusively at positions corresponding to alternate feet (Figure 4), suggesting that the assembly of RyR arrays not only guides the assembly of tetrads but also determines their characteristic spacing in the junction (Protasi et al., 1997).

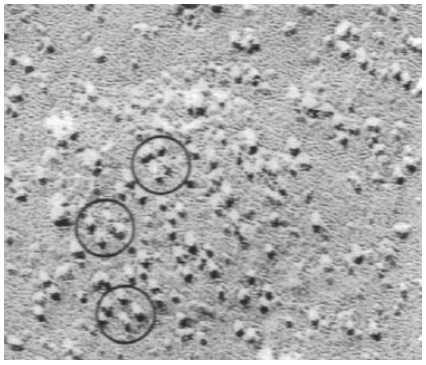

Figure 3: Electron microscopy image showing DHPR tetrads (in black circles). (Figure from Takekura et al., 1994, p. 798.)

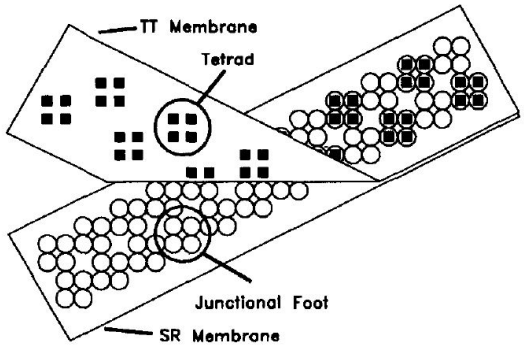

Figure 4: Arrangement of the key e-c coupling proteins in the junction. The ryanodine receptors form a double row array, with every second homotetramer coupled to a DHPR tetrad cluster. (Figure from Melzer et al., 1995, p. 63.)

DHPR needs to be appropriately targeted to the triad junction with the correct spatial orientation. A study demonstrated that the average distance between centers of each adjacent DHPR within a tetrad (~19.5 nm) is decreased by ~2 nm upon application of ryanodine at a concentration (500 μM) and duration sufficient to lock RyR1 in a sub-

conducting state (Paolini et al., 2004). Thus, the functional state of RyR1 is reflected in the spatial orientation of the DHPRs within a tetrad, a phenomenon that strongly indicates the existence of a physical coupling between RyR1 and the DHPR (Bannister, 2007).

However, the complete mechanism of conformational coupling is still unclear. There are a number of studies that aim to tackle this question (Figure 5). The α_{1s} subunit of the DHPR is a critical player in skeletal EC coupling, especially the II-III loop, the linker between 2nd and 3rd repeats, is found to be indispensable (Tanabe et al., 1990). Chimera studies identified the sequence spanning residues 720-765 in the center of the loop as "critical region" for this function (Nakai et al., 1998b; Wilkens et al., 2001). Kugler and colleagues suggested that residues 744-751 within the "critical region" form a random coil rather than an α-helix, which could undergo a rapid structural change following charge movement, enables a rapid conformational coupling (Bannister and Beam, 2013; Kugler et al., 2004). The location of this region is further confirmed by inserting fluorescent markers into the loop (Bannister et al., 2009a). The carboxy-terminal portion of the loop which connects the critical region and Repeat III is also a key structure. When yellow fluorescent protein (YFP) was introduced at either residue 760 or 785, e-c coupling was eliminated despite a rather normal channel expression and the apparent retention of the structural integrity of the critical domain. (Bannister et al., 2009a)

It was also identified that the I-II loop of $Ca_V1.1$ is the site for interaction with the β_{1a} subunit, which supports membrane trafficking and is required for skeletal e-c coupling as well (Gregg et al., 1996; Strube et al., 1996). In the β_{1a}-null zebrafish model, the "relaxed" mutant cells had reduced expression of the α_{1s} subunit in addition to no charge movement or tetrad formation of the DHPRs. In other words, the e-c coupling was disrupted (Schredelseker et al., 2005). The tetrad structure and e-c coupling were restored by expression of β_{1a}. It has been suggested that β_{1a} is essential for proper alignment between DHPR and RyR1 (Schredelseker et al., 2009).

Lately, five junctional proteins ($Ca_V1.1$, RyR1, β_{1a}, Stac3, and junctophilin2) have been identified to be the minimal necessary set of proteins to facilitate the skeletal muscle conformational e-c coupling. Voltage-dependent Ca^{2+} release was observed in tsA201 cells, a non-muscle cell line, expressing the five proteins (Perni et al., 2017). Tetrad arrangement of the $Ca_V1.1$was also observed in these cells, supporting the structural link between $Ca_V1.1$ and RyR1.

The unique conformational coupling between skeletal DHPR and RyR1 is bidirectional (Figure 6). Orthograde signals are transmitted from the voltage sensor (DHPR) to the Ca^{2+} releasing channel (RyR1). Retrograde signals are mediated by RyRs and affecting the

DHPR. The first retrograde mechanism was observed by Nakai and colleagues in a dyspedic (RyR1-null) mouse model. The RyR1-null myotubes demonstrated no e-c coupling, and curiously, a 30-fold reduction in L-type Ca^{2+} current density. By injecting the RyR1 cDNA, both e-c coupling and L-type current were restored. Charge movement measurements showed that the densities of DHPRs in dyspedic and RyR1-expressing myotubes were similar despite the largely reduced Ca^{2+} current in the dyspedic cells (Nakai et al., 1996). The retrograde signal can affect the activation kinetics of the $Ca_V1.1$ (Sheridan et al., 2006) and is dependent on the integrity of the critical domain in the II-III loop (Grabner et al., 1999).

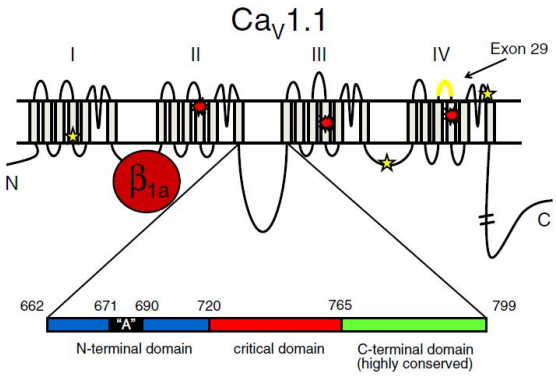

Figure 5: Components of $Ca_v1.1$ that are involved in conformational coupling (figure from Bannister and Beam, 2013, p. 1588). $Ca_v1.1$ consists of four repeats (I, II, III and IV), each containing 6 transmembrane α-helices. The I-II linker is responsible for interactions with β_{1a} subunit. The red box in the II-III linker represents the "critical domain" (residue 720-765) which is essential for e-c coupling (Grabner et al., 1999; Nakai et al., 1998b). The black box within the blue box represents the "A domain" (residues 681–690), which is required for triggering Ca^{2+} release (El-Hayek et al., 1995). The black box within the blue box represents the "A domain" (residues 681–690), which is required for triggering Ca^{2+} release (Bannister et al., 2009a). The yellow section in the S3-S4 linker of repeat IV is the location of the splice variant (Exon 29) with high Ca^{2+} conductance and voltage sensitivity (Tuluc et al., 2009). The red stars indicate positions of the mutations known for hypokalemic periodic paralysis (R528H, R900H, and R1239H). And the yellow stars indicate mutations linked to malignant hyperthermia susceptibility (R174W, R1086H/C/S and T1354S).

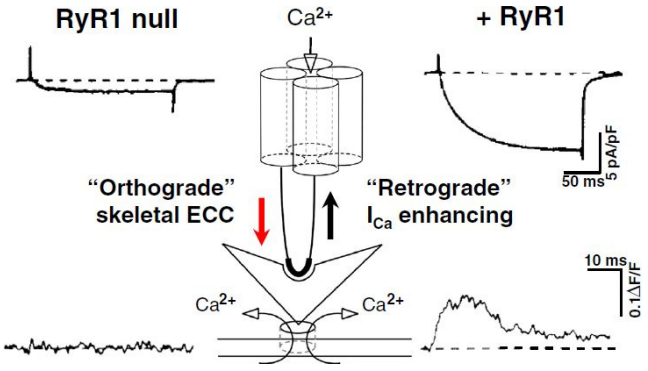

Figure 6: : Bi-directional communications between DHPR and RyR1 (figure from Bannister and Beam, 2013, p. 1591).

1.3 Cytosolic Ca^{2+} homeostasis

Ca^{2+} ions play an essential role in a variety of cellular processes, thanks to the accurate regulation of Ca^{2+} concentration mediated by different Ca^{2+} channels, transporters, exchangers, binding proteins and pumps (Murray et al., 1998). In skeletal muscle, the elevation of the cytosolic Ca^{2+} concentration initiates the cross-bridge cycle to generate a muscle contraction. In contrast, a low level of cytosolic Ca^{2+} is critical for muscle relaxation (Melzer et al., 1995). Therefore, tight control of Ca^{2+} homeostasis is of great importance to normal skeletal muscle functions. Dysregulations in Ca^{2+} entry, release or uptake mechanisms often lead to pathophysiological consequences (Vallejo-Illarramendi et al., 2014). A schematic view of the Ca^{2+} signaling in the muscle fiber is shown in Figure 7.

Store-operated Ca^{2+} entry (SOCE) and excitation-coupled Ca^{2+} entry (ECCE) are two distinct mechanisms of extracellular Ca^{2+} entry across the sarcolemmal membrane. SOCE is activated upon depletion of the Ca^{2+} store (Kurebayashi and Ogawa, 2001), relying on STIM1 to monitor the Ca^{2+} level in the SR (Zhang et al., 2005). Orai1, which was suggested to be conformationally coupled to STIM1 mediates the SOCE Ca^{2+} entry (Dirksen, 2009; Prakriya et al., 2006). ECCE, however, does not depend on Ca^{2+} store depletion and is triggered by depolarization of the plasma membrane (Cherednichenko et al., 2004). It requires the structural integrity of both DHPR and RyR1 to accommodate ECCE (Cherednichenko et al., 2004; Dirksen and Beam, 1999). SOCE can be regarded as an inside-out signaling pathway and ECCE as outside-in.

In mammalian skeletal muscle, a small amplitude of Ca^{2+} influx also known as L-type Ca^{2+} current is present during e-c coupling. However, the functionality of this influx is not understood so far. There have been a few speculations: it might contribute to ECCE and participate in maintaining Ca^{2+} homeostasis (Bannister et al., 2009b); or is involved in skeletal muscle development by regulation of acetylcholine receptor pre-patterning and formation of the neuromuscular junctions (Chen et al., 2011). Alternatively, it might have a negative inotropic effect, which is crucial for muscle health (Menezes-Rodrigues et al., 2013). It might also simply be an evolutionary remnant without particular function (Bannister, 2016; Dayal et al., 2017; Schrötter et al., 2016).

Calcium-induced calcium release (CICR) is a process that activates massive Ca^{2+} release from the SR by Ca^{2+} alone, for instance, the Ca^{2+} influx through DHPR, without any other stimulations (Endo, 2009). It was first discovered in skinned frog skeletal muscle fiber (Endo et al., 1970; Ford and Podolsky, 1970), and later found to be non-significant in physiological Ca^{2+} release in skeletal muscle (Baylor and Hollingworth, 1988; Pape et al., 1995). However, it is of importance to the e-c coupling in cardiac and smooth muscles of most vertebrates

(Bers, 2002). From the evolutionary point of view, CICR is phylogenetically ancient, because it is found in invertebrates and protochordates (Hagiwara et al., 1971; Inoue et al., 1994; Takekura and Franzini-Armstrong, 2002). A transition from randomly arranged DHPRs to the tetradic positioning of the DHPRs was also observed and thought to be associated with the evolution of the skeletal type e-c coupling (Di Biase and Franzini-Armstrong, 2005). The tetrad arrangement of DHPRs is an indication of direct protein-protein interaction with the RyR1.

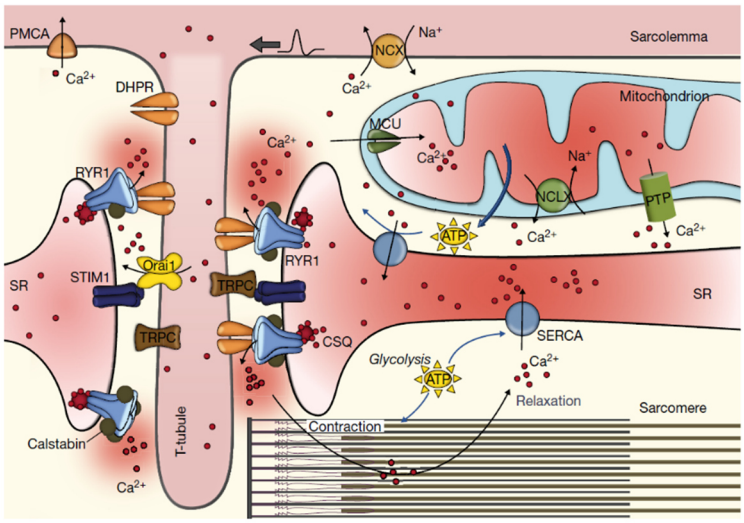

Figure 7: Participants in Ca^{2+} signaling in the muscle fiber (figure from Vallejo-Illarramendi et al., 2014, p. 3). Upon depolarization, DHPR activates RyR1 to release Ca^{2+} from the SR, accompanied by a small Ca^{2+} influx through the DHPR. Ca^{2+} returns to SR in the action of SERCA or is pumped out of the cell by NCX (Na^{+}-Ca^{2+} exchanger) or PMCA (plasma membrane Ca^{2+} ATPase) leads to muscle relaxation. STIM1 monitors Ca^{2+} level in the SR, when the Ca^{2+} store is depleted, the coupled Orai1 or TRPC channels initiates Ca^{2+} entry from extracellular space.

1.4 Dihydropyridine receptor

The dihydropyridine receptor (DHPR) located in the membrane of transverse tubules is a protein complex of about 450 kDa molecular weight. Structurally (Figure 8), DHPR is a heteromultimer consisting of 5 subunits in the stoichiometry of 1:1:1:1:1, including the voltage-gated Ca^{2+} channel $Ca_v1.1$ or α_{1s} (the skeletal muscle form), and the auxiliary subunits α_2, δ, β_{1a} and γ_1 (Campbell et al., 1988).

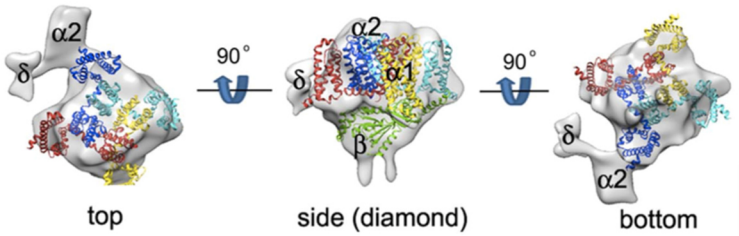

Figure 8: Spatial positions of different subunits in the DHPR (figure from Hu et al., 2015, p. 8373).

α_{1s} subunit

α_{1s} is the largest subunit (176 kDa) and constitutes both the Ca^{2+} channel pore and the voltage sensor. It can be specifically blocked by 1, 4-dihydropyridines. Like the Na^{+} channels, $Ca_v1.1$ contains 4 homologous repeats, each consisting of 6 transmembrane helices (S1-S6). Each repeat is connected to the next by a cytoplasmic loop. Transmembrane helices S5, S6 and S5-S6-linkers from each repeat contribute to the ion-conducting pore domain, whereas S1 to S4 form 4 voltage-sensing domains (VSDs). Similar to bacterial Ca_v and Na_v channels, the selectivity filter (SF) of $Ca_v1.1$ is supported by two pore helices. The SF vestibule is constituted by the side chains of the essential glutamic acid residues (Glu^{292}, Glu^{614}, Glu^{1014}, and Glu^{1323} in the four repeats, respectively) (Yang et al., 1993). The four VSDs have similar but not identical conformations. All gating charges (voltage sensors), which are positively charged amino acid residues are located in the S4 helices of all four VSDs (Wu et al., 2016).

Two of the three cytoplasmic loops connecting each repeat of the α_1s subunit to the next are of particular importance for e-c coupling. The I-II loop between domain I and II contains a conserved, 18-residue sequence called the α-interaction-domain (AID), which is the interaction site with the β_{1a} subunit (Pragnell et al., 1994; van Petegem et al., 2004). The AID is found to have effects on multiple channel properties, including voltage-dependence, kinetics, pharmacological binding affinity (Dolphin, 2003) and others. The II-III loop on the other hand plays a substantial role in both tetrad formation of the DHPR (Takekura et al., 2004) and the bi-directional conformational coupling between the DHPR and RyR1 (Grabner et al., 1999). A critical domain in the II-III loop, a 46 amino acid sequence (α_1s residues 720-765), was found necessary for Ca^{2+} release upon membrane depolarization (orthograde coupling) (Nakai et al., 1998b). At the same time, the integrity of this region is also necessary for retrograde coupling (Grabner et al., 1999; Nakai et al., 1998a).

$\alpha_2\delta$ subunit

The $\alpha_2\delta$ subunit is an extracellular protein with a molecular weight of 170 kDa encoded by

a single gene (Calderon-Rivera et al., 2012). The δ domain is anchored to the α_2 protein with a putative transmembrane segment. CACNA2D1 encodes $\alpha_2\delta$-1, which was first found in skeletal muscle, while CACNA2D2, 3, 4 encode $\alpha_2\delta$-2, 3, 4 respectively (Dolphin, 2013). The DHPR $\alpha_2\delta$-1 isoform is the most common isoform of the $\alpha_2\delta$ subunits in skeletal muscle (Flucher et al., 2005). It is not only expressed in skeletal muscle, but also in Ca^{2+} channels in the cardiovascular system and the nervous system. The methodology of siRNA gene silencing was used to deplete the $\alpha_2\delta$-1 in cultured muscle cells and to study its function (Obermair et al., 2005). The result indicated that $\alpha_2\delta$-1 is not necessary for the e-c coupling, but it altered the activation kinetics of the L-type Ca^{2+} current. In contrast to the normal L-type Ca^{2+} current which activates very slowly with two kinetic components, $\alpha_2\delta$-1 depletion led to predominantly rapid activation. Interestingly, the $\alpha_2\delta$-1 isoform in α_{1c} had a similar effect to the channel properties but in the opposite direction: it slowed down the cardiac Ca^{2+} channel activation which normally has fast kinetics when $\alpha_2\delta$-1 was depleted in cardiac muscle.

β subunit

The β_{1a} isoform of skeletal muscle is a cytoplasmic subunit containing a core SH3 domain and a guanylate kinase-like (GK) domain (Hanlon et al., 1999). The GK-domain binds to the α_{1s} subunit at a major binding site, the α-interaction-domain (AID), located in the I-II loop connecting repeat I and II (Walker and Waard, 1998). The β_{1a}-null mice exhibit failure of e-c coupling, and the homozygous mice were not viable after birth (Gregg et al., 1996). Patch clamp experiments of β_{1a}-knockout (KO) myotubes showed that L-type Ca^{2+} currents strongly decreased (Strube et al., 1996). Schredelseker et al., 2009 studied the function of β_{1a} subunit using a paralyzed mutant zebra fish strain carrying a β_{1a}-null mutation. The mutation caused a 50% decrease in α_{1s} subunit expression; however, the remaining α_{1s} were correctly targeted in triad junctions. The failure of e-c coupling was found to be accompanied by the disrupted tetrad formation of the DHPRs. This finding provided strong indication of the direct conformational interaction between DHPR and RyR1 in skeletal e-c coupling.

γ subunit

The γ_1 subunit is expressed exclusively in skeletal muscle. γ_1 knock-out mice were generated to study the function of the γ_1 subunit in muscle physiology (Freise, 2000). It was shown that γ_1 subunit is not essential for e-c coupling. The homozygous γ_1-KO mice are viable and without any abnormal phenotypes. Experiments on muscle fibers showed that the amplitude and voltage-dependence of both L-type Ca^{2+} current and Ca^{2+} release from

the SR upon activation were not altered (Ursu et al., 2004). However, steady-state inactivation experiments showed that in γ-/- fibers, the voltage-dependence of Ca^{2+} current was right-shifted. This indicates that the role of the γ_1 subunit in skeletal muscle is to increase the voltage-sensitivity of the inactivation which limits both the Ca^{2+} influx and Ca^{2+} release in e-c coupling.

3D structure of DHPR

The DHPR structure was investigated since its first purification in 1987, but good resolution results were very difficult to achieve. A common methodology used in studying protein structures is freeze fracture – shadowing electron microscopy. In order to increase the resolution, DHPR complexes are pulled down from the TT membrane with detergent and then using Transmission electron microscopy (TEM) and single particle 3D reconstruction. Cryo-electron microscopy (Cryo-EM) is a widely used technique where the sample is cooled to cryogenic temperatures. It can record images of the protein in its frozen hydrated state and has the resolution reaches up to near atomic level (Samso, 2015). Single-particle images in different orientations are analyzed and averaged to reconstruct the 3D structure. Excitingly, in 2015 a ground-breaking 4.2 Å near-atomic resolution cryo-EM reconstruction of the rabbit DHPR was published by Wu et al. and subsequently an even higher (3.6 Å) resolution (Wu et al., 2016).

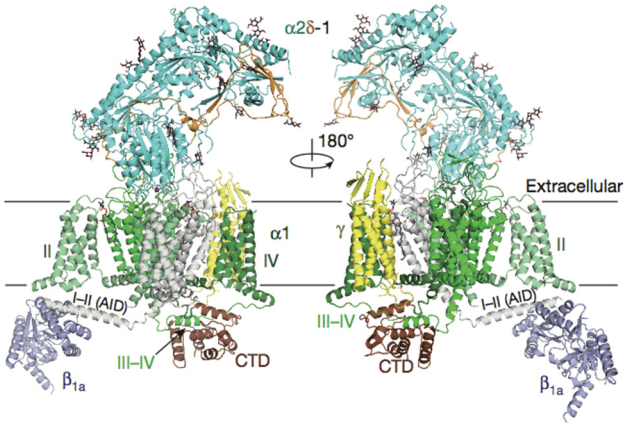

Figure 9: Near-atomic resolution of a cryo-EM reconstruction of the DHPR (figure from Wu et al., 2016, p. 192). Four homologous repeats of the α_{1s} subunit are clockwise arranged when viewed from the extracellular side. The γ_1 subunit in the cytosolic side that consisted of four transmembrane helices (TM1-TM4) interacts with the α_{1s} subunit at the VSD_{IV}. The α_2 subunit contains a von Willebrand A (VWA) domain and two Cache domains. The VWA domain and Cache1 domain interact with the extracellular loops from repeat I to III.

1.5 Ryanodine receptor

Ryanodine receptors are a kind of Ca^{2+} ion channel responsible for Ca^{2+} release from the SR/ER to the cytosol in various tissues. Ryanodine is a plant alkaloid which binds to the ryanodine receptors with high affinity and specificity (Imagawa et al., 1987; Lanner et al., 2010). Nanomolar concentrations of ryanodine keep the channel at an open sub-conductance state whereas high concentrations (>100 μM) of ryanodine inhibits the channel (Meissner, 1986). There are 3 isoforms of RyRs (1-3) found in mammals. RyR1 is primarily expressed in skeletal muscle and was the first one to be cloned (Takeshima et al., 1989; Zorzato et al., 1990), RyR2 was first found in the heart (Nakai et al., 1990; Otsu et al., 1990), RyR3 was first found in brain (Hakamata et al., 1992). All three isoforms can also be found in various other tissues. The three isoforms share 65% identity in sequence; the major differences are found in 3 regions of diversity: D1, D2, and D3 (Lanner et al., 2010).

RyR is by far the largest known ion channel with a 2.2 MDa total molecular mass. It is a homotetramer with each monomer consisting of more than 5000 amino acid residues (Nakai et al., 1990; Takeshima et al., 1989). Since its purification, many efforts have been made to study the structure of the RyRs, mostly focused on RyR1. Cryo-EM revealed that the basic architecture looks like a mushroom from the side view, with a large cap – the cytoplasmic area comprising about 80% of the volume which is also called the 'foot' region (Franzini-Armstrong, 1970; van Petegem, 2012). The corners of the cytoplasmic region are called 'clamps'; they are connected through the 'handle' domain which encloses a central ion-conducting domain called the 'central rim'. The transmembrane region and the cytoplasmic region are connected via the 'column' (Lanner et al., 2010).

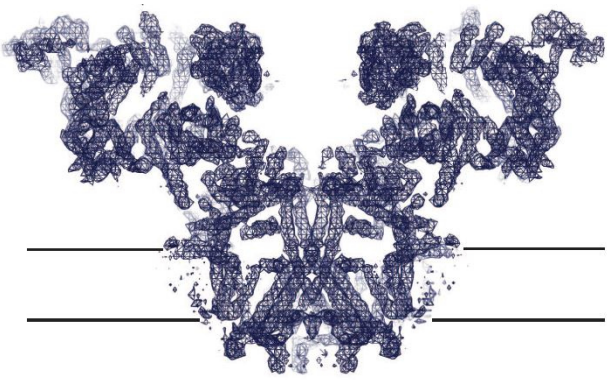

Figure 10: Density map of RyR1 at 4.8 Å viewed from the plane of the sarcoplasmic reticulum membrane (figure from Zalk et al., 2015, p. 45). Only two of the four subunits can be seen from this view, the putative position of the SR lumen is indicated between two horizontal black lines.

Regulators

The cytoplasmic region of the ryanodine receptor is responsible for interactions with many

regulators of e-c coupling. This includes small molecules such as Ca^{2+}, Mg^{2+} and ATP (Adenosinetriphosphate). Ca^{2+} regulates RyRs from both cytoplasmic side and in the SR, while Mg^{2+} and ATP modulate from the cytoplasm (Lanner et al., 2010). The activity of RyR1 on cytoplasmic Ca^{2+} concentration follows a bell-shaped dependence: low Ca^{2+} concentration (~1 μM) activates the activity of RyR1 while high Ca^{2+} concentration (~1 mM) inhibits it. This is due to the different Ca^{2+} sites with low or high affinities (Meissner, 1994, 1986). Mg^{2+} inhibits RyR activity in two ways: it can bind to the high-affinity Ca^{2+} sites to reduce RyR opening probability, and it can bind to the low-affinity inhibitory Ca^{2+} sites (Laver et al., 1997; Meissner, 1986). ATP and many other nucleotides can activate RyRs. A study showed that ATP can even activate RyR1 without the presence of Ca^{2+} (Meissner, 1984). Other regulatory partners of RyRs include calmodulin (in both Ca^{2+}-free and Ca^{2+}-bound forms), calsequestrin, traidin, junctin, FK506-binding protein (FKBP) 12 and 12.6, phosphorylation, reactive oxygen species (ROS) and reactive nitrogen species (RNS) (Lanner et al., 2010).

Human Diseases

Several human diseases are caused by mutations in ryanodine receptors. Mutations in RyR1 are known to be associated with malignant hyperthermia (MH) (MacLennan et al., 1990), heat/exercise-induced exertional rhabdomyolysis (Capacchione et al., 2010), central core disease (CCD) (Zhang et al., 1993), multiminicore disease (MmD) (Ferreiro et al., 2002) and atypical periodic paralyses (APP) (Zhou et al., 2010).

Malignant hyperthermia (MH) is a potentially life-threatening skeletal muscle disorder triggered by exposure to volatile anesthetic agents (e.g., halothane, sevoflurane, and isoflurane) and depolarizing muscle relaxants (e.g., succinylcholine) (Jurkat-Rott et al., 2000). The symptoms are elevated body temperature, metabolic acidosis, hypoxia, tachycardia, sustained and uncontrolled skeletal muscle contractions and rhabdomyolysis (Mickelson and Louis, 1996; Rosenberg et al., 2015). An MH episode is likely to be fatal if not treated immediately with the only clinically approved antidote, dantrolene (Ward et al., 1986; Zhao et al., 2001). The underlying physiological cause of MH is elevated myoplasmic Ca^{2+} concentration due to increased RyR1 channel opening (Tong et al., 1999). MH susceptibility (MHS) is when the patient has a potential risk of developing MH. However, not all MHS cases develop into MH, even after exposure to a triggering anesthetic (Dowling et al., 2014). The current “gold standard” for MHS diagnosis is the in vitro contracture testing in the presence of caffeine and halothane respectively on muscle biopsy samples (The European Malignant Hyperpyrexia Group, 1984).

Central core disease (CCD) is an inherited neuromuscular disorder, defined by areas with

reduced oxidative activity along the longitudinal axis of the muscle fiber ("central cores") and clinical features of a congenital myopathy (Jungbluth, 2007; Magee and Shy, 1956). CCD patients are also often showing positive results in MH susceptibility tests (Rosenberg et al., 2015). CCD and MH susceptibility were found to share a close genetic association. Some mutations in the RYR1 gene are responsible for both MHS and slowly progressive CCD (Denborough et al., 1973; MacLennan and Zvaritch, 2011). The majority of CCD-causing mutations are in the pore-forming domain of RyR1 (Lynch et al., 1999).

1.6 Inactivation of Ca^{2+} channel

The Ca^{2+} release in skeletal muscle shows inactivation when stimulated with a long depolarizing pulse. Further response to stimulation is only possible after the fibers are “reprimed”. Voltage-dependent inactivation in skeletal muscle has two phases, fast and slow, in terms of the rate of onset and recovery (Hodgkin and Horowicz, 1960; Nagai et al., 1979). Inactivation is tightly linked to charge immobilization, which was first measured in frog skeletal muscle (Schneider and Chandler, 1973). The steady-state voltage dependence of non-linear charge immobilization was determined by changing the holding potential (Rakowski, 1981). The charge that moves in a normally polarized fiber and is associated with Ca^{2+} release (charge 1) seems to disappear or become immobilized under long depolarization (Chandler et al., 1976). However, mobile charges (charge 2) moving in a different voltage range were discovered in depolarized fibers and suggested to be the charge of the sensor in the inactivated states (Adrian and Almers, 1976). A state diagram (Figure 11) was suggested to explain the relation between charge 1 and charge 2 (Brum and Ríos, 1987). Charge 1 would move in transitions between the resting and active states, and charge 2 would move in transitions between inactivated states. In this diagram, only the horizontal transitions are voltage dependent whereas the slow vertical transitions are voltage independent.

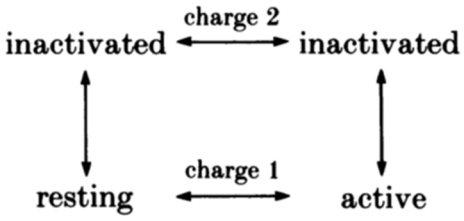

Figure 11: State diagram explaining the different inactivated states (figure from Brum and Ríos, 1987, p. 515).

Extracellular Ca^{2+} ions play a critical role in the inactivation. It was found that when external Ca^{2+} was replaced by Mg^{2+}, the Ca^{2+} release inactivation was shifted to more negative

potentials while activation remained unchanged (Brum et al., 1988b; Ríos and Brum, 1987), which couldn't be explained by the surface charge theory. When Ca^{2+} was replaced by other metal ions, the voltage sensor still functions (Pizarro et al., 1989). In the absence of metal ions in the external solution intramembrane charges only move between the inactivated states, regardless of the holding potential (-80 or 0 mV). These observations suggest that the voltage sensor requires the presence of metal cations at external binding sites in order to get reprimed and function properly (Ríos and Pizarro, 1991).

Very recently, the same concept has been confirmed in mammalian (mouse) skeletal muscle by Ferreira Gregorio et al.. The charge movement and availability measurements support that the voltage-sensing modules (VSMs) are tightly linked to the inactivation of Ca^{2+} channels in mammalian similar to the well-studied frog skeletal muscle. It was also confirmed that extracellular Ca^{2+} is required for activating Ca^{2+} release and voltage sensor charges in rodents. Unexpectedly, it was found that under physiological Ca^{2+} conditions ($[Ca^{2+}]_e$ = 1.8 mM), the voltage sensor is partially inactivated at -80 mV. The reported resting potential in rat FDB fibers ranges from -60 to -67 mV, less negative than -80 mV holding potential in the experiments (Bekoff and Betz, 1977; Pickering et al., 2009). Furthermore, to account for the hyperpolarizing shift of the voltage dependence of the charge displacement caused by removing external $[Ca^{2+}]$, a two-gate model including an extra "inactivation gate" was proposed.

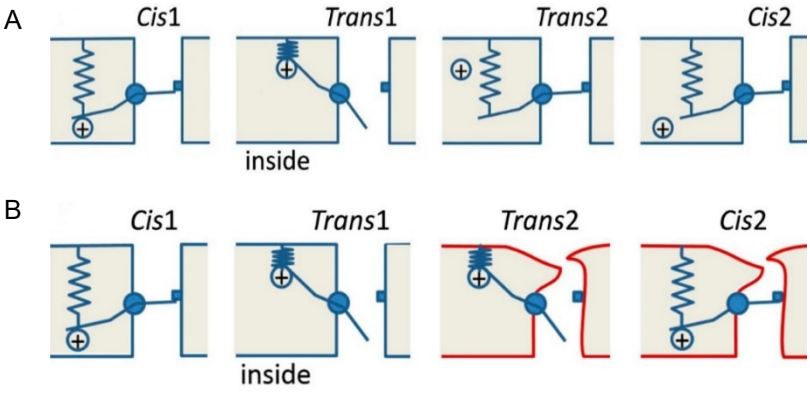

Figure 12: (A) Hypothetical single-gate model of the $Ca_V1.1$ channel. A conventional activation gate can be opened by the electric field acting on an "engaged" charged sensor. Inactivation is represented by the disengagement of sensor and gate (states 2). **(B) A two-gate model.** The inactivation "gate" is represented by narrowing of the pore at locations external to the activation gate (contours in red). (Figure from Ferreira Gregorio et al., 2017, p. 1054.)

Previous research indicated that the four glutamate residues which form the selectivity filter can bind one Ca^{2+} with high affinity when the extracellular Ca^{2+} concentration is low (10^{-3}-10^{-5} mol) and therefore block ion permeation (Almers et al., 1984). At even lower concentrations ($<10^{-5}$ mol) the channel loses its selectivity and permeates Na^+ ions. At higher concentrations ($>10^{-3}$ mol) they bind to more than one Ca^{2+} with low affinity which

allows highly selective Ca^{2+} permeation. The glutamate residues at the pore are involved in Ca^{2+} permeation, and each makes a distinct contribution to ion binding. Among them, the glutamate carboxylate in repeat III has the strongest effect. A single EIIIK mutation completely abolishes high affinity binding and Ca^{2+} permeability (Dirksen and Beam, 1999; Yang et al., 1993). Studies on voltage-gated potassium channels have shown that mutations near the pore which altered the affinities of the potassium binding sites also affected the properties of C-type inactivation of the channel (Liu et al., 1997; Lopez-Barneo et al., 1993; Yellen et al., 1994). It is reasonable to speculate that the four glutamate residues at the pore of $Ca_v1.1$ are also involved in voltage-dependent inactivation. So far, there has not been any research to change the affinity for Ca^{2+} binding to the selectivity filter by mutations to verify whether it also modifies the inactivation.

1.7 Murine models

Non-conducting DHPR mouse models

In skeletal muscle of teleost fishes, the $Ca_v1.1$ is unable to conduct Ca^{2+} current which means that in these animals the sole function of its DHPR is as a voltage sensor to trigger the RyR1 opening. Two isoforms of $Ca_v1.1$, zf-α_{1s}-a and zf-α_{1S}-b were found in zebrafish skeletal muscle, both not able to conduct the Ca^{2+} current (Schredelseker et al., 2010). The additional negative charge (aspartate) in close proximity of the selectivity filter glutamate in homologous repeat II of zf-α_{1S}-b was found to be responsible for the non-conductivity and was able to completely block Ca^{2+} conductance when introduced into the rabbit α_{1S} subunit (rb-α_{1S}) (Schredelseker et al., 2010).

Up to recently, there were no animal models available to investigate in depth the role that the L-type Ca^{2+} current plays in skeletal muscle function. Recently two mouse models with different mutations in the DHPR were created, which lead to lack of L-type current. The first one is E1014K (abbreviated EK) carrying a mutation in the DHPR selectivity filter which prevents Ca^{2+} binding and permeation (Lee et al., 2015). This mutation blocked inward L-type currents but permitted monovalent currents. The skeletal muscle of these genetically modified mice also displayed changes including an increase in fatigue, decrease in muscle fiber diameter, a shift in fiber type toward type IIb and decrease in insulin-mediated protein synthesis. These mice displayed an obese phenotype due to the disruption of the fatty acid metabolism pathway mediated by Ca^{2+}/calmodulin-dependent protein kinase II (CaMKII) which requires Ca^{2+} binding to the pore of $Ca_v1.1$ (Georgiou et al., 2015).

The mouse model, which was used in this dissertation, was generated by introducing the same selectivity-filter adjacent point mutation N617D, previously discovered to be responsible for the non-conductivity of L-type Ca^{2+} channels in zebrafish skeletal muscle (Schredelseker et al., 2010), into the mouse genome (hereafter referred to as NC for Non-Conducting). So far, no phenotype of the mice surviving and thriving into adulthood; no change in body weight development, fertility, locomotor activity, muscle fiber-type distribution, muscle strength, and fatigue has been reported. They showed unaltered e-c coupling despite the absence of the L-type current in myotubes; no transcriptional or translational regulation in major proteins that are involved in e-c coupling (Dayal et al., 2017). Current findings suggest that lack of DHPR Ca^{2+} influx doesn't play a role in muscle development and health in young and aged mice, in contrast to the findings of the EK mouse model. In this dissertation, further experiments are designed to explore the e-c coupling properties in adult muscle fibers and the inactivation of the mutant channel.

Malignant hyperthermia mouse models

Malignant hyperthermia affects not only humans but other species, for example, certain pig breeds, dogs and horses. Pigs with RyR1 mutation R615C have been for a long time the only available animal model for studies of MH (Mickelson and Louis, 1996). Two MH mouse models with mutations in RyR1 were generated and studied extensively since 2006. The R165C mouse line created by P. Allen's group carries a mutation homologous to the human mutation R163C (Yang et al., 2006). The Y524S line developed by S. Hamilton's group (hereafter referred to as YS) carries a mutation homologous to the human Y522S mutation (Chelu et al., 2006). In mice of both strains, fulminant malignant hyperthermia episodes were triggered after exposure to volatile anesthetics or following short-term heat exposure (Chelu et al., 2006; Yang et al., 2006). R163C has been found in more than 20 MH cases worldwide. The mutation displays a variable clinical phenotype in different families (Robinson et al., 2006). Y522S has been found in two MH families, both of which showed no clinical signs of muscle weakness. However, the histology analysis of the muscle samples of the patients revealed the condition of subclinical CCD (Quane et al., 1994).

The mutation Y522S was characterized as an MH/CCD mutation. In early studies, it was first introduced into full-length cDNA of the rabbit Ca^{2+} release channel (Y523 in this case), which was then expressed transiently in HEK-293 cells. The HEK-293 cells expressing the mutation showed elevated resting Ca^{2+} concentration (Tong et al., 1999). In a study that compared several RyR1 mutations expressed in myotubes, Y523S had the leakiest channels, exhibiting increased SR Ca^{2+} leak, store depletion, and a reduction in voltage-gated Ca^{2+} release (Avila and Dirksen, 2001). Soleus muscles from heterozygous Y524S

mice were examined, similar to the standard protocol of the in vitro contracture test (IVCT) in humans. Enhanced RyR1 sensitivities to activation by temperature, caffeine, and voltage were observed, but not uncompensated sarcoplasmic reticulum Ca^{2+} leak or store depletion. The homozygous Y524S mice die in the embryonic stage or postnatal day 1, which is different from the R163C mouse strain (Chelu et al., 2006; Yang et al., 2006). Although the heterozygous mice show no overt phenotype and survive well into adulthood, mitochondrial swelling/damage representing CCD could be found in their muscle fibers as early as two months of age. However, the structural damages are limited to only some areas of the fibers (Boncompagni et al., 2009).

In our group, the SR Ca^{2+} release and the L-type current of the adult muscle fibers from this mouse model were studied in detail (Andronache et al., 2009). The activation of intracellular Ca^{2+} release and intramembrane charge movement (less pronounced) displayed a shift to lower voltages. The voltage window for Ca^{2+} release that reflects the steady-state Ca^{2+} level, also left-shifted consequently. Higher temperature caused a further shift to more negative voltage of the window. Surprisingly, it was discovered that the voltage dependence of the DHPR current inactivation also was left-shifted due to a single mutation in the RyR1 gene, which serves as strong evidence of retrograde coupling.

1.8 Aims of the study

Skeletal muscle e-c coupling in vertebrates has a unique mechanism: it involves a direct protein-protein interaction between the DHPR and the RyR1, independent of the initial Ca^{2+} entry from the DHPR. After several decades of research, the role that L-type Ca^{2+} current plays in skeletal muscle physiology remains unclear and controversial. The recently generated non-conducting mouse model (NC) offers an excellent opportunity to study the long-term effect of Ca^{2+} influx in e-c coupling. The first objective of this dissertation was to gain insight into this topic using mature muscle fibers of the genetically modified murine model by monitoring Ca^{2+} release under voltage clamp conditions. Since the N617D mutation in DHPR is adjacent to the selectivity filter and alters the Ca^{2+} ion binding affinity at the pore (Dayal et al., 2017), it is also a perfect candidate to investigate the voltage-dependent inactivation according to the binding site theory.

The second part of this dissertation focuses on the malignant hyperthermia mouse model Y524S which displayed retrograde e-c coupling signals (Andronache et al., 2009). This former study reported the MH-causing mutation in the RyR1 had altered the inactivation of Ca^{2+} current as well as Ca^{2+} release mediated by the DHPR. Since the exact mechanism of

the voltage-gated inactivation of the DHPR is not well-understood, it is not clear how such a retrograde signaling pathway took place. By varying the experimental conditions of the voltage clamp protocols, the aim is to distinguish the effect of local Ca^{2+} concentration in the nearby of the Ca^{2+} release channel on current and release inactivation.

Specifically, these questions were addressed:

1) How are the Ca^{2+} release properties in mature muscle fibers of the NC mouse model?
2) Is the SR Ca^{2+} content changed in the absence of the Ca^{2+} influx in the muscle fibers from the DHPR in NC mouse model?
3) How does extracellular Ca^{2+} ion concentration affect Ca^{2+} release activation and inactivation properties?
4) Does the inactivation in NC mouse model differ from the wildtype (WT) and what can it tell about the inactivation process?
5) How does local Ca^{2+} concentration near the release channel alter the Ca^{2+} release and the steady-state Ca^{2+} level?
6) Is local Ca^{2+} concentration near the release channel involved in the retrograde pathway that altered the DHPR gating behavior?

2 Materials and Methods

2.1 Mouse models

Two transgenic murine models were used in this dissertation. The NC knock-in mouse model with C57BL/6NTac background carrying the N617D mutation in the *CACNA1S* gene was generated at the Institute Clinique de la Souris – ICS (Illkirch, France) (Dayal et al., 2017). The MH mouse model carrying YS mutation in the RyR1 gene was generated according to methods described in Chelu et al., 2006. All animals were bred and kept in a specific pathogen-free facility of the Tierforschungszentrum (Animal Research Center) at Ulm University. WT and transgenic NC mice were kept separately. YS mice were kept mixed but genotyped after weaned according to Chelu et al., 2006. Male mice aged between 18 and 34 weeks (average 24 weeks) from N617D knock-in strain and between 13 and 36 weeks (average 24.3 weeks) from wildtypes; from the YS strain, male mice ranging from 21 and 30 weeks (average 25.2 weeks) and wildtypes ranging 16 to 23 weeks (average 19 weeks) were used for experiments. All experimental procedures performed on mice were in accordance with German animal protection laws, approved by the local animal welfare committee, and conducted under the project license O.47 of the Institutional Animal Care and Use Committee of Ulm University (Tierforschungszentrum, Universität Ulm) with approval by the regional administrative authority (Regierungspräsidium Tübingen).

2.2 Muscle fiber preparation

Mice were killed by exposure to CO_2 and followed by cervical dislocation (certified by the Animal Research Center at Ulm University according to §4 Abs. 1a und 3 TschG on 03.06.2014). The hind limb toe muscles (musculi (mm.) interossei) were dissected in a Sylgard^{TM}-coated (Dow Corning, Belgium) petri-dish bathed in Krebs-Ringer solution (details see Section 2.10 “Solutions”). The dissected muscles were incubated at 37 °C with gentle shaking (100 rpm) in the dissociation solution for muscle fiber (details see Section 2.10 “Solutions”) for 60 min. After adequate washing-off of the collagenase, the enzymatically isolated single muscle fibers were cooled at 4 °C in Krebs-Ringer solution until the experiment. All experiments were carried out within 36 hours after the preparation.

A  B 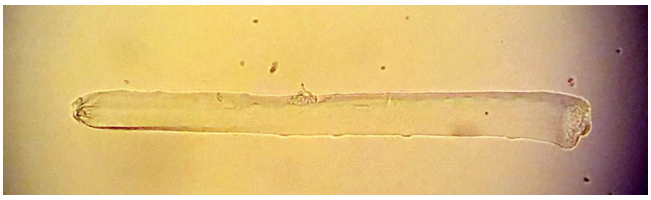

Figure 13: (A) Hind foot of the mouse during dissection of the muscle under the microscope. (Courtesy of Dr. Andronache) **(B) A representative example of muscle fiber selected for experiments (under microscope 10X lens).**

2.3 Two-electrode voltage clamp

The method used in this study was a modified version of the traditional two-electrode voltage clamp (TEVC) to control the membrane potential of mature muscle fibers. Signals to be analyzed were the L-type Ca^{2+} current and the cytosolic Ca^{2+} transients. Ca^{2+} transient measurements were recorded by using the Ca^{2+}-sensitive fluorescent indicator Fura-2. The experimental setup consisted mainly of an inverted epifluorescence microscope (Axiovert 135 TV, Zeiss) and a voltage clamp amplifier (Axoclamp 2B, Axon Instruments). The complete list of the setup elements is included in Table 1. A representative scheme of the setup system is shown in Figure 14 (Ursu, 2004).

The prepared muscle fibers were added into the experimental chamber with 1 ml external bath solution (details see Section 2.10 “Solutions”). In the external solution, tetraethylammonium (TEAOH) and 4-Aminopyridine (4-AP) are potassium channel blockers to reduce the potassium current; Tetrodotoxin (TTX) is a high-affinity sodium channel blocker to inhibit the sodium current; N-benzyl-p-toluene sulphonamide (BTS) is a myosin II ATPase inhibitor to prevent muscle fiber contractions. The Ca^{2+} concentration was increased to 10 mM instead of the physiological concentration in muscles (2.5 mM) is to augment the L-type Ca^{2+} current. The glass micropipettes were made from borosilicate glass with filament (GB150TF-10, Science Products GmbH) using a commercial puller (DMZ, Zeitz Instruments). The sharp voltage-recording electrodes had resistances between 5 and 10 MΩ when filled with 3M KCl electrolyte. The larger-opening current-passing electrodes had resistances between 1.8 and 2.8 MΩ when filled with the artificial internal solution with EGTA or BAPTA as Ca^{2+} chelator. The current-passing electrode was used to dialyze the cell. The electrodes were placed into their holders (HL-U, Axon Instruments) which connected them to the amplifier head stages. The head stages were mounted on micromanipulators that were attached to the microscope stage (Figure 15).

Table 1: A list of devices in the setup.

Name	Device/Model	Manufacturer
AD/DA Converter	CED 1400+	Cambridge Electronic Design
Bessel Filter	8 pole Bessel filter	Geitmann, Menden
FC	Filter changer	Ulm University Workshop
H1	HS-2A-x0.1LU	Axon Instruments
H2	HS-2A-x1LU	Axon Instruments
Inverted Microscope	Axiovert TV 135	Zeiss
M1	DC-micromanipulator	Märzhäuser
M2	SM3.25-Micromanipulator	Märzhäuser
PC AMD K6-2	Personal Computer	Comtech
PMT	PMT R268	Hamamatsu
RC	Plexiglas recording chamber	Ulm University Workshop
S	Shutter Uniblitz VS25	Vincent Associates
Voltage Clamp Amplifier	Axoclamp 2B	Axon Instruments
Xenon Lamp	XBO 75W	Zeiss

The fibers were first observed with a 10X/0.3 objective (Zeiss), then with 40X/0.75W objective (Zeiss) when the electrodes were in close distance to the cell. The command voltage was set to -80 mV with minimum amplifier gain (30) when the voltage-recording electrode was inserted in the cell. Then the current-passing electrode was gently sealed to the cell membrane, and the amplifier gain was set to 800 for the duration of each experiment. An 8-pole Bessel filter (Geitmann) was used for low-pass filtering at 500 Hz before input to the analog-digital converter to avoid aliasing effect according to Nyquist–Shannon sampling theorem.

All electrophysiological and fluorescent data were recorded simultaneously at 2 kHz sampling frequency, except for the capacitance measurement at 10 kHz, using a CED 1401+ interface connected to an AMD K6-2 computer. A home-written software in Delphi 3 (Borland International) named *Clamprec* by Dr. Daniel Ursu was used for data acquisition.

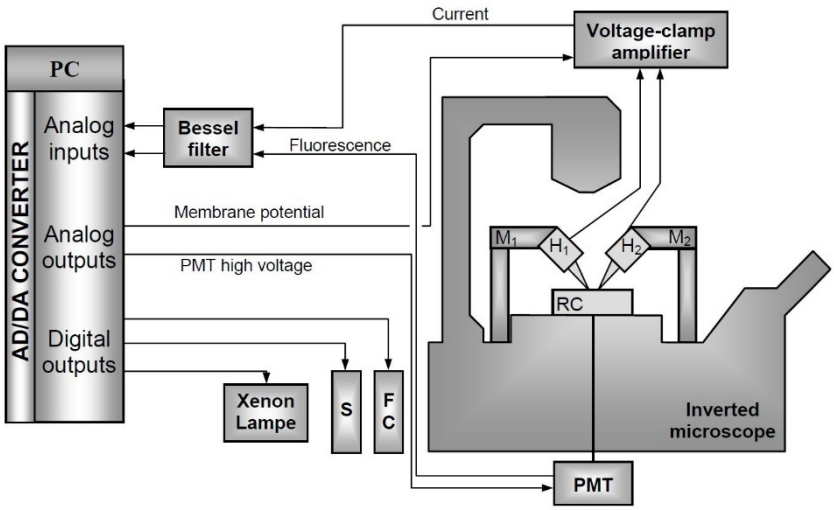

Figure 14: Scheme of the voltage clamp setup system for TEVC (Ursu 2004, 28).

Table 2: Parameters used in the puller to produce both micropipettes. P(A)01 (single-pull program) was used for sharp pipettes, and P(A)18 & P(B)18 (multi-pull program) were used for large-opening pipettes.

Parameters	P(A) 01	P(A) 18	P(B) 18	Parameters	P(A) 01	P(A) 18	P(B) 18
Heat	500	300	300	Delay Pull 1	155	200	170
Force Prim. Pull	100	80	50	Force Pull 1	250	---	380
Distance Threshold	60	14	3	Distance Pull 2	50	004	060
Delay heatstop	60	---	50	Force Pull 2	700	000	200
Distance heatstop	0	300	0	Adjust	---	020	020

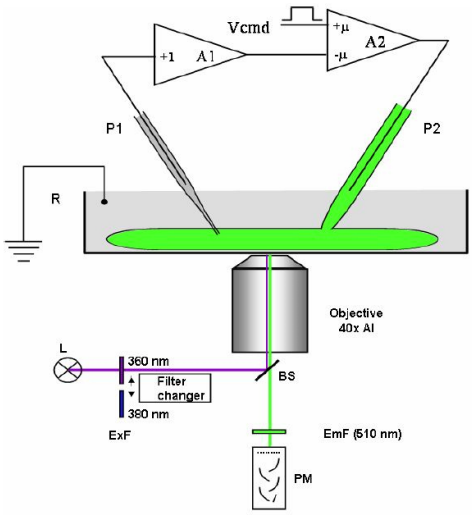

Figure 15: Abstract scheme of the voltage clamp and fluorescent measurement setup (Ursu 2004, 30).

2.4 Fluorescent recordings and indicators

The fibers were loaded with the Ca^{2+} indicator Fura-2 during dialysis with the artificial internal solution from the current-passing electrode. The light path for the fluorescence excitation starts from the xenon lamp (XBO, 75 W), then an electromagnetic shutter (S) controlled by the computer program allows the light to pass when the measurement was taking place. Next, a home-made electromagnetic filter changer (FC) was used to switch between two excitation wavelengths using interference filters 380.1/14.8 and 358.2/9.2 (Schott, Mainz, Germany). A dichroic beam splitter (BS, FT460, Zeiss, Oberkochen, Germany) was used to guide the excitation light to the fiber via the objective (Neofluar 40 W.I. 0.75, Zeiss) and the emission light (510 nm) from the fiber to the photomultiplier. A photomultiplier system (PMT) was attached to the bottom output of the microscope to collect the emission signals, which was first filtered by a 510 nm bandpass interference filter (510W B40 Omega Optical, Brattleboro, VT, USA).

Fura-2 was used in all two-electrode voltage clamp experiments. It is a commonly used, UV-excitable, ratiometric Ca^{2+} indicator. The excitation spectrum (Figure 16 A) shifts upon binding to Ca^{2+}, which allows ratiometric detection of the intracellular free Ca^{2+} concentration. At its isosbestic point (about 360 nm), the fluorescence intensity is independent of the Ca^{2+} concentration. Emission at 510 nm was monitored at two excitation wavelengths, 360 and 380 nm. By calculating the ratio F_{380}/F_{360}, free Ca^{2+} concentration can be determined reliably regardless of the dye concentration. The dissociation constant K_D of Fura-2, determinded as 276 nM by (Schuhmeier et al., 2003), was used to calculate the intracellular Ca^{2+} concentration using the following equation:

$$[Ca^{2+}] = K_{D,fura} * \left(\frac{\frac{1}{k_{off,fura}} * \frac{dR}{dt} + R - R_{min}}{R_{max} - R} \right) \quad (1)$$

Here R_{min} and R_{max} are the limiting ratios of two extreme conditions: no Ca^{2+} and an excess amount of Ca^{2+} causing full dye saturation respectively. They were calibrated on the same setup by earlier researchers; the values used are R_{min} = 3.53, R_{max} = 0.41 (Ursu, 2004). It is important to note that, with increasing [Ca^{2+}] the ratio F_{380}/F_{360} decreases.

Fura-FF is an analog of Fura-2, also a ratiometric Ca^{2+} indicator. Its excitation spectrum (Figure 16 B) and emission wavelength are similar to Fura-2, therefore, the same filters can be used in measurements with Fura-FF. However, its affinity to Ca^{2+} binding is much lower than Fura-2 with K_D ~ 5.5 µM (Molecular Probes, Paredes et al., 2008. It is used to measure the high concentration of Ca^{2+} or in cells that have relatively low Ca^{2+} buffering capacities.

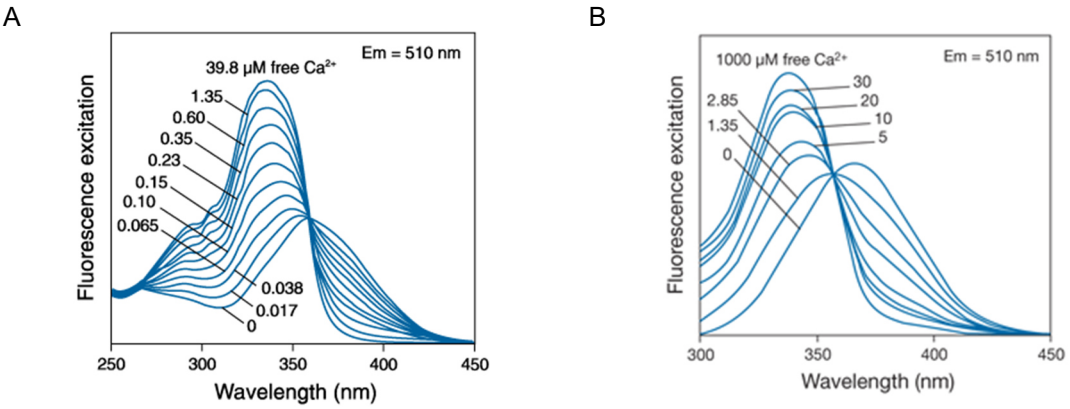

Figure 16: (A) Fluorescence excitation spectra of Fura-2 in solutions containing 0 – 39.8 µM free Ca^{2+}. **(B)** Ca^{2+}-dependent fluorescence excitation spectra of Fura-FF (Thermo Fisher Scientific)

2.5 Ca^{2+} current analysis

The raw current data from the voltage clamp measurement contains several components. The command voltage was rounded by an 8-pole Bessel filter, a low pass filter at 500 Hz. Analog compensation was performed to decrease the leak and capacitive current components before the digital data acquisition. The interpretation of the Ca^{2+} current was done by R scripts. The measurements within the last 9 ms of the depolarization pulse in each trace were averaged as the current data point of the given voltage (Figure 17). The voltage-dependence of the current data was fitted to the following equation consisted of a linear leak current and a voltage-dependent component:

$$I(V) = G_{leak} * (V - V_{leak}) + \frac{G_{Ca}(V - V_{Ca})}{1 + e^{(V_h - V)/k}} \quad .(2)$$

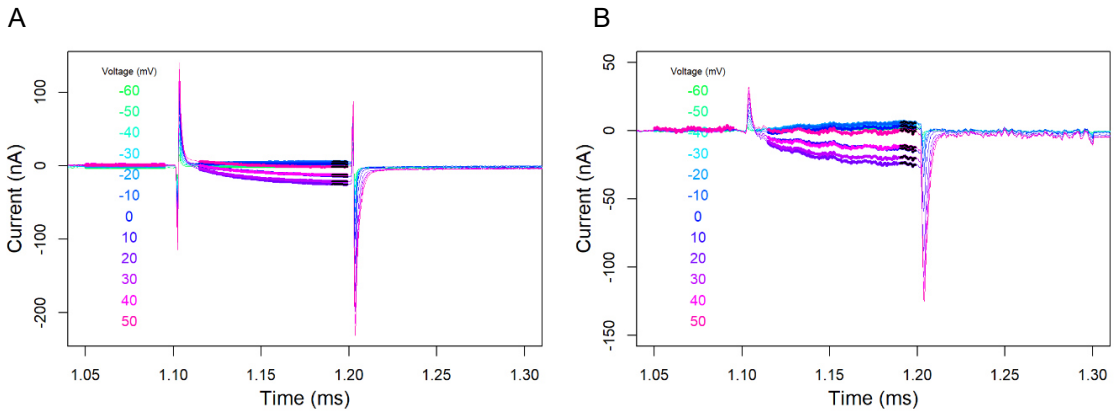

Figure 17: An example of the leak and capacitance current correction by R. (A) the traces in different colors represent raw current recordings at different test voltages. **(B**) the current traces after leak and capacitance corrections are shown. The average value at the end of the test pulse which is marked black was used to generate the current voltage plot in Figure 18.

The leak current component is assumed to be linear with voltage; G_{leak} and V_{leak} are the conductance and reversal potential of the leak current. The Ca^{2+} current was calculated as the total measured current subtracting the leak current activation, assumed to follow Boltzmann function:

$$I_{Ca^{2+}}(V) = \frac{G_{Ca}(V - V_{Ca})}{1 + e^{(V_h - V)/k}} \quad , (3)$$

where G_{Ca} and V_{Ca} are the conductance and reversal potential of the Ca^{2+} current, V_h is the half maximal voltage of the Ca^{2+} current, and k describes the steepness of the Boltzmann function. The averaging and fitting steps were done by a R (R Core Team, 2017) analysis script, as shown in Figure 18.

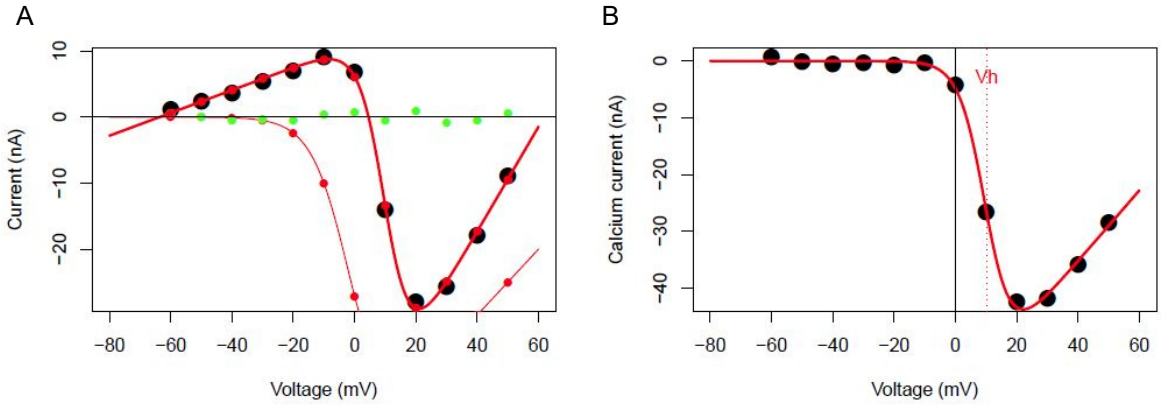

Figure 18: An example of the linear leak current correction by R. (A) The black circles represent the total current measurement points, the bold red line connecting the black circles is the fit to the measured points according to Equation . (2 **)**. The smaller red circles and thin red line represent the data points and fit after the correction, respectively. The light green circles are the residue leak current offset after the linear subtraction. **(B) T**he corrected current data points and the fit according to Equation , (3 **)** are shown in black circles and red line respectively. The red dashed line indicates the V_h value in the equation.

2.6 Current density calculation

In order to normalize the Ca^{2+} current amplitude to the size of the muscle fiber, the capacitance of the cell must be calculated to convert the current to current density (i_{Ca}). Capacitance analysis was performed as shown in Figure 19. From -80 mV holding potential, two sets of alternating depolarizing and hyperpolarizing small pulses (±10 mV) of 50 ms duration were applied. The sampling rate of data collection in the capacitance measurements was 10 kHz. A R script was used to determine the capacitance values automatically using the ON response of the depolarizing traces. The integral of the slope-corrected current data is the electrical capacitance of the cell. Finally, Ca^{2+} current density is Ca^{2+} current normalized to the capacitance of each individual fiber.

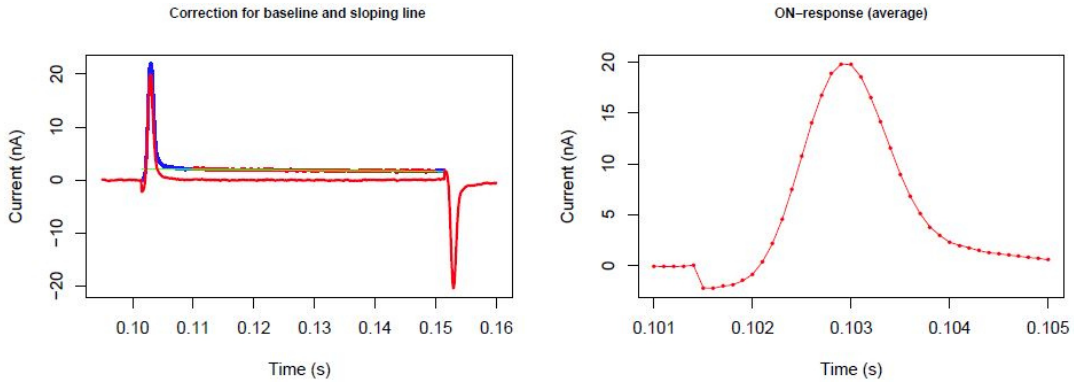

Figure 19: The cell electrical capacitance calculation done by R. In the left panel, the current response of the cell under 10 mV depolarizing pulse is shown in blue trace; a sloping line fit was done in the time range 0.11 – 0.15 s shown in thin green line; the corrected current is the total current subtracting the slope line shown in red trace. In the right panel, the corrected ON-response current is shown at a different time scale. The capacitance is determined as the integral from 0.1015 – 0.105 s.

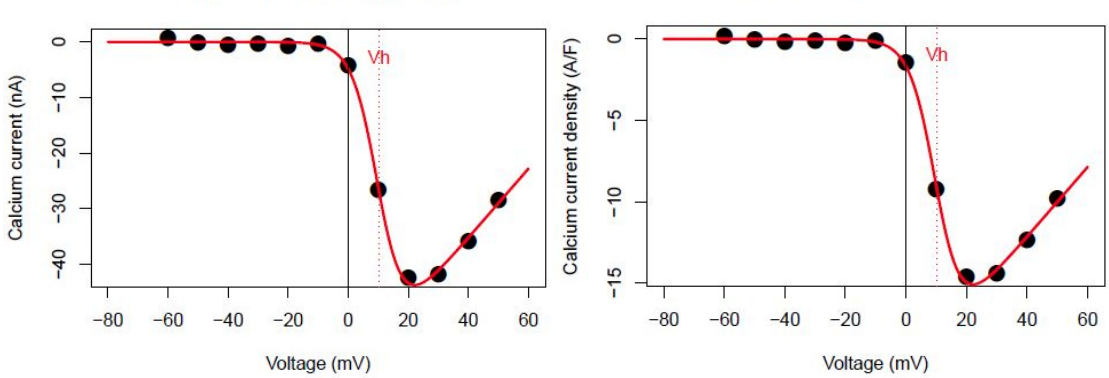

Figure 20: The conversion from current (left) to current density (right) by R.

2.7 Ca^{2+} transient and flux analysis

In order to obtain information about Ca^{2+} transient and flux in experiments, the recorded data of F_{360} and F_{380} needed to undergo several steps of analysis. First of all, the background fluorescence had to be subtracted before calculating the ratio of F_{380}/F_{360}. The background determination was done automatically by a R script. Background intensity of F_{360} and F_{380} were determined independently by fitting linear regression models to the rising part of the signals. Both signals were initially high due to the diffusion of the internal solution from the pipette to the surrounding of the cell. After the washout with external solution flow, the signals dropped to the lowest point and then slowly increased due to the diffusion of internal solution into the cell. The extension of the two fit lines at x=0 was calculated and interpreted as the background intensity. The ratio of F_{380}-$Background_{380}/F_{360}$-$Background_{360}$ was the background-corrected ratio R being used in the data analysis.

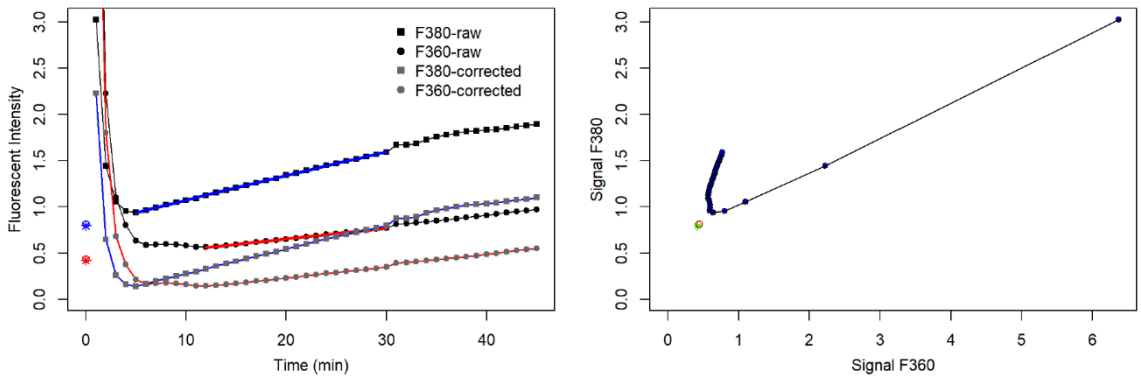

Figure 21: An example of background determination by R (file number: 14N18007). The left panel shows the raw fluorescent intensity of F_{360} and F_{380} in black symbols. The rising signals during the loading protocol (0 – 30 min) have been fitted respectively (fit line of F_{380} shown as thick blue line, that of F_{360} shown as thick red line). The extension of the linear fits at Time = 0 is the determined fluorescence background. The corrected fluorescence intensities are the raw signal with the background removed (gray symbols), which were then used to calculate the ratio F_{380}/F_{360}. The right panel shows the relative relation of F_{380} and F_{360} from the same recording. The background determined in the left panel is shown as a red circle in the right panel.

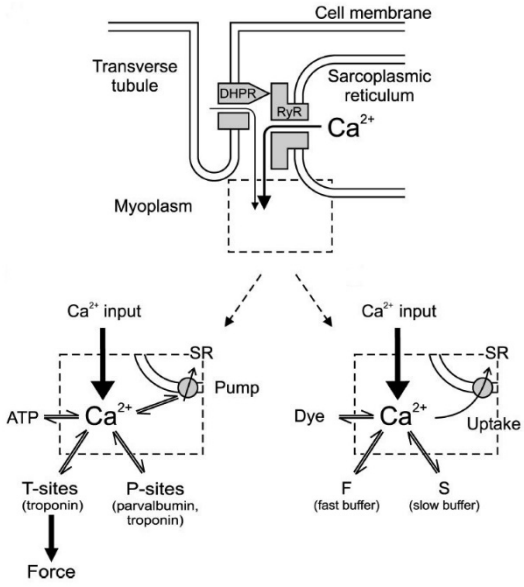

Figure 22: The released intracellular Ca^{2+} binding models with and without a dominating slow buffer (figure from Schuhmeier and Melzer, 2004, p. 36). (more detailed explanation in text below)

Although only the free cytosolic Ca^{2+} transient could be determined from the fluorescence ratios, as it shows in Figure 22, many components contribute to the removal of cytosolic Ca^{2+} in a physiological condition. For example, the fast binding sites on troponin C (T-sites), slow binding sites on troponin C and parvalbumin (P-sites), the fast Ca^{2+} binding by ATP, and binding and transport by the SR Ca^{2+}-ATPase (Baylor and Hollingworth, 1998; Jiang et al., 1999). In order to extract the Ca^{2+} influx information (Ca^{2+} input) from the measured Ca^{2+} transient, the Removal Model (Schuhmeier and Melzer, 2004) was employed to simplify the binding and transport of the released Ca^{2+}. In the experimental condition, the excess

amount of EGTA (15 mM) as slow Ca^{2+} buffer (S) completely dominated the slow binding sites. Other binding sites were the fluorescent dye, fast binding sites (F) that assumed to bind instantaneously and linearly, and the re-uptake by the Ca^{2+}-ATPase (Uptake) at a rate assumed proportional to the free Ca^{2+} concentration. The relation between them can be described by the following equation:

$$\frac{d}{dt}[Ca^{2+}]_{total} = \frac{d}{dt}([Ca^{2+}] + [Ca^{2+}Dye] + [Ca^{2+}]_F + [Ca^{2+}S] + [Ca^{2+}]_{uptake}) \quad , (4)$$

The modeling and fitting procedures were done by a home-written program named *Canalysis* developed by Dr. Ralph-Peter Schuhmeier. There were 4 free parameters in this fitting model: $k_{off,\,dye}$, $k_{on,\,S}$, $k_{off,\,S}$ and k_{uptake}. The fixed parameters were $[Dye]_{total}$ = 0.2 mM, $[S]_{total}$ = 15 mM, $K_{D,dye} = k_{off,Dye}/k_{on,Dye}$ = 0.276 µM. In the analysis of the NC data, $k_{off,\,dye}$ was fixed to 29.6591 s^{-1} due to the high noise level in the measurements. Other conditions of the removal model analysis were as following:

$$\frac{d}{dt}[Ca^{2+}Dye] = k_{on,Dye}[Ca^{2+}][Dye] - k_{off,Dye}[Ca^{2+}Dye] \quad , (5)$$

$$[Ca^{2+}]_F = F * [Ca^{2+}] \quad , (6)$$

$$\frac{d}{dt}[Ca^{2+}S] = k_{on,S}[Ca^{2+}][S] - k_{off,S}[Ca^{2+}S] \quad , (7)$$

$$\frac{d}{dt}[Ca^{2+}]_{uptake} = k_{uptake}[Ca^{2+}] \quad , (8)$$

$$[Dye] = [Dye]_{total} - [Ca^{2+}Dye] \quad , (9)$$

$$[S] = [S]_{total} - [Ca^{2+}S] \quad . (10)$$

2.8 Permeability calculation

With the removal model fit, Ca^{2+} influx can be calculated from the Ca^{2+} transient. Since the Ca^{2+} entry is negligible compared to the Ca^{2+} release from the SR in experimental conditions, the Ca^{2+} influx obtained in this dissertation was interpreted as the Ca^{2+} release. In Equation 11, the permeability of the SR (P_{SR}) is the Ca^{2+} release rate (flux $\dot{R}$) divided by the SR content in terms of myoplasmic water volume (Ca_{SR}) (assuming that the Ca^{2+} concentration build-up in the cytoplasm remains small compared to the SR content). SR content is the initial Ca^{2+} content minus the released Ca^{2+}.

$$P_{SR} = \frac{\dot{R}}{Ca_{SR}} \quad . (11)$$

In order to calculate the permeability, a depletion correction was first required. According to Schneider et al., 1987 and González and Ríos, 1993, the slower decline of the plateau phase likely results from the depletion of the SR content, whereas the permeability of the SR is assumed to stay constant during the plateau phase at a given voltage.

2.9 Chemically triggered Ca^{2+} release

Muscle fibers from mice were transferred to culture dishes with glass bottoms (P35G-1.5-14-C, MatTek Corporation) after preparation steps described in Section 2.2 “Muscle fiber preparation”. The glass bottom was pretreated with Matrigel ECL matrix at 37˚C for 30 min to achieve better adhesion for the cells. Cells were kept in the incubator (37˚C and 5% CO_2) overnight to stabilize in cell culture medium (details see Section 2.10 “Solutions”). On the day of the experiment, cells were loaded with 5 µM Fura-FF-AM (Molecular Probes) in HEPES-buffered Krebs-Ringer solution for 30 min at room temperature. After washing out the dye, cells were equilibrated with Krebs-Ringer solution containing 100 µM BTS for 30 min at room temperature to avoid contractions during measurement.

Shortly before the experiment, the bath solution was replaced by Ca^{2+} free Ringer’s solution to eliminate the potential influence of external Ca^{2+}. The selected cell was stimulated with a Ca^{2+}-releasing solution: 500 µM 4-chloro-m-cresol (4-CMC) and 30 µM cyclopiazonic acid (CPA) in Ca^{2+}-free Ringer’s solution, applied from a pipette close to the cell. At the same time, bulk flow (2 L/min) of Ca^{2+}-free Ringer’s solution is maintained to avoid contamination of other cells in the same dish. Ryanodine receptor agonist 4-CMC, together with CPA, a SERCA blocker to prevent Ca^{2+} from returning to SR, could stimulate large Ca^{2+} release signals yet still tolerable for the cells. The Ca^{2+}-releasing solution application protocol consisted of 20 s washing with Ca^{2+} free Ringer’s solution, followed by 20 s application of the Ca^{2+}-releasing solution and repeating 20 s washing.

Fura-FF-AM fluorescent signals were collected at two excitation wavelengths: 340 and 380 nm, using a Zeiss Microscope Photometer System (FFP) based on an inverted microscope (Axiovert 35, Zeiss) equipped for epifluorescence (Fluar 40X/1.3 oil immersion objective). Fura-FF was chosen for this experiment instead of Fura-2 to prevent dye saturation during large Ca^{2+} release without intracellular buffering. This series of experiments were performed in the laboratory of Dr. Karl Föhr (Department of Anaesthesiology, Ulm University, Ulm, Germany).

2.10 Solutions

Solutions play a vital role in voltage clamp and other ion channel measurements. Here is a list of all solutions (in mM) used in experiments included in this dissertation.

1. Krebs-Ringer solution: 145 NaCl (Sigma-Aldrich), 5 KCl (Roth), 1 $MgCl_2$ (Sigma), 2.5 $CaCl_2$ (Sigma), 10 HEPES (Sigma), 10 Glucose (Sigma) (pH 7.4, 0.308 Osm).
2. Dissociation solution for muscle fiber isolation: Krebs-Ringer solution containing 2 mg/ml collagenase (SERVA).
3. External bath solution containing 10 mM Ca^{2+}: 130 TEAOH (Aldrich), 130 HCH_3SO_3 (Aldrich), 2 $MgCl_2$, 10 $CaCl_2$, 5 Glucose, 10 HEPES, 5 4-aminopyridin (4-AP, Aldrich), 0.001 tetrodotoxin (TTX, Biotrend), 0.05 N-benzyl-p-toluene (BTS, Tocris) (pH 7.4, 0.298 Osm).
4. Internal solution with EGTA: 145 CsOH (Aldrich), 110 aspartic acid (Sigma), 5 Na_2 creatine phosphate (Sigma), 10 HEPES, 0.75 Na_2ATP (Sigma-Aldrich), 4.25 MgATP (Sigma), 15 EGTA (Aldrich), 1.5 $CaCl_2$, 0.2 Fura-2 pentapotassium salt (Life Technologies) (pH 7.2, 0.311 Osm).
5. Cell culture medium: 90% DMEM/F-12 (1:1) + GlutaMAX (Dulbecco's Modified Eagle Medium F-12 Nutrient Mixture, Gibco, Thermo Fisher Scientific), 10% Fetal bovine serum (FBS) and 0.2% Primocin (InvivoGen).
6. Ca^{2+}-free Ringer's solution: 145 NaCl, 5 KCl, 3.5 $MgCl_2$, 10 HEPES, 10 Glucose (pH 7.4, 0.306 Osm).
7. Ca^{2+}-releasing solution: 500 µM 4-chloro-m-cresol (Sigma-Aldrich) and 30 µM cyclopiazonic acid (Sigma-Aldrich) in Ca^{2+}-free Ringer's solution.
8. Low-Ca^{2+} external solution: 130 TEAOH, 130 HCH_3SO_3, 11.9 $MgCl_2$, 0.1 $CaCl_2$, 5 Glucose, 10 HEPES, 5 4-aminopyridin, 0.001 TTX, 0.05 BTS (pH 7.4, 0.312 Osm).
9. Internal solution with BAPTA (1,2-Bis(o-aminophenoxy)ethane-N,N,N′,N′-tetraacetic acid): 145 CsOH, 115 aspartic acid, 5 Na_2 creatine phosphate, 20 HEPES, 1.05 Na_2ATP, 3.95 MgATP, 10 BAPTA (Sigma-Aldrich), 0.2 Fura-2 pentapotassium salt (pH 7.2, 0.311 Osm). Free Mg^{2+} concentration set to 1 mM determined with a metal ion and buffer binding software CALCV31 provided by courtesy of Dr. Karl Föhr (Föhr et al., 1993).

Table 3: List of companies that chemicals and materials were obtained from.

Name of the Company	Location
Aldrich	Steinheim, Germany
Biotrend	Cologne, Germany
InvivoGen	San Diego, California, USA
Life Technologies	Carlsbad, California, USA
MatTek Corporation	Ashland, Massachusetts, USA
Molecular Probes	Eugene, Oregon, USA
Roth	Karsruhe, Germany
Science Products GmbH	Hofheim am Taunus, Germany
SERVA Electrophoresis GmbH	Heidelberg, Germany
Sigma	Deisenhofen, Germany
Sigma-Aldrich	St. Louis, Missouri, USA
Thermo Fisher Scientific	Waltham, Massachusetts, USA
Torcris	Bristol, United Kingdom
Zeitz Instrument GmbH	Martinsried, Germany

2.11 Statistics

Values are reported as the mean ± standard error of the mean (SEM) unless otherwise stated. Boxplots show median (central line), interquartile range (IQR; 25^{th} – to 75^{th} – percentile) (box) and complete range (whiskers); extreme values which lie more than 1.5 IQR below, respectively above the 25^{th} and 75^{th} percentile are displayed as circles. Statistical tests were carried out with R version 3.1.3. R base package. The inspection of the distribution normality was done visually by Q-Q plots (Ghasemi and Zahediasl, 2012). They did not show strong indication against the normal distribution. Comparisons between only two genotypes when experimental conditions maintained the same were assessed by Student's two-tailed t-test (unpaired) and/or Mann-Whitney-Wilcoxon test (U-test) in R. The t-tests are relatively robust against deviations from the normal distribution especially in larger samples (Dalgaard, 2008; Kabacoff, 2015). Due to the smaller sample sizes in most cases in this dissertation, the nonparametric Wilcoxon test was done in addition which does not depend on the assumption of a normal distribution.

P-values from multiple comparisons were adjusted with Bonferroni correction: the adjusted p-value is the original p-value multiplied by the number of parallel comparisons. When making multiple statistical tests, there is an increased risk of type-I error (false positive: rejecting the null hypothesis when should not) (Armstrong, 2014). Bonferroni correction is a conservative method that protects against type-I error. Measurements obtained from different fibers of the same mouse were considered independent because the unavoidable individual experimental conditions (loading status etc.) affect the measurements even more than the mouse to mouse discrepancy. In figures and tables, the significance of the differences is indicated according to the following standard: * indicates $p \leq 0.05$, ** indicates $p \leq 0.01$, *** indicates $p \leq 0.001$.

3 Results

This section consists of two parts. The first part presents the e-c coupling properties of the NC fibers which permanently lack the L-type Ca^{2+} current. These properties include inward Ca^{2+} current, voltage-dependence of the Ca^{2+} release, and the SR Ca^{2+} store content is also studied as it is supposed relevant to the Ca^{2+} entry from the DHPR. Most interestingly, the Ca^{2+} inactivation properties of the NC fibers are investigated under different extracellular [Ca^{2+}]. Based on previous work, mutations adjacent to the selectivity filter of K^+ channels affected the properties of the C-type inactivation. It is suspected that the NC mutation might contribute to changes in the voltage-dependent inactivation of $Ca_v1.1$. The second part focuses on the mouse model carrying an MH causing mutation in the RyR1. Previous studies have reported alteration in the inactivation properties due to this mutation. It will be further studied under experimentally modified Ca^{2+} release in terms of preventing potential acute effects of Ca^{2+} on the DHPR. The aim is to determine whether the elevation of myoplasmic [Ca^{2+}] in YS fibers is the cause or involved in the shift of the inactivation.

3.1 E-c coupling in fibers containing non-conducting DHPR

Eliminating the L-type Ca^{2+} current pharmacologically by applying L-type Ca^{2+} channel blockers have been studied before in experiments. However, the NC mouse model offers an opportunity to investigate the long-term physiological importance of the L-type Ca^{2+} current in skeletal muscle e-c coupling in mammals. The single point mutation N617D which was found to be responsible for the complete loss of L-type Ca^{2+} in zebrafish was introduced into the murine CACNA1S gene encoding $Ca_v1.1$. In this dissertation, the two-electrode voltage clamp was performed on mature muscle fiber from the interosseous muscle of adult male mice.

3.1.1 L-type Ca^{2+} current in NC knock-in mice

Firstly, the loss of Ca^{2+} influx in knock-in mice was examined. Depolarization of the sarcolemma membrane activates the DHPR to conduct the slow inward Ca^{2+} current and to initiate Ca^{2+} release from the SR. The activation protocol (shown in Figure 23 A) was designed to investigate the voltage-dependence of activation of Ca^{2+} channels. Muscle fibers were prepared according to the procedure described in Section 2.2 “Muscle fiber preparation”; a standard external solution containing 10 mM Ca^{2+} was used in this series of experiments. From a holding potential of -80 mV, the fibers were stimulated with test steps

ranging from -60 to +50 mV (10 mV increments) for a duration of 100 ms. The time interval between test steps was 60 seconds. Representative L-type current traces are shown in Figure 23 B. In WT fibers, the inward Ca^{2+} current through the DHPR started to appear at -10 mV and peaks at 20 mV, then it decreased in amplitude when further approaching the reversal potential of Ca^{2+}. In the case of NC fibers, no inward Ca^{2+} current could be observed at any depolarizing voltage.

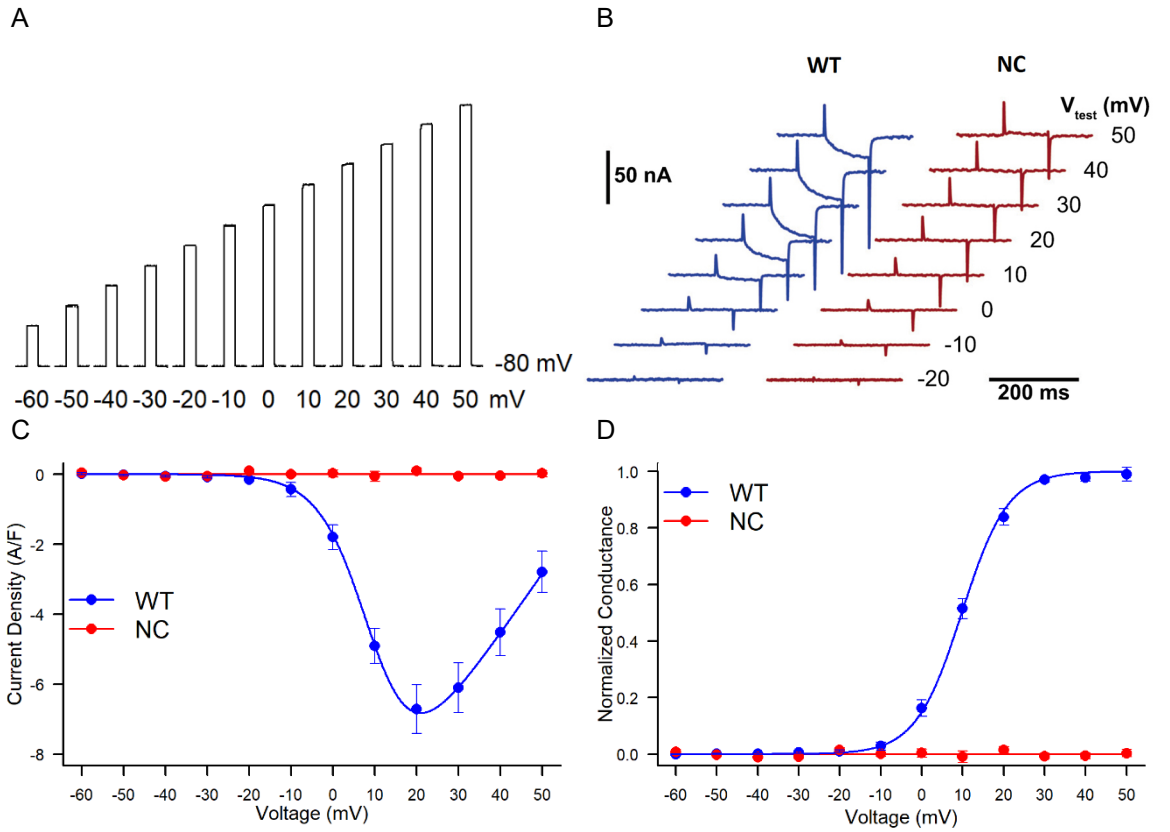

Figure 23: Current density as a function of voltage in WT and NC fibers. (A) Voltage recordings of the activation protocol. From -80 mV holding potential, depolarizing test steps of 100 ms were applied ranging from -60 to +50 mV (10 mV increment). The time interval between each test step was 60 s. **(B)** Representative traces of measured leak-corrected current using the activation protocol (test steps to voltages ranging from -20 mV to 50 mV) of a WT (blue) and an NC fiber (red). (first published in Dayal *et al.* 2017.) **(C)** Mean current density as a function of the voltage of WT (n=18) and NC (n=18) muscle fibers (mean ± SEM). Peak inward current density of WT fibers was -6.86 ± 0.70 A/F at 20 mV. The current density of the NC fibers fluctuates around 0 A/F, mean peak values ranged between -0.07 ± 0.02 and 0.10 ± 0.05 A/F. (Based on Dayal *et al.* 2017 and extended with additional data.) **(D)** Mean fractional conductance as a function of voltage (normalized to the maximum in each WT fiber) derived from data in C (mean ± SEM). The parameters $V_{1/2}$ and k of the fit line were 9.71 ± 1.01 mV and 5.63 ± 0.18 mV, respectively.

In Figure 23 C, mean current density of 18 WT fibers and 18 NC fibers was calculated and presented. The current density was obtained by dividing the measured current amplitude by the capacitance of the same fiber. This figure shows that L-type Ca^{2+} current is completely absent in NC knock-in mice (i_{max} = -0.46 ± 0.13 A/F); while in WT fibers, the mean of maximum current density was -6.86 ± 0.70 A/F at 20mV. In Figure 23 D, fractional

conductance of the Ca^{2+} inward current was obtained by fitting the Ca^{2+} current versus voltage to a Boltzmann function: $\mathrm{FA(V)} = \frac{I_{Ca}(V)}{G_{Ca}(V-V_{Ca})} = \frac{1}{1+e^{(V_h-V)/k}}$ (details see Section 2.5 "Ca^{2+} current analysis"). No meaningful data could be processed in the case of NC fibers due to the loss of the L-type Ca^{2+} current. According to 18 WT fiber measurements, the parameters of the fit curve are: $V_{1/2}$ = 9.71 ± 1.01 mV, k = 5.63 ± 0.18 mV.

3.1.2 Voltage dependence of Ca^{2+} release

Figure 24 A shows representative traces of Ca^{2+} release fluxes obtained with the activation protocol. Ca^{2+} release fluxes can be determined from the fluorescent recordings of Fura-2 according to the removal model described in Section 2.7 "Ca^{2+} transient and flux analysis". From the example traces, an almost immediate peak after the depolarization voltage pulse and a fast and a slow decreasing phase can be identified in the Ca^{2+} release flux signal. The slowly decreasing phase is understood due to SR depletion during the Ca^{2+} release (Schneider et al., 1987). The depletion correction is performed as described in Section 2.8 "Permeability Calculation" to restore the plateau phase of the release (González and Ríos, 1993).

The average peak release normalized to the maximum peak release from 15 WT and 23 NC fibers are presented in Figure 24 B. The kinetic parameters which determine the curve shape of the fit lines are: $V_{1/2}$, k, a and b. The normalized release flux plateau data was also analyzed and illustrated in Figure 24 C. The same equation was used to simulate the data. The mean values of the parameters from normalized release flux peak and plateau can be found in Table 4. Statistical analysis with t-test suggests no significant difference in any of the fit parameters between WT and NC fibers. These results suggest that the voltage dependence of the SR Ca^{2+} release properties are unaltered in the NC fibers.

Table 4: Release flux fit parameters (mean ± SEM) analyzed by Canalysis. (All p values of comparisons between WT and NC are larger than 0.05 by unpaired student's t-test)

	Normalized flux peak		Normalized flux plateau	
Genotype	WT (N=15)	NC (N=23)	WT (N=15)	NC (N=23)
$V_{1/2}$ (mV)	-6.41 ± 1.68	-7.38 ± 1.75	-11.01 ± 1.56	-11.34 ± 1.16
k (mV)	6.96 ± 0.47	7.94 ± 0.66	6.67 ± 0.16	7.06 ± 0.24
a (mV)	0.0033 ± 0.0011	0.0055 ± 0.0016	-0.0033 ± 0.0008	-0.0026 ± 0.0006
b	0.78 ± 0.04	0.65 ± 0.06	1.03 ± 0.02	1.02 ± 0.02

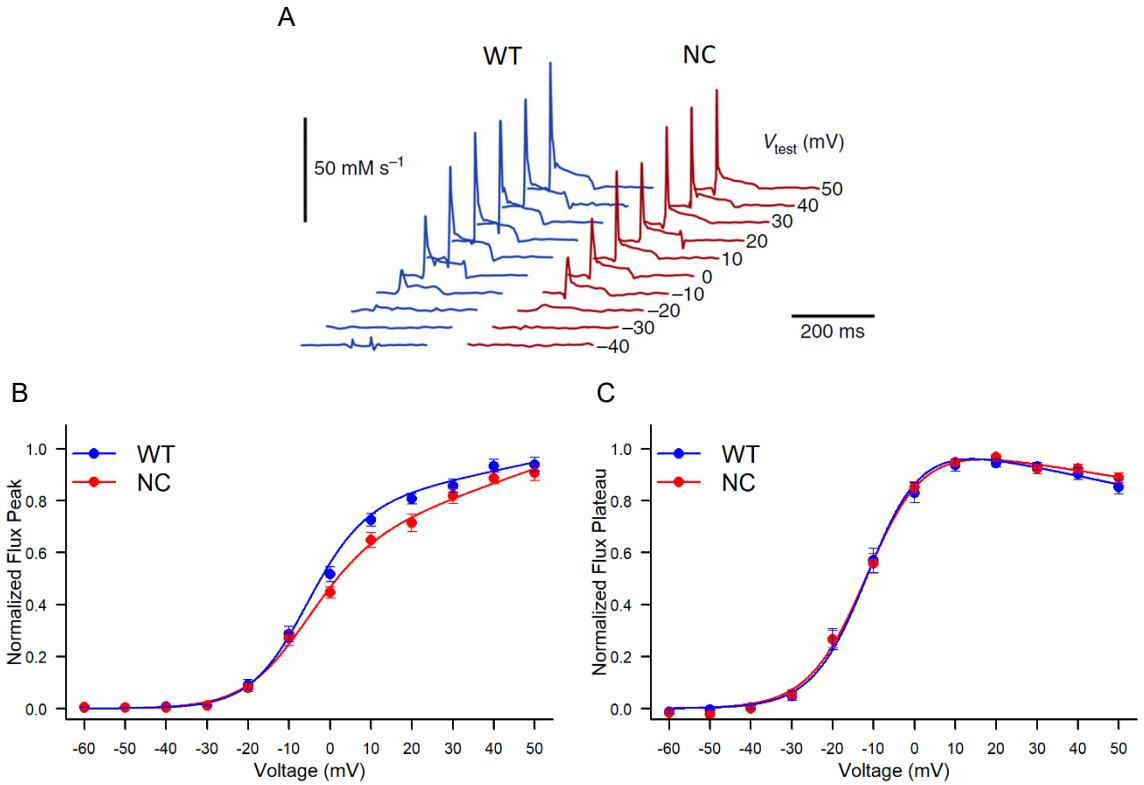

Figure 24: Voltage-dependent Ca^{2+} release flux properties in WT and NC fibers. (A) Representative traces of Ca^{2+} release flux (mM/s) determined from fluorescent recordings with Fura-2 using the activation protocol in single WT (blue) and NC (red) fibers. The fluxes display a peak and a fast decline to a plateau level. (This figure was first published in Dayal *et al.* 2017.) **(B)** Fractional activation of the peak component of the Ca^{2+} release fluxes (mean ± SEM) from WT (n=15) and NC (n=23) adult muscle fibers which exhibits similar voltage dependence. The voltage dependence of release flux normalized to the maximum was fitted by the function: $F(V) = (a + bV)/(1 + \exp((V_{1/2} - V)/k))$. The mean values of the fit parameters $V_{1/2}$, k, a and b are as following: WT: -6.41 ± 1.68 mV, 6.96 ± 0.47 mV, 0.0033 ± 0.0011 mV, 0.78 ± 0.04; NC: -7.38 ± 1.75 mV, 7.94 ± 0.66 mV, 0.0055 ± 0.0016 mV, 0.65 ± 0.06. (Based on Dayal *et al.* 2017 and extended with additional data.) **(C)** Fractional activation of the plateau component of the Ca^{2+} release fluxes (mean ± SEM), determined by averaging release flux values between 25 and 75 ms during the depolarizing pulse. The mean values of the fit parameters $V_{1/2}$, k, a and b are the following: WT: -11.01 ± 1.56 mV, 6.67 ± 0.16 mV, -0.0033 ± 0.0008 mV, 1.03 ± 0.02; NC: -11.34 ± 1.16 mV, 7.06 ± 0.24 mV, -0.0026 ± 0.0006 mV, 1.02 ± 0.02.

3.1.3 Voltage-activated Ca^{2+} release permeability and kinetics

The permeability of the SR describes the permeable state of the SR upon different depolarizing test potentials. This indicator gives information about the voltage sensitivity of the SR Ca^{2+} releasing function. To obtain the permeability data from the Ca^{2+} release fluxes, a depletion correction was first performed. It is assumed that the residual release flux during the plateau phase of the signal is constant and the decline during the plateau is only due to SR depletion (González and Ríos, 1993). With an estimation of the initial SR content (using

least squares optimization), permeability data were determined as shown in Figure 25 A-C. It was found that the peak permeability of the NC fibers showed very similar voltage-dependece and maximal value as in the WT fibers. The same is true for the plateau level of the Ca^{2+} release flux signals after depletion correction. The permeability calculations exhibited no significant differences between genotypes, which is consistent with the Ca^{2+} release flux data in Section 3.1.2.

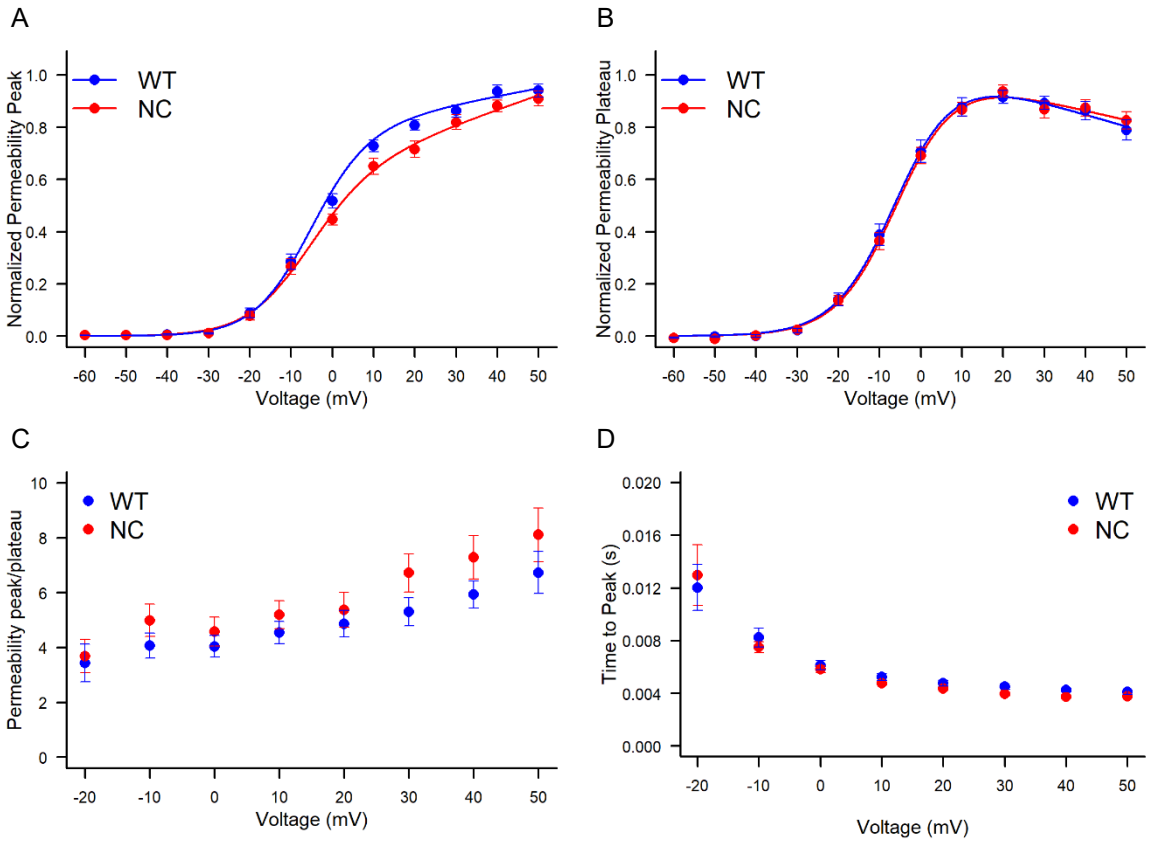

Figure 25: Voltage-activated SR permeability properties in WT and NC fibers. (A and B) Fractional voltage-dependent SR Ca^{2+} release permeabilities of peak (A) and plateau (B) derived from the data in Figure 24 (B and C) with the assumption that the slow decline during the plateau phase was due to SR depletion. The mean values of the fit parameters $V_{1/2}$, k, a and b are as following: Normalized permeability peak: -5.89 ± 1.75 mV, 6.98 ± 0.50 mV, 0.0030 ± 0.0012 mV, 0.80 ± 0.05 (WT); -7.31 ± 2.71 mV, 7.82 ± 0.75 mV, 0.0055 ± 0.004 mV, 0.65 ± 0.18 (NC). Normalized permeability plateau: -1.78 ± 3.08 mV, 7.58 ± 0.74 mV, -0.0095 ± 0.0003 mV, 1.28 ± 0.16 (WT); -5.42 ± 1.17 mV, 7.20 ± 0.34 mV, -0.0038 ± 0.001 mV, 1.02 ± 0.04 (NC). **(C)** Ratio of permeability peak/plateau as a function of voltage. **(D)** Rising time to peak (TTP) values determined from the Ca^{2+} release fluxes as a function of voltage. (Figure A, C and D are based on Dayal *et al.* 2017 and extended with additional data.)

Another characteristic of the Ca^{2+} signals is the voltage dependence of the peak to plateau ratio of the permeability. It is also one of the main differences between amphibian and mammalian skeletal muscles (Shirokova, 1996). In rodents, this value rises slowly with increasing voltage, which is attributed to negligible CICR contribution to e-c coupling and a larger density of RyRs (Margreth et al., 1993; Ríos, 2018). Figure 25 C suggests no

significant deviations in the voltage dependence of the mean peak/plateau permeability ratios between the NC and WT fibers. Values of the fit parameters of the permeability analysis are summarized inTable 5.

Table 5: Release permeability fit parameters (mean ± SEM) analyzed by Canalysis. (All p values of comparisons between WT and NC are > 0.05 by unpaired student's t-test)

	Normalized Permeability peak		Normalized Permeability Plateau	
Genotype	WT (N=15)	NC (N=23)	WT (N=15)	NC (N=23)
$V_{1/2}$ (mV)	-5.89 ± 1.75	-7.31 ± 2.71	-1.78 ± 3.08	-5.42 ± 1.17
k (mV)	6.98 ± 0.50	7.82 ± 0.75	7.58 ± 0.74	7.20 ± 0.34
a (mV)	0.0030 ± 0.0012	0.0055 ± 0.004	-0.0095 ± 0.0003	-0.0038 ± 0.001
b	0.80 ± 0.05	0.65 ± 0.18	1.28 ± 0.16	1.02 ± 0.04

To further quantify the kinetics of Ca^{2+} release flux peak, time to peak (TTP) which indicates the time duration before reaching the peak release of each trace is calculated and shown in Figure 25 D. TTP data from depolarizations ranging from -20 mV to 50 mV is plotted against the potential of the test pulse. In general, the TTP values decrease with increasing test pulse in both WT and NC fibers. It indicates that with higher test pulse potentials, the Ca^{2+} release is activated faster. No significant difference was observed between data from WT and NC fibers.

3.1.4 SR Ca^{2+} store content

In NC fibers, the Ca^{2+} inward current, which is a major source for Ca^{2+} entry into the fiber is permanently absent. This naturally raises questions about the SR Ca^{2+} store content. In this section, experiments were designed and performed to collect information on whether the long-term absence of Ca^{2+} L-type current affects the SR Ca^{2+} store capacity. Chemically induced unloading of the SR was used under conditions to minimize reuptake to assess store content. Ratiometric fluorescent Ca^{2+} indicator Fura-FF-AM was used to accommodate the externally loaded cells without sufficient Ca^{2+} buffering, thanks to its lower binding affinity to Ca^{2+} compared to Fura-2. The low affinity of Fura-FF avoids dye saturation during the rapid release of large amounts of Ca^{2+} upon stimulation. Fibers were exposed to RyR agonist 4-chloro-m-cresol (4-CmC) to induce Ca^{2+} release. Cyclopiazonic acid (CPA), a SERCA blocker was also added to the Ca^{2+}-releasing solution to reduce the reuptake of the released Ca^{2+} to the SR. A Ca^{2+}-free external solution was the base of the Ca^{2+}-releasing solution, that can eliminate the potential influence of extracellular Ca^{2+} ions.

Figure 26 A is an example recording when 30 μM CPA was applied alone, which demonstrates the SERCA blocking effect. The slowly elevated ratio signal of F_{340}/F_{380} indicating increasing [Ca^{2+}] in the cell, suggests that in the presence of CPA, SERCA function is blocked and cannot compensate for the resting leak of Ca^{2+} from the SR. Figure 26 B is a representative trace of the measurement when a combination of 0.5 mM 4-CMC and 30 μM CPA (Ca^{2+}-releasing solution) was applied to the fiber to stimulate Ca^{2+} release. From the time of the drug application (at 20 s), the myoplasmic Ca^{2+} concentration rises rather rapidly reaching its peak amplitude. The peak Ca^{2+} release upon stimulation can reflect the initial total SR Ca^{2+} store content level. Delta ratios between peak and baseline of the traces from both genotypes were analyzed and are presented in Figure 26 C. The mean delta ratio of the WT fibers is 0.522 ± 0.021 (n=49), that of the NC fibers is 0.537 ± 0.017 (n=54). Unpaired student's t-test indicates no significant difference ($p > 0.05$) between the two groups.

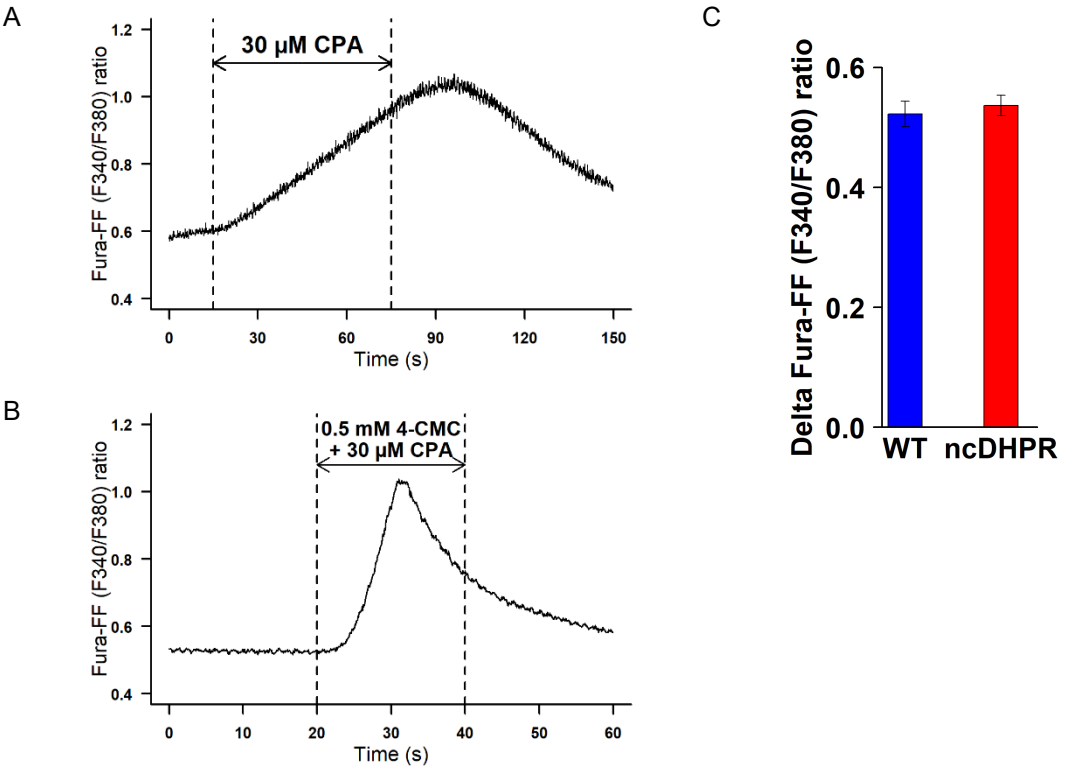

Figure 26: Evaluation of chemically induced Ca^{2+} release using Fura-FF as the fluorescent indicator. (A) Example recording of cytosolic Ca^{2+} concentration change (shown as F_{340}/F_{380} ratio) when the SERCA blocker CPA (30 μM) was applied alone (between 15 and 75 s indicated by the two dashed lines) in Ca^{2+}-free external solution. The fibers were then rinsed for 75 s by CPA-containing Ca-free solution. **(B)** Example recording of Ca^{2+} release stimulated for a duration of 20 s (between the dashed lines) by 0.5 mM of the RyR agonist 4-CMC in combination with 30 μM CPA in Ca^{2+}-free external solution. (modified from Dayal et al. 2017) **(C)** Average maximal Ca^{2+} release presented as Δratio between peak and base line of the fluorescence signals (F_{340}/F_{380}) of WT (n=49) and NC (n=54) fibers. The mean ± SEM values are 0.522 ± 0.021 and 0.537 ± 0.017 for WT and NC respectively.

3.1.5 Current and release availability measurements

The DHPR in mammalian skeletal muscle is subjected to voltage-dependent inactivation. The inactivation takes place when fibers are stimulated with a long depolarization. The fibers then become “reprimed” before a further response can be evoked. It is known that the voltage-dependent inactivation is associated with charge immobilization of the intramembrane charge movement. However, on the contrary to the K^+ and Na^+ channels, in which two distinct inactivation mechanisms, N-type and C-type, were identified, the inactivation of the Ca^{2+} channels is less understood. One commonly accepted theory suggested by Rios and co-workers – the Ca^{2+}/metal ions binding activity (Brum and Ríos, 1987; Ríos and Pizarro, 1991), involved with the four state gating diagram, offered some explanation to the voltage-depend inactivation of the channel (see Section 1.6 “Inactivation of Ca^{2+} channel”). The shortcoming is that the earlier studies were based on amphibian, not mammalian skeletal muscle. The NC mouse contains a point mutation in the pore loop contributed by domain II of $Ca_v1.1$ adjacent to the negatively charged regions of the selectivity filter. A neutrally charged asparagine is replaced by a negatively charged aspartic acid. This will likely change the Ca^{2+} binding at the pore and therefore makes it interesting to investigate the effect of this DHPR mutation on voltage-dependent inactivation. Until now, no similar studies are available to provide an insight into this question.

Voltage-dependent current and release availabilities of WT and NC fibers were measured with inactivation protocols. Release availability is a result of both voltage-dependent inactivation and depletion of the SR, since depletion has a substantial impact on the release (Robin and Allard, 2013). The protocols maintained the membrane potential at depolarized state for a longer time, for the voltage-dependent inactivation to take place. Protocols – standard or short, was performed to depolarize the membrane for 30 s at various holding voltages ranging from -80 to +10 mV (standard, Figure 27 A) or from -80 to -10 mV (short, Figure 27 B). After each conditioning depolarization, a test pulse of 100 ms duration to +50 mV (standard) or +20 mV (short) was applied. Neither current nor release properties obtained from the measurements generated with the two inactivation protocols differ from one another. It was reasonable to combine the data of the two protocols that had the same experimental conditions. As this will increase the sample size of each experimental group, and therefore, reduce the error and increase the reliability of the statistical analysis.

A series of representative Ca^{2+} inward current traces during availability measurements are shown in Figure 27 C. It is demonstrated that in WT fibers, with progressively increasing holding potentials, Ca^{2+} current was reduced which indicates inactivation taking place. In NC fibers, the Ca^{2+} current is absent. Current availability was calculated from the Ca^{2+} current at the end of every test pulse (time range 1.19 – 1.199 s, more details see Section

2.5 “Ca^{2+} current analysis”) shown in Figure 27 D. The loss of the L-type Ca^{2+} current due to the N617D mutation in the DHPR is illustrated again in inactivation measurements. Due to the absence of the L-type current, the investigation to compare DHPR inactivation in different experimental groups focused on the Ca^{2+} release availability.

A series of representative traces of the background-corrected Fura-2 fluorescence ratio during inactivation measurement are shown in Figure 27 E. Figure 27 F shows the steady-state availability of SR Ca^{2+} release derived from delta ratio at the end of the test pulses. The measurements were performed in the standard external solution containing 10 mM Ca^{2+} to augment Ca^{2+} current. The points in this figure represent the mean ± SEM values at each individual voltage, while the solid lines are generated with the mean fit parameters obtained from fitting the following Boltzmann function: $FI(V) = \frac{1}{1+e^{(x-V_h)/k}}$ to the data points. The release availability data in this figure were obtained from 13 WT and 18 NC fibers. The values of the fit parameters and the result of statistical tests are summarized in Table 6. The mid-voltages of the two groups were indistinguishable when evaluated by both student’s t-test (unpaired) and Mann-Whitney-Wilcoxon test. A discrepancy was found in the slope factor k. The NC fibers appeared to inactivate more sensitively to increasing voltage while the mid-voltage stayed the same.

Table 6: Fit parameters of the Ca^{2+} release inactivation in external solution containing 10 mM $[Ca^{2+}]$. (*** indicates p < 0.005 in unpaired student’s t-test between WT and NC.)

Genotype	WT (N=13)	NC (N=18)
$V_{1/2}$ (mV)	-30.11 ± 1.28	-32.46 ± 1.30
k (mV)	7.11 ± 0.40	5.23 ± 0.23 ***

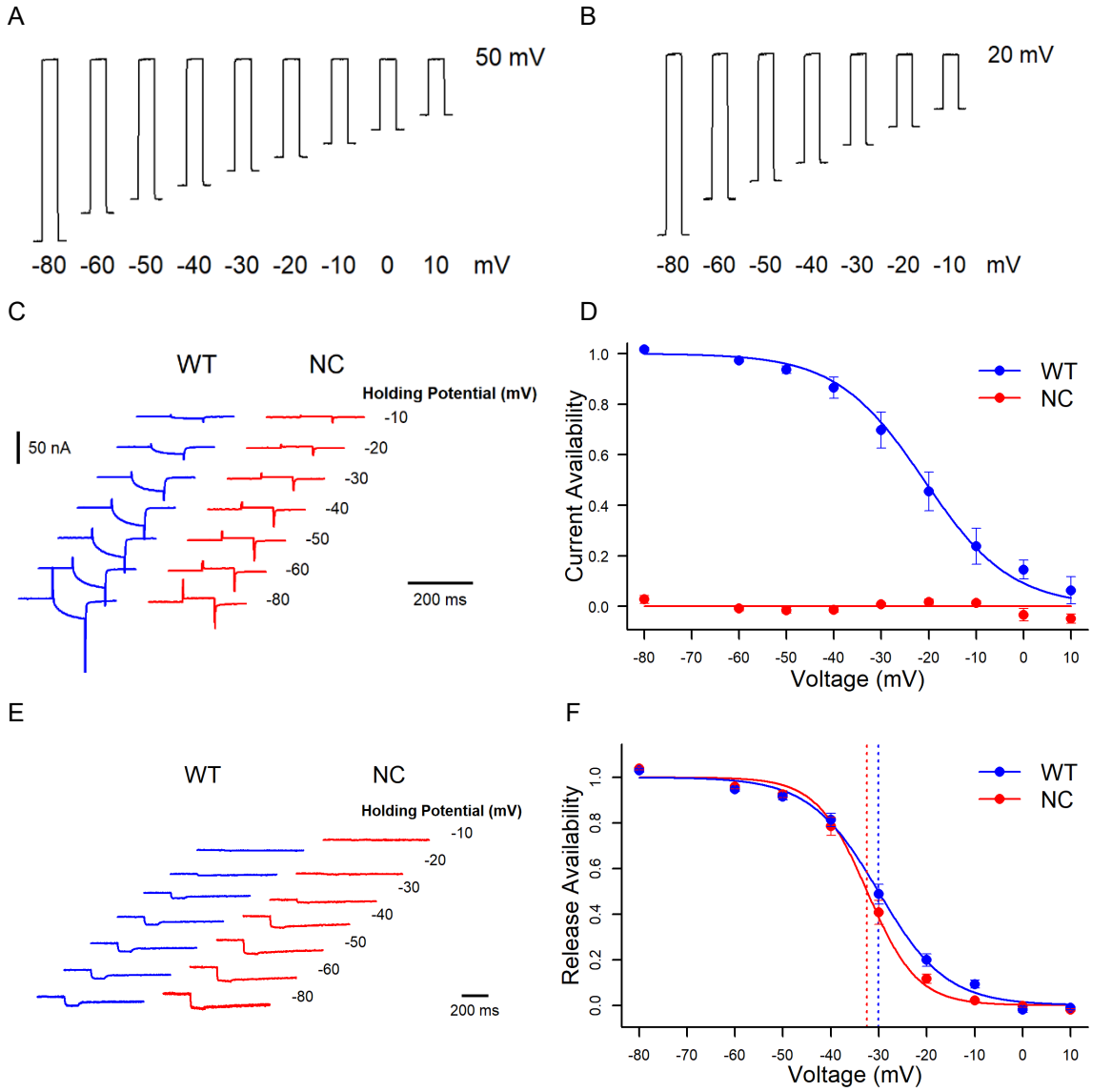

Figure 27: Voltage-dependent availability of Ca^{2+} current and release measured in WT and NC fibers. (A) Voltage steps of the standard inactivation protocol: test pulses to +50 mV for 100 ms were applied from progressively increasing holding potentials ranging from -80 to +10 mV. The change to the new holding potential always occurred 30 s prior to the test pulse. **(B)** Voltage steps of the short inactivation protocol: test pulses to +20 mV were applied from progressively increasing holding potentials ranging from -80 to -10 mV (same timing as in A). **(C)** Representative leak-corrected current traces (-80 to -10 mV holding potentials) using the short inactivation protocol on a WT (blue) and an NC fiber (red). The correction was performed using a preceding hyperpolarizing pulse within the same episode (amplitude of -10 mV; not shown in the figure). **(D)** Mean fractional L-type current availability calculated from current measurements in 10 mM extracellular [Ca^{2+}] from WT (n=7) and NC (n=18) fibers (normalized to the maximum of the WT). The fit parameters to the Boltzmann function of WT current inactivation are $V_{1/2}$ = -20.97 ± 3.40 mV and k = 9.17 ± 0.98 mV. The Ca^{2+} current in NC fibers was not present. **(E)** Representative background-corrected fluorescence ratio traces (-80 to -10 mV holding potentials) using the short inactivation protocol on a WT (blue) and an NC fiber (red). **(F)** Mean fractional release availability of Ca^{2+} signals from WT (n=13) and NC (n=18) fibers measured in the external solution with 10 mM [Ca^{2+}]. Blue and red points represent WT and NC mean ± SEM values respectively. The lines were drawn using the mean of the individual best fit parameters according to Boltzmann equation for WT: $V_{1/2}$ = -30.11 ± 1.28 mV, k = 7.11 ± 0.40 mV; for NC: $V_{1/2}$ = -32.46 ± 1.30 mV, k = 5.23 ± 0.23 mV. Dotted vertical lines indicate the $V_{1/2}$ values.

3.1.6 Effect of Extracellular Ca^{2+} on release availability and activation

Previous studies on amphibian skeletal muscle demonstrated that reduced external Ca^{2+} concentration caused a left shift in the Ca^{2+} release inactivation curve while that of activation remained almost the same (Brum et al., 1988b). The experiments in this section were designed to investigate the effect of the extracellular Ca^{2+} concentration on inactivation. The external [Ca^{2+}] was reduced to 0.1 mM while replacing the missing Ca^{2+} with Mg^{2+} to maintain the total divalent cation concentration unchanged. Figure 28 A contains all release availability curves from WT and NC in two different external [Ca^{2+}]. The open circles in blue and red show data obtained from 8 WT and 7 NC fibers respectively at low external [Ca^{2+}]. The dashed lines were generated using the mean parameters from individual fits with a Boltzmann function from WT and NC fibers. The fit parameters under the reduced external [Ca^{2+}] condition are listed in Table 7.

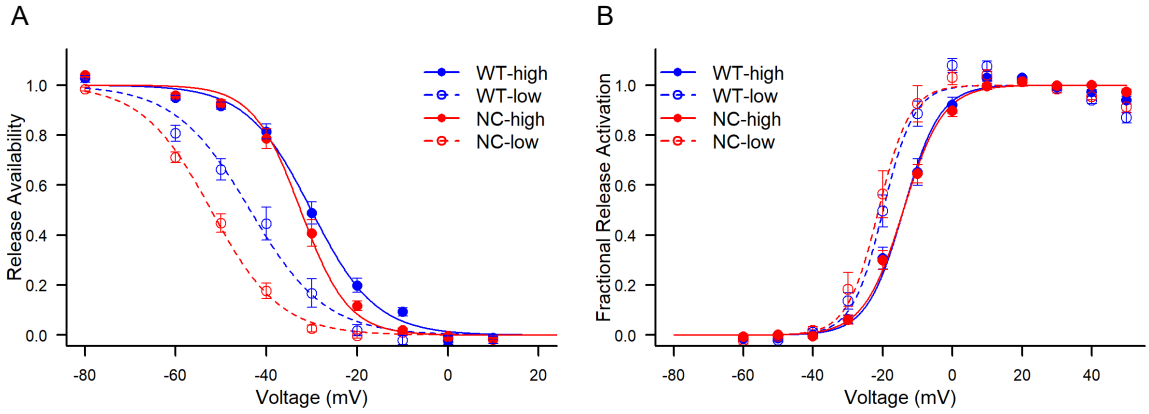

Figure 28: Alterations in the voltage dependence of the release availability and activation measured in two different extracellular [Ca^{2+}]. (A) Fractional availability curves of WT and NC fibers in external solutions containing 10 mM and 0.1 mM [Ca^{2+}]. The mean fit parameters of curves at low $[Ca^{2+}]_e$ are: WT $V_{1/2}$ = -43.59 ± 2.19 mV, k = 8.26 ± 0.76 mV; NC $V_{1/2}$ = -52.18 ± 1.00 mV, k = 7.58 ± 0.40 mV. The mid-voltages from both WT and NC fibers showed stronger hyperpolarizing shifts than in the activation curves in 0.1 mM $[Ca^{2+}]_e$, and NC displayed a significantly larger left-shift than the WT. **(B)** Normalized release activation curves of WT and NC fibers in external solutions containing 10 mM and 0.1 mM [Ca^{2+}]. In the latter, the total divalent cation concentration was maintained by replacing Ca^{2+} with Mg^{2+}. The open circles represent WT (n=8) and NC (n=7) (mean ± SEM) fibers in the external solution with 0.1 mM [Ca^{2+}]. In both high and low $[Ca^{2+}]_e$, the voltage dependence of release activation from WT and NC fibers were indistinguishable. However, the voltage dependence of both genotypes was shifted to hyperpolarized potentials.

The decrease of extracellular [Ca^{2+}] caused a shift of the availability curves to more negative potentials in both WT and NC fibers. The mean fit parameter $V_{1/2}$ from the Boltzmann fitting of the WT data changed by -13.48 mV, and that of the NC data changed by -19.72 mV. The left-shift in voltage dependence caused by reduced $[Ca^{2+}]_e$ in both genotypes are highly significant. It is interesting to note that while the Ca^{2+} release availability voltage dependences between two genotypes seem similar under 10 mM $[Ca^{2+}]_e$, a clear

discrepancy appeared under reduced external Ca^{2+} concentration. The data were statistically assessed by student's t-test as well as Mann-Whitney-Wilcoxon test (U-test).

Table 7: Statistical analysis (p-values adjusted by Bonferroni method (see Section 2.11 "Statistics") of the fit parameters from Ca^{2+} release availability in high (10 mM) and low [Ca^{2+}] (0.1 mM) containing external solutions. (Statistical analysis: / indicates p > 0.05, * indicates p < 0.05, ** indicates p < 0.01, *** indicates p < 0.005.)

$V_{1/2}$ (mV)		t-test	U-test	k (mV)		t-test	U-test
WT-high	NC-high			WT-high	NC-high		
-30.11 ± 1.28	-32.46 ± 1.30	/	/	7.11 ± 0.40	5.23 ± 0.23	***	***
WT-high	WT-low			WT-high	WT-low		
-30.11 ± 1.28	-43.59 ± 2.19	***	***	7.11 ± 0.40	8.26 ± 0.76	/	/
NC-high	NC-low			NC-high	NC-low		
-32.46 ± 1.30	52.18 ± 1.00	***	***	5.23 ± 0.23	7.58 ± 0.40	***	***
WT-low	NC-low			WT-low	NC-low		
-43.59 ± 2.19	52.18 ± 1.00	*	**	8.26 ± 0.76	7.58 ± 0.40	/	/

Table 8: Ca^{2+} release activation fit parameters (mean ± SEM) analyzed by R. (* indicates p < 0.05 in unpaired student's t-test between high and low [Ca^{2+}]$_e$.)

$V_{1/2}$ (mV)		t-test	U-test	k (mV)		t-test	U-test
WT-high	NC-high			WT-high	NC-high		
-14.09 ± 1.35	-14.09 ± 1.14	/	/	5.26 ± 0.19	5.69 ± 0.17	/	/
WT-high	WT-low			WT-high	WT-low		
-14.09 ± 1.35	-19.90 ± 1.41	*	/	5.26 ± 0.19	4.47 ± 0.19	*	/
NC-high	NC-low			NC-high	NC-low		
-14.09 ± 1.14	-21.23 ± 2.00	/	*	5.69 ± 0.17	4.53 ± 0.51	/	/
WT-low	NC-low			WT-low	NC-low		
-19.90 ± 1.41	-21.23 ± 2.00	*	/	4.47 ± 0.19	4.53 ± 0.51	/	/

It was reported in frog skeletal muscle fibers, that reducing extracellular [Ca^{2+}] had little effect on the voltage dependence of the activation, much less pronounced compared to the change in inactivation. To check whether this is also the case for mammals, the Ca^{2+} release activation signals in two different [Ca^{2+}]$_e$ were recorded with Fura-2. The fractional activation curves were achieved by analyzing the peak fluorescense Ca^{2+} signals and fitting their voltage dependence to a Boltzmann function as shown in Figure 28 B. Both the slope factors (k) and the mid-voltage ($V_{1/2}$) are similar in WT and NC muscle fibers under reduced external [Ca^{2+}] condition. However, they both display left-shifted voltage dependence when compared to the 10 mM [Ca^{2+}]$_e$ activation curves. The changes in the mid-voltage values

are of mild significance according to Bonferroni-adjusted t-tests (see Section 2.11 “Statistics”). Figure 28 A and B, as well as the statistical tests in Table 7 and Table 8, demonstrate that the shift of voltage dependence of Ca^{2+} release induced by reduced extracellular [Ca^{2+}] is stronger in availability curve than activation curve.

3.1.7 Window Ca^{2+} release and steady-state free [Ca^{2+}]

When fractional activation and the steady-state availability curves are multiplied, it results in a “window of release”. Within this “window of release”, the Ca^{2+} release is partly activated while some but not all channels are available leading to permanent partial activation (and a corresponding increase in the steady-state free [Ca^{2+}] level). In Figure 29 A and B, mean unnormalized Ca^{2+} release activation curves and mean fractional availability curves from each genotype and Ca^{2+} concentrations are multiplied, resulting in the predicted release windows of each experimental group.

The averaged maximum release window of the WT fibers is about 3% of the maximum Ca^{2+} release flux, while that of the NC fibers is 1.7%, in 10 mM external [Ca^{2+}]. The voltages at which the maximum release windows are reached of WT and NC fibers are -17.1 mV and -25.1 mV, respectively. In 0.1 mM external [Ca^{2+}], the maximum amplitude of both release windows from WT and NC fibers decreased significantly. The maximal amplitude of the WT release window is 1.5%, half of the corresponding value in high external [Ca^{2+}] whereas the maximum of the NC release window is only one-fourth that of the WT. The voltages at which the maximum release windows are reached of WT and NC fibers are -20.1 mV and -22.8 mV, respectively, under 0.1 mM $[Ca^{2+}]_e$. When compared to the higher external [Ca^{2+}] condition, WT data displayed a slight left shift whereas NC data displayed a slight right shift.

Figure 29 C and D illustrate the steady-state [Ca^{2+}] levels measured at the end of every depolarizing conditioning step of the inactivation protocol (Figure 27 E), shown as the background-corrected baseline ratios of the Fura-2 signals F_{380}/F_{360}. The ratios have been inversely plotted to better illustrate the change of resting [Ca^{2+}], since a decrease in the ratio F_{380}/F_{360} indicates an increase in free Ca^{2+} concentration. Under 10 mM $[Ca^{2+}]_e$ (Figure 29 C), the voltage dependence of the baseline fluorescence ratios also displays a bell shape with its maximum amplitude located at -20 mV. The resting [Ca^{2+}] changes according to conditioning voltages of WT and NC fibers are similar in terms of amplitude and voltage dependence. The release window curves of both genotypes are in general agreement with the steady-state [Ca^{2+}] change. Under 0.1 mM $[Ca^{2+}]_e$ (Figure 29 D), the overall resting [Ca^{2+}] level was lower and the change according to holding voltages was minimum for both

genotypes. Neither the voltage dependence nor the amplitude of the baseline fluorescence ratios resembled the predictions from the release windows under reduced external [Ca^{2+}].

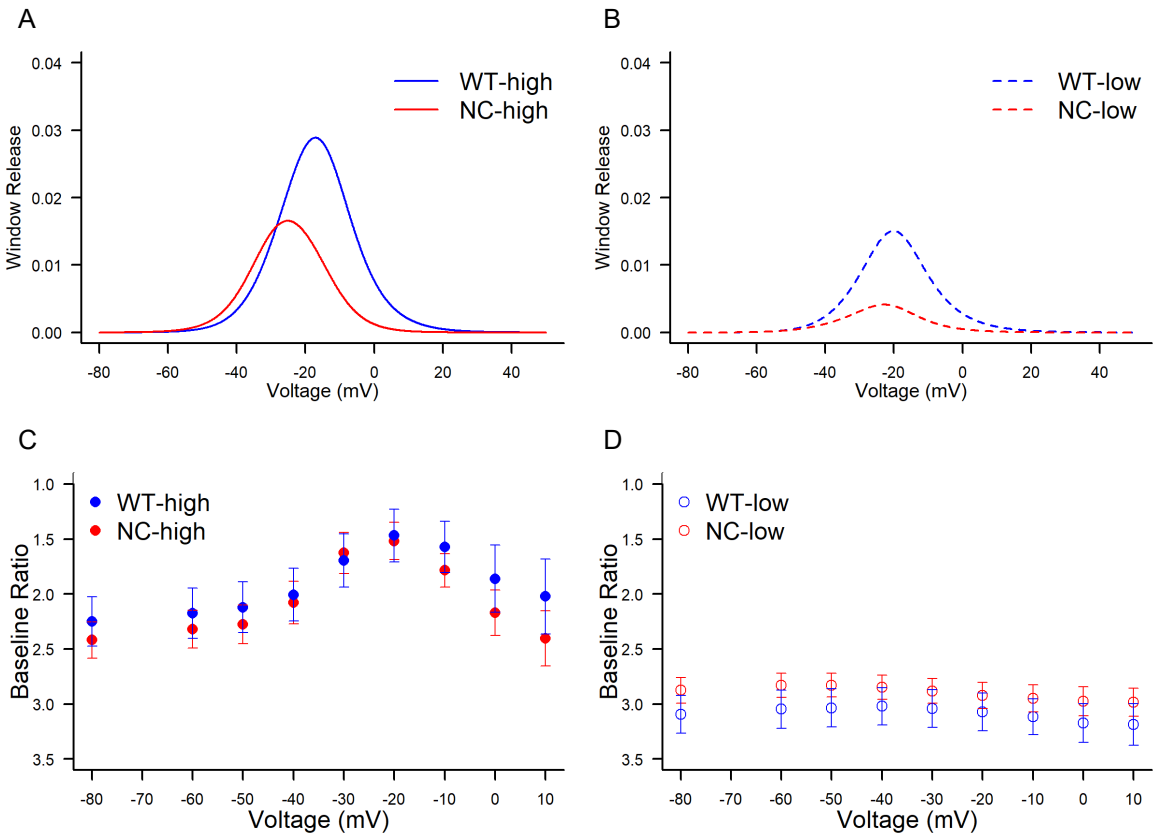

Figure 29: Voltage windows of steady-state Ca^{2+} release predicted from activation and availability curves. (A) The Ca^{2+} release window generated from 10 mM $[Ca^{2+}]_e$ curves, by multiplying the mean activation curve (non-normalized) and the mean normalized availability curve. Bell-shaped Ca^{2+} release windows show that predicted peak release of the WT fibers is 75% larger than that of the NC fibers. The peak of the NC release window is at -25.1 mV and that of the WT release window is at -17.1 mV. **(B)** The Ca^{2+} release window generated from 0.1 mM $[Ca^{2+}]_e$ curves. The amplitudes of the maximum release windows of both WT and NC fibers are significantly smaller than in (A) respectively. The amplitude of the maximum release window of the WT fibers is nearly fourfold that of the NC fibers. The voltages at which the maximal window amplitudes are reached are comparable in the two genotypes (-20.1 and -22.8 mV for WT and NC, respectively). **(C) and (D)** Change of the steady-state Ca^{2+} level (shown as the background-corrected baseline ratios of the Fura-2 fluorescence signals) at the end of each conditioning voltage during the inactivation protocol (Figure 27 A) measured in external solution containing 10 mM [Ca^{2+}] (C) and 0.1 mM [Ca^{2+}] (D) (Y-axis is plotted inversely).

3.2 Inactivation of DHPR affected by mutations in RyR1

The YS mouse model carries an MH causing mutation in the RyR1, which is known to elevate the resting intracellular [Ca^{2+}]. Earlier results obtained by our group on this mouse model indicated a retrograde effect of the mutation as the voltage dependence of the steady-state inactivation of the DHPR was found to be altered (Andronache et al., 2009). A

hypothesis behind this observation is that the myoplasmic [Ca^{2+}] release plays a modulatory role in the inactivation. In this section, experiments were designed to investigate whether the altered Ca^{2+} release in the MH mutant fibers contributes to the shift of the availability curve by limiting the free [Ca^{2+}] in the cell.

3.2.1 Ca^{2+} current activation

The same activation protocol as in Figure 23 A was used to record the voltage-activated L-type Ca^{2+} current. BAPTA-containing internal solution (see Section 2.10 “Solutions”) was used in all experiments in Sections 3.2.1 – 3.2.4. Representative L-type current traces are shown in Figure 30 A. The capacitive current in this figure has been corrected proportionally to the signals measured at the test pulse of -40 mV. The inward Ca^{2+} current was activated from -10 mV and peaks at 20 mV. The voltage dependence of the current activation of the YS fibers has a slightly lower threshold.

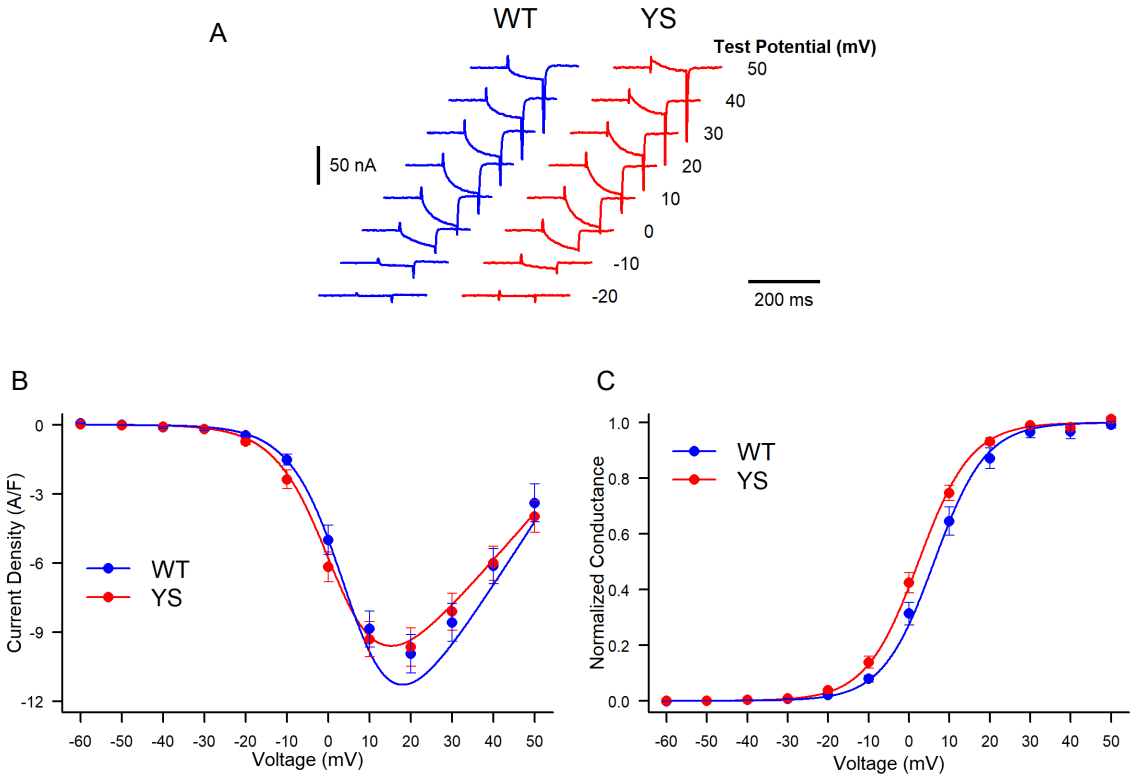

Figure 30: Voltage-dependent activation of Ca^{2+} inward current of WT and YS fibers. (A) Representative leak-corrected current traces using the activation protocol (test steps to voltages ranging from -20 mV to 50 mV are shown) of a WT fiber (blue) and a YS fiber (red). The correction was performed using traces at -40 mV as reference. **(B)** The current-voltage relationship shown in current density (A/F) by normalizing current to cell capacitance of WT (n=13) and YS (n=14) muscle fibers (mean ± SEM). Peak current density of WT fibers was 10.01 ± 0.84 A/F at 17.7 mV, that of the YS fibers was 9.81 ± 0.83 A/F at 16.4 mV. **(C)** The normalized Ca^{2+} conductance of WT and YS fibers (mean ± SEM). Parameters of fitting to the Boltzmann equation are: $V_{1/2}$ = 6.18 ± 1.56 mV (WT), 2.31 ± 1.02 mV (YS); k= 6.40 ± 0.36 mV (WT), 6.53 ± 0.22 mV (YS).

In Figure 30 B and C, the blue and red points represent mean values of measurements from 13 WT and 14 YS fibers respectively. The lines are plotted based on the average of the fit parameters from each genotype using the same fitting functions described in Section 3.1.1. The details of the fitting analysis are shown in Table 9. The first visible inward Ca^{2+} current was activated at -20 mV and reached its peak amplitude at 17.7 mV for WT and at 16.4 mV for YS fibers. They exhibit similar maximal Ca^{2+} current density. In normalized Ca^{2+} conductance curves, YS fibers displayed a slight left-shift in the mid-voltage of about 4 mV. The difference is of borderline statistical significance analyzed by the t-test (p=0.49). A difference in the slope factor k was indistinguishable.

Table 9: Fit parameters from Ca^{2+} current activation data of YS and WT fibers. (* indicates p < 0.05 by unpaired student's t-test between WT and YS.)

Genotype	WT (n=13)	YS (n=14)
iCa_{max} (A/F)	-10.01 ± 0.84	-9.81 ± 0.83
$V_{1/2}$ (mV)	6.18 ± 1.56	2.31 ± 1.01 *
k (mV)	6.40 ± 0.36	6.53 ± 0.22

3.2.2 Ca^{2+} signals under SR depletion conditions

In order to unload the SR and prevent acute effects of Ca^{2+} release on the DHPR, the SR depletion conditions were applied, which includes no added Ca^{2+} into the internal solution, using BAPTA instead of EGTA as the Ca^{2+} chelator, and introducing the SERCA blocker CPA. The conditions also included performing a series of Ca^{2+} releasing protocols after the loading phase before the activation and availability measurements. Since BAPTA binds to Ca^{2+} ions with much faster kinetics, it is very effective in buffering Ca^{2+} close to the pore after voltage-activated Ca^{2+} release mediated by RyR1. Buffering with a high concentration of BAPTA can restrict the local [Ca^{2+}] increase as well as the Ca^{2+} reuptake back to the SR. The SERCA blocker CPA was introduced to the external solution to limit the efficiency of SERCA pumps. Additionally, no Ca^{2+} was added to the internal solution to further limit the Ca^{2+} source. The SR depletion conditions aim to limit the acute effects of the Ca^{2+} release from the SR on the DHPR.

Figure 31 A are example background-corrected Fura-2 fluorescence ratio traces of one cell measured in the 15 mM EGTA-containing internal solution, and another measured under the SR depletion conditions. A ratio signal drop-down indicates a rise of the cytosolic Ca^{2+} concentration, upon Ca^{2+} release from the SR activated by depolarizing test pulses. A noticeable point is that after the test pulses were applied, the changes of the fluorescence ratio signals showed different kinetics between the EGTA and BAPTA buffered cells. In the

cell with EGTA as the dominant internal buffer, the signals displayed a steep drop-down. This is due to the saturation of the fluorescent indicator Fura-2, since EGTA, as a slow chelator for Ca^{2+}, cannot immediately bind to the large amount of Ca^{2+} ions rapidly being released to the myoplasmic space from the SR. On the contrary, the BAPTA signals displayed a slow decay following the Ca^{2+} release, attributed to its fast binding kinetics to Ca^{2+} ions. This example demonstrates how internal Ca^{2+} buffers can affect the measured intracellular Ca^{2+} transient.

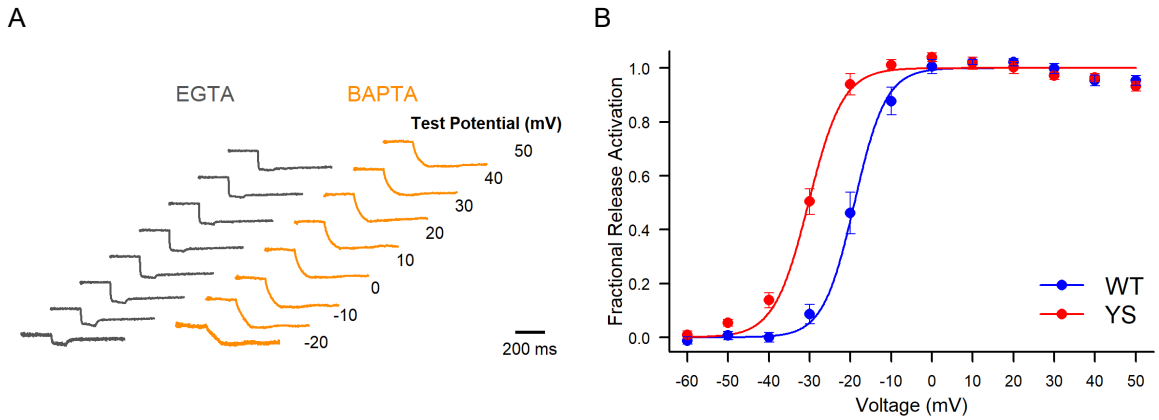

Figure 31: Voltage-dependent activation of Ca^{2+} signals of WT and YS fibers under SR depletion conditions. (A) Representative background-corrected fluorescence ratio traces recorded using the activation protocol (test steps to voltages ranging from -20 mV to 50 mV are shown). The grey traces are from a cell loaded with 15 mM EGTA-containing internal solution, and the orange traces are from a cell under SR depletion conditions (10 mM BAPTA in the internal solution in addition to CPA presence). **(B)** Normalized Ca^{2+} release activation curves of WT (n=13) and YS (n=13) fibers under SR depletion conditions. The mean fit parameters (mean ± SEM) are: $V_{1/2}$ = -19.03 ± 1.56 mV, k = 3.85 ± 1.56 mV (WT); $V_{1/2}$= -30.29 ± 0.98 mV, k= 4.23 ± 0.48 mV (YS). The voltage-dependence of the YS fibers are significantly shifted to lower potentials (t-test, p<0.005).

Under the SR depletion conditions, the plot of normalized Ca^{2+} signals at different voltages were obtained by analyzing the fluorescence ratios at the end of each test pulse as shown in Figure 31 B. The mid-voltage $V_{1/2}$ of the peak release from YS fibers exhibits a significant left-shift by about 11 mV compared to that of the WT. This confirms earlier findings of lowered activation voltage threshold of Ca^{2+} release caused by YS mutation (Andronache et al., 2009). On the other hand, the slope factor k remained the same. The values of the fit parameters are summarized in Table 10.

Table 10: Fit parameters from Ca^{2+} activation signals of WT and YS fibers. (*** indicates p < 0.005 by unpaired student's t-test between WT and YS.)

Genotype	WT (n=13)	YS (n=13)
$V_{1/2}$ (mV)	-19.03 ± 1.56	-30.29 ± 0.98 ***
k (mV)	3.85 ± 1.56	4.23 ± 0.48

3.2.3 Ca^{2+} release and current availability under SR depletion conditions

The availabilities of Ca^{2+} release and Ca^{2+} current were measured simultaneously under the previously mentioned SR depletion conditions. The voltage protocol used in availability measurements is shown in Figure 32 A. The holding potential progressively rises from -80 to 10 mV for a duration of 30 s each to induce the voltage-dependent inactivation. A series of representative traces of the Ca^{2+} inward current during inactivation protocol are shown in Figure 32 B. It is illustrated that with progressively increasing holding potentials, the amplitude of the Ca^{2+} current decreases. The Ca^{2+} current at the end of every test pulse was normalized and plotted versus voltage in Figure 32 C. The mid-voltage value ($V_{1/2}$) of the current activation in YS fibers is 9.2 mV left shifted compared to the WT fibers. The steepness (k) of the voltage dependence are similar in WT and YS fibers. The values of all parameters describing the Ca^{2+} release and current availability are summarized in Table 11.

A series of representative traces of the background-corrected Fura-2 fluorescence ratio during inactivation measurement are shown in Figure 32 D. It illustrates that the decaying of Ca^{2+} signals in YS fibers showed stronger voltage dependence than in WT fibers. Figure 32 E illustrates the normalized Ca^{2+} release response to changing holding potentials. The blue and red points represent mean values of the release availabilities of WT and YS fibers, respectively. The lines were generated using the mean parameters obtained from the individual Boltzmann function fits (same as in Section 3.1.5). The voltage dependence of the Ca^{2+} release availability curve is shifted to more hyperpolarizing potentials in the YS fibers; the difference of the mid-voltage ($V_{1/2}$) compared to the WT is -11.9 mV. The slope factor of the YS fibers is slightly larger (shallower decay) than in WT, but it does not show statistical significance.

Table 11: Fit parameters of Ca^{2+} current and release signals availability data of WT and YS fibers. (*** indicates $p < 0.005$ by unpaired student's t-test between WT and YS.)

	Ca^{2+} Current		Ca^{2+} Signals	
Genotype	WT (n=11)	YS (n=13)	WT (n=12)	YS (n=15)
$V_{1/2}$ (mV)	-25.84 ± 1.63	-35.01 ± 1.27***	-40.09 ± 2.16	-51.96 ± 1.26***
k (mV)	8.14 ± 0.41	8.50 ± 0.64	6.60 ± 0.58	7.99 ± 0.62

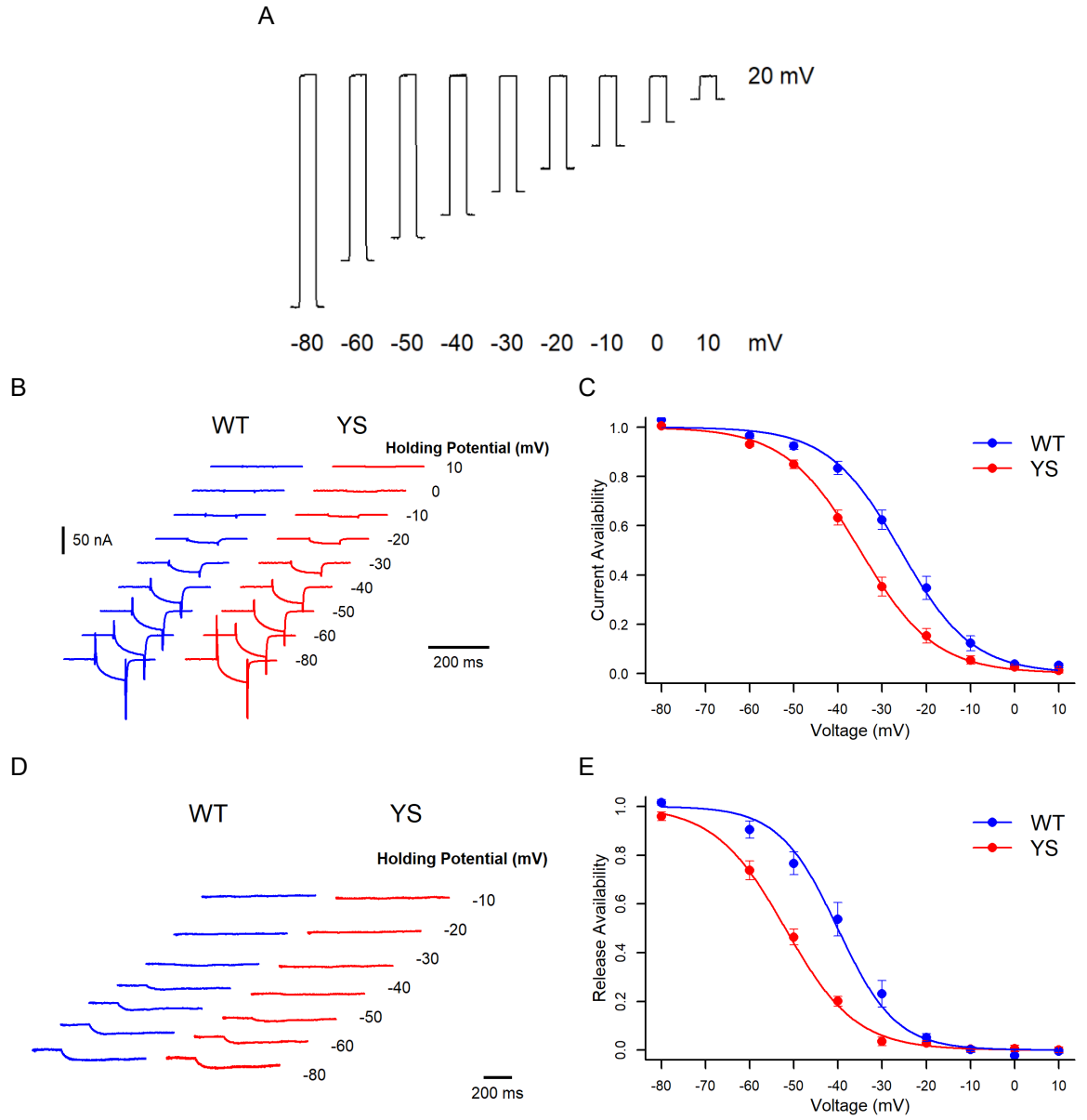

Figure 32: Availability of Ca^{2+} current and Ca^{2+} release of WT and YS fibers under SR depletion conditions. (A) Voltage pulses of the inactivation protocol. Test pulses (to +20 mV for 100 ms) were applied from progressively increasing holding potentials ranging from -80 to +10 mV. The change to the new holding potential always occurred 30 s prior to the test pulse. **(B)** Representative leak-corrected current traces obtained using the inactivation protocol of a WT (blue) and a YS fiber (red). The correction was performed using a preceding hyperpolarizing pulse within the same episode (amplitude of -10 mV; not shown in the figure). **(C)** Current availability data from WT (n=11) and YS (n=13) fibers. The fit parameters (mean ± SEM) are $V_{1/2}$ = -25.84 ± 1.63 mV and k = 8.14 ± 0.41 mV for WT fibers; $V_{1/2}$ = -35.01 ± 1.27 mV and k = 8.50 ± 0.64 mV for YS fibers. The YS voltage-dependence exhibits a left-shift of about 9 mV. **(D)** Representative background-corrected fluorescence ratio traces using the inactivation protocol in A on a WT fiber (blue) and a YS fiber (red). **(E)** Fractional release availability curves from WT (n=12) and YS (n=15) fibers. The lines are drawn using the following mean fit parameters: $V_{1/2}$ = -40.09 ± 2.16 mV, k = 6.60 ± 0.58 mV (WT); $V_{1/2}$ = -51.96 ± 1.26 mV, k = 7.99 ± 0.62 mV (YS). The YS voltage-dependence exhibits a left-shift of about 12 mV.

3.2.4 The windows of Ca^{2+} release and Ca^{2+} current

The window of Ca^{2+} release predicted in Figure 33 A is the product of the availability curve and the release activation curve (non-normalized). It provides information about the expected steady-state Ca^{2+} release from the SR. Blue lines represent WT fibers, and red lines represent YS fibers. The red dashed line is the supposed window of release if the release availability curve of the YS fibers had stayed the same while only the activation curve had the left shift. Since both release activation and availability curves of the YS fibers have left-shifted, the peak of its release window also displayed a left shift of about the same degree when compared to the WT. The peak amplitudes of the predicted Ca^{2+} release window of the WT and YS fibers are 1.8% and 2.3%, respectively. However, it would be 3 times larger (6.9%) if only the activation curve had the left shift, as the red dashed line indicates. It suggests that the left shift of the release availability curve of the YS fibers prevents large amounts of excess Ca^{2+} release due to the left shift of the release activation. The calculated release windows also suggest that the Ca^{2+} release of the YS fibers is activated at lower depolarizing potentials. The voltages at which the peak amplitudes of the release windows of WT and YS fibers are reached were -19.9 and -30.2 mV, respectively.

Figure 33 B illustrates the steady-state baseline Fura-2 ratios (inversely plotted) at the end of every conditioning pulse in WT and YS fibers. This baseline ratios correspond to the free Ca^{2+} level at different holding potentials. The voltage dependence of the steady-state $[Ca^{2+}]$ level in both WT and YS fibers displayed a bell shape. The maximal amplitude of WT fibers is located at -20 mV, while that of the YS fibers is located at -30 mV. On the other hand, the maximal amplitude of WT and YS fibers are similar. Generally, the windows of release of both genotypes are in agreement with the steady-state fluorescence ratios.

Figure 33 C and D show the window of Ca^{2+} current and the normalized window conductance of WT and YS fibers. The window of current is the product of the current density curve (Figure 30 B) and normalized current availability curve (Figure 32 C). The red dashed line represents the supposed window of current if the current availability curve of the YS fibers had not shifted to more negative potentials. The peak amplitude of the window current of the YS fibers is about 50% that of the WT fibers. However, this window current would be nearly 3-fold larger if the voltage dependence of the current availability was the same as in the WT fibers. The voltages at which the maximal window amplitudes are reached is similar in WT (-4 mV) and YS fibers (-7.7 mV). Figure 33 D illustrates the normalized steady-state window of conductance calculated by multiplying the mean fractional conductance and the mean availability curves in WT and YS fibers. This result confirms that for the experimental conditions used here, the availability properties of the DHPR in the YS fibers are altered as a result of the YS mutation in RyR1.

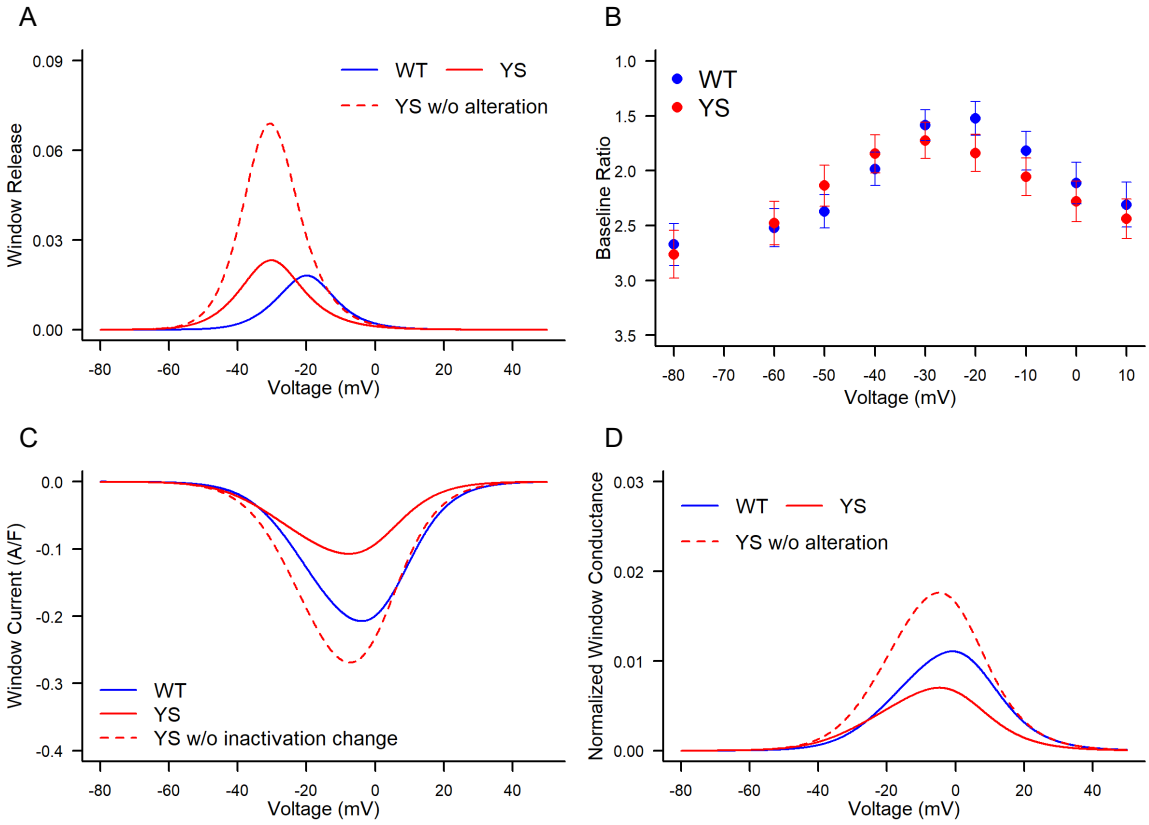

Figure 33: Windows of Ca^{2+} release and Ca^{2+} current generated from activation and availability curves. (A) The window of Ca^{2+} release is the result of multiplying the unnormalized Ca^{2+} activation signals (not shown) with the normalized availability curves (Figure 32 E) from each genotype. The bell-shaped release window of YS fibers exhibits a left shift of about 10 mV of the voltage dependence compared to the WT while the peak level is almost unchanged. The red dashed line represents the theoretical window release of YS for the case that only the activation curve was left shifted while the availability curve remained the same. **(B)** The steady-state baseline Fura-2 ratio levels at the end of every conditioning pulse (indicating free $[Ca^{2+}]$) corresponding to different holding membrane potentials of the inactivation protocol (Figure 32 A) obtained from WT (n=12) and YS (n=15) fibers (inversely plotted). **(C)** The window of current is the product of the activation curve of current density and normalized current availability curve. The red dashed line represents the supposed window current of YS if the current availability curve of the YS fibers had not shifted to more negative potentials. **(D)** The normalized window of conductance is calculated by multiplying the mean fractional conductance and the current availability curves in WT and YS fibers respectively. The red dashed line represents the supposed normalized conductance of YS if the current availability curve of the YS fibers had not shifted to more negative potentials.

4 Discussion

In this dissertation, two mouse models with separate mutations in DHPR (NC) and RyR1 (YS) respectively were studied to better understand the inactivation of calcium channels in the skeletal muscle.

4.1 Non-conducting DHPR mutation in mouse

In the first part, the e-c coupling properties in the NC mouse model which lacks L-type Ca^{2+} current were investigated. Specifically, the experiments were focused on: Ca^{2+} release properties, the SR store content and the inactivation of the channel. The results can be briefly summarized as: (i) Ca^{2+} release properties are not altered; (ii) SR Ca^{2+} content is not affected by the mutation; (iii) at reduced $[Ca^{2+}]_e$, the voltage-dependence of the availability in NC is left-shifted more than in the WT.

It has been widely accepted that the L-type inward Ca^{2+} current is not a necessity for skeletal muscle e-c coupling. Many early studies have addressed this concept with experiments using frog skeletal muscles. Both reducing the external $[Ca^{2+}]$ to the nano-molar range with EGTA (Lüttgau and Spiecker, 1979) or pharmacologically blocking the Ca^{2+} entry (Gonzalez-Serratos et al., 1982) did not seem to affect the performance, i.e., the e-c coupling of the skeletal muscle. On the other hand, there have been other suggestions of what physiological (Brum et al., 1988b) functions this Ca^{2+} influx might be involved in, for example, the calcium-induced calcium release (CICR) mechanism. CICR is a process that can activate massive Ca^{2+} release from the SR by Ca^{2+} alone, without any other stimulations (Endo, 2009; Endo et al., 1970; Ford and Podolsky, 1970). But it is rather unlikely that this slow inward current still serves a functional role in CICR based on experiments comparing the Ca^{2+} release and Ca^{2+} current at extremely low free $[Ca^{2+}]$ that restricted the L-type current (Armstrong et al., 1972; Brum et al., 1988b). It is also activated after the Ca^{2+} release from the SR, and the Ca^{2+} influx is much smaller than the SR Ca^{2+} release. The same could be assumed regarding the involvement of the L-type current in other rapid Ca^{2+} entry mechanisms, for instance, SOCE (Edwards et al., 2010) and action potential-activated Ca^{2+} influx (Launikonis et al., 2009).

4.1.1 Absence of Ca^{2+} current

The knock-in mouse model N617D is non-Ca^{2+}-conducting due to the single amino acid swap from asparagine (N) to aspartic acid (D) in the pore loop II of the α_{1s} subunit in the

DHPR which is adjacent to the selectivity filter. This type of non-conducting DHPR was first discovered in zebra-fish skeletal muscle (Schredelseker et al., 2010) then genetically engineered into the murine genome as a point mutation. The group who created this mouse model has demonstrated the absence of Ca^{2+} current through the DHPR in myotubes (Dayal et al., 2017). It is also confirmed through the tsA201 cells expressing $Ca_v1.1$-N617D channels, that no inward Ca^{2+} current was present (Perni et al., 2017). These observations are consistent with my results on the adult muscle fibers as shown in Figure 23 B, C, and Figure 27 C, D. The absence of the current in the adult muscle fibers confirms N617D is a non-conducting mutation when engineered into mice. Despite the lack of Ca^{2+} influx, the NC mice didn't display any pathological phenotypes and showed normal development in terms of body weight, fertility and locomotor activity (Dayal et al., 2017). These results strongly suggest that the development of the mice does require L-type Ca^{2+} influx.

On the contrary, mice expressing another mutant non-Ca^{2+}-conducting $Ca_v1.1$ channel, the E1014K (abbreviated as EK), permitted outward monovalent current (Beqollari et al., 2018; Lee et al., 2015). Without the Ca^{2+} permeation and binding, the EK mice gain more body weight and body fat percentage with the same food intake and activity levels compared to the WT mice. It was also found that the metabolic rate is decreased as well as heat production in a cold environment (Georgiou et al., 2015).

The discrepancy between the phenotypes of the two genetically modified mouse models very likely originates from the difference in Ca^{2+} binding at the pore. Although both mutant channels don't allow Ca^{2+} permeation, the $Ca_v1.1$ N617D facilitates Ca^{2+} binding at the pore, due to the introduction of a negative charge (Aspartic acid) close to the selectivity filter (Dayal and Grabner, 2016). On the other hand, the $Ca_v1.1$ E1014K hinders the Ca^{2+} binding to the pore. The binding affinity at the pore is very different for these two mutant channels (Beqollari et al., 2018).

4.1.2 Unaltered Ca^{2+} release properties

The Ca^{2+} release-related properties give information about the functionality of e-c coupling. The results obtained in this dissertation (Figure 24 and Figure 25) demonstrated no significant changes in normalized flux (peak or plateau), normalized SR permeability (peak or plateau), the ratio of permeability peak/plateau and time-to-peak values between NC and WT channels. These results represent no alterations in e-c coupling caused by the N617D mutation.

Muscle physiology, development, and performance were also explored in NC mice, including twitch force, tetanic force and fatigue in EDL as well as Soleus muscles. No

significant differences were observed compared to the WT (Dayal et al., 2017). Collectively, these data support the hypothesis that eliminating the L-type Ca^{2+} current does not affect the skeletal muscle e-c coupling.

However, the studies on the $Ca_v1.1$ E1014K mutation revealed different results. The muscles displayed increased sensitivity to fatigue, decreased muscle fiber diameter and increased fast twitch type IIb fiber distribution (Lee et al., 2015). The discrepancy can be attributed to the monovalent permeability of the EK channels. The reported outward Cs^+ current might not be meaningful, due to the negligible level of internal Cs^+ concentration in a physiological condition of the skeletal muscle. However, a recent study has shown that the EK channel conducts outward K^+ current under physiological condition, which could be phenotype-causative (Beqollari et al., 2018). Since accumulation of K^+ ions in the T-tubule can lead to earlier fatigue (Allen et al., 2008; Cairns et al., 1997; Sejersted and Sjøgaard, 2000), Beqollari *et al.* 2018 suggest that the Cav1.1 E1014K channels function as K^+ channels during prolonged depolarization that can eventually lead to pronounced fatigue phenotype.

4.1.3 Unaltered SR store content

The myoplasmic Ca^{2+} homeostasis is of great importance to the skeletal muscle e-c coupling. Ca^{2+} entry from extracellular space makes its contribution via two distinct mechanisms, Excitation-coupled Ca^{2+} entry (ECCE) and store-operated calcium entry (SOCE) (Dirksen, 2009). The skeletal L-type Ca^{2+} current was identified as the primary source of ECCE (Bannister et al., 2009b), which is activated by depolarization (Cherednichenko et al., 2004; Hurne et al., 2005). SOCE is the Ca^{2+} entry activated by the store Ca^{2+} depletion (Rosenberg 2009), it might be affected by the change in the L-type Ca^{2+} current as well. Therefore, the absence of the L-type Ca^{2+} current may lead to an imbalance of the intracellular Ca^{2+} levels. Any alternations in ECCE and SOCE could also affect the SR Ca^{2+} store. It was suggested that the voltage-gated Ca^{2+} influx through the L-type channel contributes to the Ca^{2+} loading of the SR (Robin and Allard, 2015).

Surprisingly, the result of the SR store content experiments (Figure 26 C) did not seem to display any change caused by the N617D mutation which abolishes the L-type Ca^{2+} current. It has also been reported that the NC mice behave similarly to the WT in whole animal muscle endurance and strength tests (Dayal et al., 2017). Together these findings all suggest that the skeletal muscle development of the NC mice doesn't require the Ca^{2+} entry via ECCE.

The proteins involved in SR store refilling via SOCE and other pathways were quantified by Dayal et al. as well, including STIM1, Orai1, SERCA1, CSQ1, TRPC1. The results demonstrated no upregulation of SOCE in the absence of ECCE, which agrees with the above finding on SR store content.

4.1.4 Steady-state fluorescence ratios and release window

The Ca^{2+} influx through the $Ca_v1.1$ upon depolarization is involved in the cytosolic Ca^{2+} homeostasis. The absence of this influx might raise questions about the resting free Ca^{2+} level. And the level of resting steady-state free Ca^{2+} concentration is crucial to the health of the muscle fibers (Canato et al., 2015; Gommans et al., 2002; Vallejo-Illarramendi et al., 2014).

In 10 mM external calcium, the steady-state fluorescence ratios (reflecting free Ca^{2+}) display bell-shaped voltage dependence (Figure 29 C) which corresponds well to the window curves (Figure 29 A) – both peak around -20 mV. The window curves were calculated from the mean unnormalized Ca^{2+} release activation curves (not shown in the figures) and mean fractional availability curves (red and blue solid lines in Figure 28 A). The steady-state fluorescence ratios in Figure 29 C show similar calcium levels in the cells of NC compared to WT fibers. However, there is a discrepancy between the maximal amplitude of the window curves from WT and NC fibers: the maximum of the NC window curve is about 55% that of the WT window curve, and slightly left-shifted.

The cause of this discrepancy in the window curves between WT and NC originates mainly from the discrepancy in the amplitudes of their activation curves. Although statistically insignificant, the differences in maximal amplitudes of the unnormalized activation curves can lead to the differences in maximal amplitude of the window curves. The amplitudes of the activation curves are dominant factors in the amplitudes of the window curves. Secondly, the difference in the steepness of the normalized availability curves also contribute to the difference in the window curves. The availability curve of the NC cells is steeper than the WT, which may have caused the left shift in the window curve. Other parameters involved in the window curves are identical between WT and NC channels.

The steady-state free Ca^{2+} at different holding potentials represented by the steady-state fluorescence ratios shows a different case: there is no statistical significance in any of the data points between different genotypes. It can be supported by the collection of other results in this section. If the releasable Ca^{2+} content in the SR, as well as the release properties of the channels (release flux, permeability) are identical in WT and NC fibers, the steady-state Ca^{2+} levels at various holding potentials should be too.

In 0.1 mM external Ca^{2+}, the voltage dependence of the baseline fluorescence ratios is much different from that in 10 mM. Firstly, the fluorescence ratios from both WT and NC fibers (Figure 29 D) decreased significantly compared to the values at the high external Ca^{2+} concentration. Secondly, the baseline ratios display almost no changes to the increasing membrane holding potential. The result that reduced external Ca^{2+} resulted in reduced cytosolic Ca^{2+} level is no surprise because in the steady state, the free cytoplasmic Ca^{2+} concentration should always be determined by the concentration in the large external Ca^{2+} pool (Ríos, 2010). In addition, according to the recent study on voltage sensors in mammals (Ferreira Gregorio et al., 2017), charge 2 mode is dominant under very low or no external Ca^{2+}, meaning that the DHPR voltage sensors are largely in their inactivated state and the contribution of Ca^{2+} release flux would be much reduced. This offers an explanation of why the steady-state free Ca^{2+} is not fluctuating according to changes in the holding potential.

The predicted release windows under 0.1 mM (Figure 29 B), similarly, have also decreased in amplitudes compared to in 10 mM external Ca^{2+}. The maximal window of the WT is reduced to 50%, and NC to 25% of before. Meanwhile, the maximal window of the NC under 0.1 mM is only about 25% that of the WT cells. This partly contradicts the observations on the steady-state fluorescence ratio.

One factor that may have contributed to the difference between window curves, which are supposed to predict the free Ca^{2+} level, and the steady-state fluorescence ratios is that all activation curves are measured at -80 mV holding potential. Ideally, the activation curves should be held at various potentials. Due to the difficulty to obtain good quality measurements, all activation protocols were performed at -80 mV holding potential. The window curves were constructed with the assumption that activation curves at -80 mV can represent the case at other holding potentials very well. However, if that is not the case, the window curves calculated here might not be able to reflect the true steady-state Ca^{2+} level precisely.

Overall, the NC mutation doesn't seem to affect the cytosolic steady-state free Ca^{2+} in either 10 mM or 0.1 mM of extracellular Ca^{2+}.

4.1.5 Inactivation of the Ca^{2+} channel and Ca^{2+} binding sites

In skeletal muscle, the $Ca_v1.1$ voltage sensor is responsible for two critical gating functions: the L-type Ca^{2+} influx through DHPR and the Ca^{2+} release through RyR1 of the sarcoplasmic reticulum. In NC fibers, the L-type Ca^{2+} current can no longer be measured due to the Ca^{2+} non-permeability of the channel pore. The result in Figure 27 C and D clearly

demonstrates the loss of Ca^{2+} current in mutant channels. Since the e-c coupling process is unaffected, it is sensible to predict that the charge movement of the voltage sensors must be intact. Although the time resolution of the current measurements is not optimal for recording and analyzing the charge movement, they can still be seen in the representative traces in Figure 27 C after removing the capacitive current from the raw current. However, to quantify the charge movements in a precise manner, it requires more detailed analysis.

Since the L-type Ca^{2+} current from WT and NC can't be directly compared, I assessed the availability by observing the Ca^{2+} release from the SR. There are two processes contributing to the decline of Ca^{2+} release from the SR during depolarization: depletion of the SR store and inactivation. From studying the slow phase of recovery of Ca^{2+} release, it was concluded that SR depletion was the cause of slow decline after the peak (Schneider et al., 1987). Availability discussed here, from the measured cytosolic Ca^{2+} signals under the inactivation protocol, is a combination of voltage-dependent inactivation and depletion of the SR (Melzer, 2013). It was reported that SR depletion takes place prior to the voltage-induced inactivation of the RyR and can largely reduce the SR content (Royer et al., 2008; Ursu et al., 2005). Another study pointed out that the SR depletion is responsible for the progressive decline of voltage-dependent Ca^{2+} release activation under prolonged depolarization, especially at small depolarizations (Robin and Allard, 2013).

Figure 27 F illustrated the Ca^{2+} release from the SR at different conditioning membrane potentials of WT and NC fibers at high (10 mM) external [Ca^{2+}], which revealed identical mid-voltage but significantly different slope factor k according to the fitting curves. The NC channels displayed stronger voltage-sensitivity without altering the mid-voltage of the release availability. It is possibly due to the additional negative charge of the aspartic acid introduced to the near SF region in the mutant channel that reportedly changed the binding affinity of the Ca^{2+} binding sites in the pore (Dayal and Grabner, 2016).

In the relatively well-studied voltage-activated K^+ channels, there are two distinct types of inactivation mechanisms showing very different gating properties: N-type and C-type (Armstrong and Hollingworth, 2018; Hoshi et al., 1990b). The N-type inactivation is fast with a time constant of a few milliseconds and relies on the N-terminal domain (Hoshi et al., 1990a). The C-type inactivation is much slower and is tightly associated with the outer carbonyl ring of the SF. The skeletal muscle L-type Ca^{2+} channel displays only characteristics of the C-type inactivation in terms of its voltage dependence and the kinetics.

It was reported in the *Shaker* potassium channels, that the molecular structure at the outer mouth of the SF is especially important to the C-type inactivation. Mutations at position T449 in *Shaker*, which corresponds to location N617 in $Ca_V1.1$, have been extensively

investigated. The T449C mutation displayed a drastic change in Cd^{2+} binding affinity in the inactivated state, which suggested that a conformational change at the outer mouth of the pore is involved in C-type inactivation (Yellen et al., 1994). It is debatable whether the diameter of the external site of the pore decreases offering high affinity binding when inactivated or increases which destroys the ability to bind K^+ ions (Hoshi and Armstrong, 2013). The K^+ binding sites located in the SF are crucial to K^+ conduction and inactivation. Mutations in this region can profoundly alter the gating behavior including inactivation. For instance, mutation at position 378 in potassium channel caused a reduction in the inward K^+ conductance, supposedly due to the partial neutralization of the negative charge (Kirsch et al., 1995). The W434F mutation abolishes the K^+ conductivity of the channel completely (Perozo et al., 1993), while this residue was suggested to form interactions within the selectivity filter and/or its surrounding scaffolding (McCoy and Nimigean, 2012). Several Mutations at T449 have produced changes in the inactivation kinetics and the interaction with monovalent ions (Lopez-Barneo et al., 1993).

Like in potassium channels, there are also Ca^{2+} binding sites within the pore region of Ca^{2+} channels. Yang and colleagues proposed that the four glutamate residues forming the SF are acting as Ca^{2+} binding sites (Yang et al., 1993). These binding sites can either bind one Ca^{2+} ion with high affinity which results in low Ca^{2+} permeation or two Ca^{2+} ions simultaneously with low affinity which allows high Ca^{2+} permeation. In a more recent study, a set of three Ca^{2+} binding sites – two of high affinity and one of low affinity, was identified in a converted Ca_vAb channel: the key SF residues of a voltage-gated bacterial Na_vAb channel were replaced that subsequently altered its ion selectivity (Tang et al., 2014). The three identified binding sites are D178, D177, and T175 in the Ca_vAb channel, which are equivalents of the position 615, 614 and 612 in the pore loop II of the $Ca_v1.1$ (Tang et al., 2014; Wu et al., 2015). The mutation introduced to the NC mouse model is at the position 617 which is located very close to the suggested binding sites but situated closer to the outer mouth of the SF. Furthermore, it was discovered that the M181 residue in the converted Ca_vAb also caused calcium non-permeability by blocking the Ca^{2+} ion with tighter binding to Site 1 (D178) (Tang et al., 2014).

In another study that focused on the SF of the voltage-gated sodium channel Na_vRh, the residue E183 was identified as a strong Ca^{2+} binding site, which is the equivalent the location of the N617D mutation in $Ca_v1.1$ (Zhang et al., 2013). Calcium ions are highly likely to be trapped at negatively charged E183, which consequently blocks both Na^+ and Ca^{2+} from entering the SF. Glutamic acid (E) and aspartic acid (D) residues both carry a negative charge. Although there is still no final agreement on the numbers and locations of the calcium ion binding sites in the SF of the $Ca_v1.1$ channel (Wu et al., 2016; Wu et al., 2015),

it is reasonable to speculate that the introduction of a negatively charged aspartic acid residue at the outer ring of the SF can alter the affinity of the existing Ca^{2+} binding sites.

Experiments using different Ca^{2+} ion concentrations to block the Li^{+} current through normal and mutant $Ca_v1.1$ offered insight of the Ca^{2+} binding affinity at the pore of the N617D mutant channel (Dayal and Grabner, 2016). In the absence of external Ca^{2+} ions, Ca^{2+} channels conduct large monovalent current (Hess and Tsien, 1984). A small concentration (µM range) of external Ca^{2+} can block these currents by high affinity binding to the pore region (Almers et al., 1984; Yang et al., 1993). The mutant channel blocks Li^{+} current more effectively indicating higher affinity binding at the Ca^{2+} binding sites.

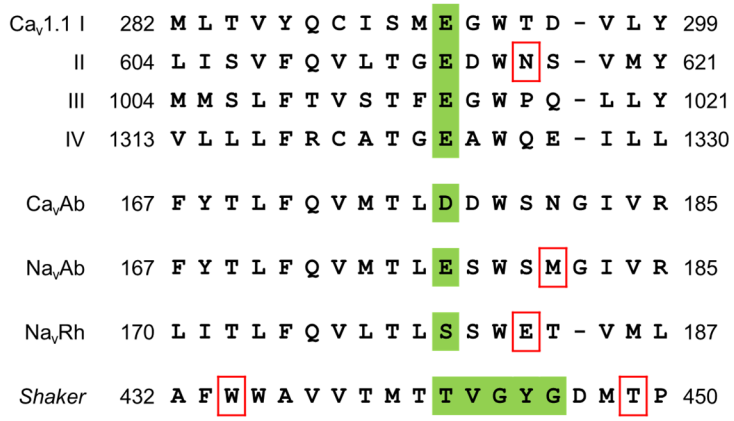

Figure 34: The selectivity filter sequence alignments of the mouse $Ca_v1.1$, Ca_vAb, Na_vAb, Na_vRh, and *Shaker* K^{+} channels. The critical EEEE (Glu292, Glu614, Glu1014, and Glu1323) in $Ca_v1.1$ and the corresponding residues from Ca_vAb, Na_vAb and Na_vRh channels, as well as the selectivity filter of the *Shaker* channel are shown in green boxes. The point mutation introduced to the NC mouse model used in this dissertation is marked with a red box, at position 617 an asparagine is replaced by the negatively charged aspartic acid. In Na_vAb, the M181 residue which caused calcium non-conductivity when converted to Ca_vAb is outlined in a red box. In Na_vRh, the E183 residue which traps calcium ions and blocking both Na^{+} and Ca^{2+} from entering the SF is outlined in a red box. The W434F mutation in *Shaker* that caused non-conductivity of the channel and the T449 residue which corresponds to the N617 in $Ca_v1.1$ are outlined in red boxes (Drawn based on information from Dayal et al., 2017; McCoy and Nimigean, 2012; Tang et al., 2014; Zhang et al., 2013.)

4.1.6 Effect of the extracellular Ca^{2+} on activation and availability

Although the availability curves of Ca^{2+} release of NC and WT cells displayed similar characteristics at high Ca^{2+} concentration (10 mM), an interesting result was discovered when extracellular calcium concentration was reduced to 0.1 mM. The mid-voltages of the Ca^{2+} release activation curves were left-shifted by about 6 mV and 7 mV for WT and NC cells respectively (Figure 28 B). In contrast, the mid-voltages of the Ca^{2+} release availability curves were found to be shifted by about 13 mV and 20 mV to more hyperpolarizing potentials, respectively (Figure 28 A). The differences in the voltage-dependence (both

activation and availability) between 0.1 mM and 10 mM external [Ca^{2+}] were highly significant for both genotypes. Moreover, a change in the steepness of the availability voltage dependence was noticed when external [Ca^{2+}] was reduced, as for both WT and NC the slope factor (k) increased (steepness decreased). In addition, a significant difference emerged in the voltage dependence of the release availability between the WT and NC channels under 0.1 mM external calcium.

A reduction in extracellular calcium concentration was reported to left shift the steady-state inactivation of Ca^{2+} channels in frog muscle fibers (Brum et al., 1988b; Lüttgau and Spiecker, 1979; Schnier et al., 1993). On the other hand, the same change in extracellular calcium concentration has caused no or little effect on the activation voltage dependence (Lüttgau and Spiecker, 1979; Melzer et al., 1995). From the perspective of surface potential theory, it is proposed that Ca^{2+} binds to and screens negative surface charges at the outside of the membrane. When the concentration of external calcium ions decreases, the outside surface becomes more negative (less screening), and therefore the potential difference seen by intramembrane voltage sensors is more depolarized. As a consequence, this induces negative shifts to the steady-state voltage dependence of gating (Hille, 1992). In the experiments performed in this dissertation, the removed external Ca^{2+} ions were replaced by Mg^{2+} ions, to maintain the total concentration of divalent ions. However, it has been reported that the Mg^{2+} ions are not as effective as Ca^{2+} ions in screening and binding surface charges (Dörrscheidt-Käfer, 1976; Dulhunty and Gage, 1989; Hahin and Campbell, 1983), which could explain the negative shifts partially in all curves. The milder left shift in activation than inactivation could mean that surface charges are not equally distributed and may, therefore, affect activation differently than inactivation.

Alternatively, it can be explained with the additional specific effect Ca^{2+} has on inactivation as described below. Two different voltage sensor charge movements can be measured depending on the holding potential (Adrian and Almers, 1976; Almers, 1975). When the fiber is held negative to or at normal holding potential, the charge movement during depolarization is called charge 1. If the fiber is held at depolarizing potentials, charge movements are only measurable at very negative potentials and then called charge 2. In frog muscles, the voltage-sensing modules (VSM) of $Ca_v1.1$ channel which are responsible for voltage-dependent activation (causing a gating charge movement: charge 1) are altered in their voltage dependence by inactivation (conversion to charge 2) (Brum and Ríos, 1987; Pizarro et al., 1989; Ríos and Pizarro, 1991). This process is affected by the reduction or removal of external calcium ions favoring inactivation, converting from charge 1 to charge 2 mode (Brum et al., 1988a). Recently, the dependence of charge displacement on extracellular calcium concentration was studied in two mouse strains (Ferreira Gregorio et

al., 2017). It was the first time that the effect of removing extracellular calcium on inactivation was confirmed in mammals. It was shown that the removal of external Ca^{2+} shifted the voltage dependence of the charge movement to more negative potentials (i.e. conversion from charge 1 to charge 2 favoring inactivation as in frog muscle). The results I obtained in WT are consistent with this study – a substantial negative shift of the mid-voltage of inactivation when extracellular calcium is reduced.

Interestingly, in my results, the reduction of external [Ca^{2+}] from 10 mM to 0.1 mM caused a significantly greater left shift of the availability curves in the NC than in WT cells. At first glance, this seemed like the opposite of what one would expect, considering that the mutation provides a stronger binding at the Ca^{2+} binding sites. Here is the first possible explanation: if the model proposed by Brum and Rios is precise in describing voltage sensor charge movements, in which the removal of external Ca^{2+} promotes voltage sensor inactivation, then the NC mutation should cause a right shift of the voltage dependence of charge 2 (inactivation). Due to the tighter Ca^{2+} binding, the $[Ca^{2+}]_e$ should be "sensed" as higher in NC fibers than it is in WT. However, it is important to be reminded that the measurements I acquired are availability curves, under the influence of both voltage-dependent inactivation and depletion. Depletion is very likely the dominant factor during small steady depolarizations (Robin and Allard, 2013). A right shift in the voltage dependence of the inactivation while the activation remains unchanged results in a larger release window, which subsequently leads to a stronger depletion of the SR. The stronger depletion would cause the availability curve to shift to the negative direction as it appeared in the results.

A second explanation emerges from a closer look at the molecular structure of the SF and the Ca^{2+} binding sites. The N617D mutation, situated at the outer side of the SF of the $Ca_v1.1$, can potentially trap Ca^{2+} ions from the external side before they reach the binding sites further down the vestibule of the SF. When the external [Ca^{2+}] is as high as 10 mM, the effect of the altered binding affinity may not play an important role. But under reduced [Ca^{2+}], the negatively charged aspartic acid can bind to the Ca^{2+} more tightly at Position 617, making it less likely for Ca^{2+} to bind to the binding sites that are involved in the voltage-dependent inactivation. Under this assumption, the external [Ca^{2+}] would be "sensed" as lower in the NC compared to the WT. Then the NC cells would show a more pronounced left shift of the voltage dependence of the inactivation when the external [Ca^{2+}] is reduced.

Alterations in the properties of C-type inactivation due to mutations adjacent to the selectivity filter have been observed in voltage-gated *Shaker* K^+ channels as well. For instance, the W434F mutation, when introduced in one or two of the subunits in a tetrameric construct of the *Shaker* 29-4 channel, was reported to shift the voltage dependence of the

inactivation to more negative potentials while leaving the activation properties unchanged (Yang et al., 1997). The effect of external K^+ concentration on the inactivation time course was also changed by this mutation. Different mutations at the T449 location in *Shaker*, the equivalent position of N617 in $Ca_v1.1$, displayed significant slowing down of the inactivation time course at high external [K^+] while no noticeable changes were observed in the activation kinetics. Higher external [K^+] also produced larger amplitude of the K^+ current despite of the reduced driving force for K^+ current. It is argued that external K^+ places the channel from C-type inactivation to a state that it can be opened (Lopez-Barneo et al., 1993).

The findings regarding the effect of external [Ca^{2+}] on availability curves, especially the additional left shift observed in the NC fibers are very interesting at the same time surprising. Although it is still hard at this point to determine which possible explanation is the actual underlying cause of that, these results provided good foundation for further investigations. Measuring and analysing inactivation charge movements at low external [Ca^{2+}] will be helpful to better understand the inactivation mechanism. Other hypotheses other than the two discussed above are also not excluded.

4.2 Retrograde signaling in a mouse model with MH

The second part of this dissertation focuses on the previously reported alteration in the Ca^{2+} current inactivation of the MH mouse model Y524S. Malignant hyperthermia (MH) is a genetic skeletal muscle disorder, which is caused by mutations originating from the RyR1 gene (coding RyR1) and CACNA1S gene (coding DHPR). In the majority of the cases, the MH-causing mutation is located in the RyR1 gene (Rosenberg et al., 2015). The Y524S mouse model carries the MH causative mutation in the RyR1, but surprisingly, also alters the gating function of the DHPR (Andronache et al., 2009; Chelu et al., 2006). The objective was to investigate whether the altered Ca^{2+} release caused by the mutation contributes to the alteration in the voltage dependence of the inactivation of the DHPR. Following SR depletion conditions were applied to deplete the SR and to prevent acute effects of Ca^{2+} release on the DHPR: no Ca^{2+} was added into the internal solution, BAPTA was used as Ca^{2+} buffer for faster binding, and SERCA blocker was applied to reduce SR refilling. As a result, the alteration in the voltage dependence of the availability current persists under supressed Ca^{2+} transients. This suggests that internal Ca^{2+} elevation is most likely not the cause of the DHPR gating alteration in the YS mouse; other candidates should be studied to understand the mechanism of retrograde signalling.

4.2.1 Ca^{2+} release and current activation under SR depletion conditions

Uncontrolled Ca^{2+} release via RyR1 from the SR in the skeletal muscle is the start of an active MH event which then leads to a fulminant hypermetabolic reaction of the body (MacLennan and Zvaritch, 2011). The mutation caused disruption in the intracellular Ca^{2+} homeostasis primarily by increasing the probability of RyR to open (p_{open}) (Ríos et al., 2015). Prior studies using the YS mouse model observed a left shift in the voltage dependence of the Ca^{2+} release activation curve (Andronache et al., 2009; Manno et al., 2013), demonstrating the increased voltage sensitivity of YS mutant channels. Different cytosolic Ca^{2+} transient kinetics were also found. Muscle fibers expressing mutant channels display a sharper peak of Ca^{2+} flux and less time to reach the peak. (Andronache, 2008; Manno et al., 2013).

This is suggested to be related to the calcium-induced calcium release (CICR). Unlike in healthy muscles, CICR takes on a more critical role in e-c coupling of skeletal muscle with MH. Patients or animal models with MH demonstrated increased calcium sensitivity of CICR and elevated maximum Ca^{2+} release rate (Endo et al., 1983; Kawana et al., 1992; Ohta et al., 1989). The presence of BAPTA limits the rise of the myoplasmic Ca^{2+} concentration, which subsequently reduces the CICR and also calcium-dependent inactivation (CDI), ultimately affecting the Ca^{2+} release kinetics (Endo, 2009; Ríos, 2018).

A number of studies explored the influence of Ca^{2+} buffers on Ca^{2+} release signals. When directly injected into the frog skeletal muscle fiber, BAPTA eliminated the abrupt local [Ca^{2+}] increase upon the activation of RyR1 due to its strong buffering capacity. Its presence removed the early peak and the sharp decline of the Ca^{2+} release flux without affecting the final equilibrium level (Jacquemond et al., 1991). The affinity of BAPTA for Ca^{2+} is similar to that of EGTA, however, its binding kinetic to Ca^{2+} ions is a lot faster. When comparing BAPTA buffered Ca^{2+} release signals to EGTA buffered signals, BAPTA speeded up the Ca^{2+} release process, resulted in a peak release flux rate at least twice of that from the EGTA signals, and decayed much faster to a lower steady level, leaving a sharper flux peak (Sztretye et al., 2011). The Ca^{2+} release flux from WT fibers buffered with BAPTA highly resembled the changes caused by the YS mutation. Using BAPTA as the Ca^{2+} buffer altered the Ca^{2+} release flux properties of WT channels to behave like YS mutants, but at the meantime not affecting the voltage dependence of the voltage sensor as the mutation did (Manno et al., 2013). It can eliminate the potential effects that have been caused by the difference in Ca^{2+} release kinetics.

Although Ca^{2+} release flux form transients measured with BAPTA are not analysed in this dissertation due to the lack of information needed for the “removal model analysis”

(Schuhmeier and Melzer, 2004), the background-corrected Fura-2 fluorescence ratios are presented in Figure 31 A. Comparing to the signals from a cell loaded with EGTA buffered internal solution, it is shown that BATPA can bind to Ca^{2+} much faster, therefore is able to eliminate the effects caused by abrupt change of free Ca^{2+} level.

With regard to the voltage dependence of the Ca^{2+} release activation, the mean mid-voltage of the mutant channels is 11 mV more negative than the WT channels. The corresponding value was 8 mV in the findings of Andronache et al., and 5 mV by Manno et al.. The slope factor parameter of the fits from WT and mutant channels are comparable. The data shown in Figure 31 B is obtained by analyzing the fluorescence signals at the end of the 100 ms test pulse in the activation protocol, where the Ca^{2+} signals exhibit a relatively low and steady level. Therefore, this data is more comparable to the data describing the plateau of the release flux rather than the peak of the flux in the previous studies. The mid-voltages of both WT and YS fibers are more negative than in the observations in Andronache et al., 2009. Additionally, the slope factors (k) of the activation curves are steeper than those of Andronache et al. for both WT and mutants.

One possible explanation is that the BAPTA in the internal solution caused a higher potential of the RyR1 opening. According to the model proposed in an earlier study on MH, that can result in a left shift in the voltage dependence of the Ca^{2+} release (Dietze et al., 2000). A five-state model is used to describe the relationships between different open and closed states of the voltage sensor and the Ca^{2+} releasing channel. It is assumed that the DHPR has 3 states: resting, pre-active and open; the RyR1 has just closed and open state. Both the pre-active and the open state of DHPR can induce the opening of RyR1 with the same equilibrium constant. The model predicts that a decrease of this closed-to-open equilibrium constant of the RyR1 (larger degree of opening at constant voltage) can result in a left shift of the half-maximal activation $V_{1/2}$ of the Ca^{2+} release. If the use of BAPTA caused a larger degree of RyR1 opening at same voltages, it would induce the observed left shift of the voltage dependence of the activation. Apart from the difference in the internal solution compared to Andronache's procedure, the analytical method behind the release activation curve is also different. Fura-2 ratios provided information on the part of the released Ca^{2+} that bound to the fluorescent indicator, which is not identical to the Ca^{2+} flux analyzed by the "removal model" that involves dynamic modeling and simulation.

The Ca^{2+} current activation results from WT and YS channels shown in Figure 30 are qualitatively and quantitatively very close to the published results on the same mouse strain (Andronache et al., 2009). The mid-voltage of the Ca^{2+} activation conductance of the YS fiber was slightly but statistically significantly shifted to more negative potential compared to WT channel, which might contribute to the left shift of the Ca^{2+} release activation curve.

The use of BAPTA instead of EGTA didn't seem to cause any change in the inward Ca^{2+} current from the DHPR.

4.2.2 Release availability curve affected by local [Ca^{2+}] and SR depletion

The control of Ca^{2+} release from the SR is primarily mediated by voltage via a conformational coupling through the DHPR, secondarily also by free Ca^{2+} in the junction (Melzer et al., 1995; Ríos and Pizarro, 1988). It is widely accepted that the II-III loop in the α_{1s} subunit is responsible for the conformational coupling between DHPR and RyR1 (Tanabe et al., 1990). Additionally, several models were introduced aiming to describe the mechanical interaction between the voltage sensor and the Ca^{2+} release channel before (Chandler et al., 1976; Melzer et al., 1986). The allosteric model provided a good theoretical description of the molecular interaction between the DHPR and the RyR1 (Ríos et al., 1993). The model viewed the RyR1 as the allosteric protein which is coupled to four DHPRs that function as its activators. The RyR1 has two states: closed and open, while the four DHPRs undergo voltage-driven activation independently from each other. This model allows changes on the RyR1 to be transmitted to the voltage sensors and produce secondary effects. According to the model, the junctional Ca^{2+} concentration influences the activation and inactivation properties by interacting with different sites (Stern et al., 1997). And the distribution of intracellular Ca^{2+} concentration is a result of the amount of released Ca^{2+} and the binding to fixed and diffusible buffers in the myoplasmic space.

The effects of different buffers on the local Ca^{2+} gradient have been studied extensively (Anderson and Meissner, 1995; Baylor et al., 1983; Csernoch et al., 1993; Jacquemond et al., 1991; Klein et al., 1988; Pape et al., 1998, 1995). The intracellular Ca^{2+} dynamic is sensitive to the affinities and the forward rate constants of the Ca^{2+} buffers. A buffer with rapid binding kinetic as BAPTA in high concentration (10 mM used in my experiments) will be very effective in confining the released Ca^{2+} within in a small distance ranging from the Ca^{2+} releasing cluster (Wu et al., 1996). EGTA, on the other hand, will result in a wider distribution of calcium concentration gradient in terms of the distance from the Ca^{2+} releasing channels. Furthermore, the experimental conditions have been designed to favor SR depletion. Firstly, BAPTA promoted SR depletion and boosted the SR permeability (Manno et al., 2013). Secondly, there were no added calcium ions in the artificial internal solution as additional source. Besides, a blocker of SERCA pumps was used to prevent the Ca^{2+} re-uptake after the release. Finally, a depletion protocol was performed before the measurement of activation and inactivation protocols. The expectation is that the reduced intracellular Ca^{2+} concentration could influence the availability curve to shift to more

negative potentials which is consistent with my observations on the availability curves in Figure 32 E.

The mid-voltages of the release availability curves from both WT and YS fibers moved to the hyperpolarizing direction compared to Andronache's results (Andronache, 2008), while the relative shift between WT and YS remained the same. The steepness of the availability curves also decreased in both cases by about the same. It is to be noted here that different analysis methods were performed compared to Andronache *et al.* 2009, some systematic changes might be attributed to that.

4.2.3 Availability of the Ca^{2+} current and retrograde signalling

One of the key findings from previous studies on the YS mouse model for malignant hyperthermia is that the voltage dependence of the DHPR-mediated Ca^{2+} current availability has been altered, possibly as a protective mechanism against the altered Ca^{2+} release voltage dependence (Andronache et al., 2009). It serves as strong indication for the regulation on DHPR from RyR1. Under the conditions of my experiments, which provided stronger Ca^{2+} buffering and restrict the cytosolic Ca^{2+} level, the alteration on the DHPR current availability persisted. It is shown in Figure 32 C that the mid-voltage of the normalized current availability of YS fibers is about 9 mV more negative than that of the WT fibers. The value of this shift is consistent with the observations from Andronache et al., 2009.

It is known that the interaction between DHPR and RyR1 in the skeletal muscle is bidirectional: an orthograde signal is when the voltage sensor of the DHPR triggers Ca^{2+} release from the SR via RyR1; a retrograde signal is when RyR1 is affecting the gating properties of the DHPR (L-type Ca^{2+} current). The first observation of retrograde coupling was from the mutation found in a dispedic (RyR1-null) mouse model which caused a drastic reduction in the amplitude of the L-type current density (Nakai et al., 1996). A more detailed study discovered that the RyR also modifies the DHPR expression level, voltage dependence, and kinetics of the current (Avila and Dirksen, 2000). Although it is still not clear how retrograde signaling takes place, multiple regions in both channels involved (DHPR and RyR1) have been studied. On the side of the DHPR, it is found that the II-III loop, connecting the 2^{nd} and 3^{rd} repeats, contains essential motifs for orthograde as well as retrograde coupling (Grabner et al., 1999; Wilkens et al., 2001). More investigations were carried out on the RyR1, locating relevant regions that could modulate the activity of DHPR in different manners (Lee et al., 2004; Polster et al., 2018; Protasi et al., 2002; Sheridan et al., 2006). There is evidence that retrograde signaling is independent of the Ca^{2+} release

from the SR (Hurne et al., 2005). Recently, a study on a lethal mutation in the RyR1 E4242G suggested a new model including two separate retrograde signals: one that slowed the activation kinetics and the other enhances the current amplitude (Bannister et al., 2016).

Regulators and influencers of the retrograde coupling have also been studied. For instance, intracellular calcium concentration can modify the interaction between DHPR and RyR1. It was reported that raised $[Ca^{2+}]_i$ caused e-c uncoupling in mammalian as well as amphibian skeletal muscles (Lamb et al., 1995). Furthermore, proteolysis mediated by μ-calpain, a calcium-dependent protease, was found to be responsible for disrupting the communication between DHPR and RyR1 (Murphy et al., 2013; Verburg et al., 2009). Additionally, key regulatory triadic proteins – junctophilin (JP) isoforms 1 and 2 were suggested to function as anchors between the SR membrane and the T-tubule membrane, maintaining the structural integrity of the triad (Ito et al., 2001). The activation of calpain leads to proteolysis of JP1 and JP2, that resulted in a decreased number of DHPRs, reduction of L-type Ca^{2+} current and intramembranous charge movement (Golini et al., 2011; Kanzaki et al., 2017). Some modification of the DHPR or its associated proteins by slightly increased free $[Ca^{2+}]$ in the MH mouse might also be responsible for a retrograde effect.

The results in Figure 32 C revealed differences in the voltage dependence of the Ca^{2+} current availability compared to Andronache et al., 2009. The mid-voltage of both WT and YS fibers moved about 3 mV to the negative potential while maintaining the relative difference between them (9 mV) unchanged. The slope factors of the normalized current curves are less steep for both genotypes. One interpretation regarding the change in the steepness is that BAPTA restricted the calcium ions in a closer ranger around the release channel and minimized a Ca^{2+}-dependent modification of the voltage gating charge in the T-tubule. There are two components of the charge 1, Q_β and Q_γ, with different pharmacology, voltage sensitivity, and kinetics (Adrian and Peres, 1979; Almers et al., 1975). It was suggested that Q_γ could be caused by the Ca^{2+} released from SR: calcium ions bind to the negatively charged sites on the sensor, then affecting the surface potential, causes further activation (Pizarro et al., 1991). Therefore, the kinetics (steepness) of the gating charge could be altered by changes in the internal Ca^{2+} distribution. By reducing this positive feedback loop between released Ca^{2+} and channel activation, the switch from EGTA to BAPTA could cause a less steep voltage dependence.

4.2.4 Ca^{2+} release and current windows

The calculated Ca^{2+} release window shown in Figure 33 A is generated from activation (non-normalized) and availability (normalized) curves of Ca^{2+} signals obtained from fluorescence

ratios. The YS fibers displayed a bell-shaped window curve similar in amplitude compared to the WT. Whereas its voltage dependence and the position of its peak were about 10 mV more negative. The predicted steady-state SR Ca^{2+} leak as a function of holding potential corresponded well to the measured free Ca^{2+} levels indicated by the fluorescence ratios (Figure 33 B). The peak of the mean baseline ratios in the YS fibers was similar in amplitude but appeared 10 mV more negative than the WT. The alteration in the voltage dependence of the RyR1 availability curve of the YS fibers may serve as a protective mechanism to avoid massive Ca^{2+} leak. Without this alteration, the amplitude of the steady-state Ca^{2+} leak would increase to more than 3-fold as the red dashed line in Figure 33 A indicates.

The results obtained in this dissertation are generally in agreement with results from Andronache et al., 2009. The voltage dependences of the release activation and availability in YS fibers appeared to be at more negative potentials than those of the WT. The relative distances from the peaks of the window curves between WT and YS are also similar. The left shift of the availability curve in the YS fibers persisted under SR depletion conditions. My results, therefore, suggest that acute internal Ca^{2+} elevation does not play a key role in the information transfer process that caused alterations in the release availability curve.

There is a difference between the two studies in terms of the position at which the window curves peak. In my results, the voltage dependence in both genotypes were shifted to the right. If BAPTA indeed attenuated the positive feedback mechanism between Ca^{2+} release and the activation of the sensor charge movement as discussed above, the steady-state Ca^{2+} leak should move to higher potentials accordingly. That could explain the right shift of the window curves shown in my results.

A limitation in concluding the involvement of Ca^{2+} in the retrograde coupling based on Ca^{2+} release availability is that the release availability could be strongly influenced by the SR depletion. An early activation (at lower voltages) of the RyR1-mediated Ca^{2+} release caused by the YS mutation, can lead to a more severe SR depletion. As discussed in Section 4.1.6, availability is a combination of voltage-dependent inactivation and SR depletion, in which the latter contributes substantially. It is possible that the stronger shift in the availability curve for the Ca^{2+} signals may result from the lower threshold of activation causing depletion at lower depolarizations.

The L-type current, on the other hand, is a signal closer to the DHPR than the Ca^{2+} signals discussed above and can provide stronger evidence for the retrograde signalling. As a result, the Ca^{2+} current window of the YS fibers also exhibited changes due to the shift of the current availability curve. The peak amplitude of the predicted YS window current was smaller than that of the WT as well as the putative window current, if the Ca^{2+} current

availability curve had not shifted (Figure 33 C red dashed line). The left-shifted current availability curve strongly suggests the action of retrograde signalling, i.e., that RyR1 modifies the gating property of the voltage sensor to limit the Ca^{2+} flux, both from the SR and from the extracellular space, as a compensatory method against the effect of the MH mutation, protecting against a catastrophic Ca^{2+} leak.

Considering the similarity of my results to the results using EGTA as Ca^{2+} buffer from Andronache et al., 2009, it is likely that this specific retrograde signalling pathway does not involve the intracellular Ca^{2+} distribution, at least the short-term effect of it. It cannot be excluded that the elevated cytosolic Ca^{2+} level might have long-term effects on the DHPR's voltage sensors and its gating properties. Modifications on the DHPR might have taken place prior to the experiments and cannot be simply reversed by applying BAPTA or other SR depletion conditions. The studies on retrograde coupling has progressed since two decades, but more investigations should still be carried out in order to decipher the process of signal transmission from Ca^{2+} release channel to its voltage sensor.

5 Summary

The excitation-contraction coupling in mammalian skeletal muscle is unique because of its conformational signaling mechanism. The activation of sarcoplasmic reticulum (SR) Ca^{2+} release via ryanodine receptor 1 (RyR1) is not dependent on the calcium entry but solely on the activation of the voltage sensor. Many questions remain unanswered despite years of research on the direct or indirect interaction between the dihydropyridine receptor (DHPR) and RyR1.

In this dissertation, experiments were designed and carried out to study various aspects of the e-c coupling machinery with a stress on the slow inactivation process using two knock-in mouse models: N617D (NC) and Y524S (YS). NC mice carry homozygously the DHPR mutation N617D discovered in zebrafish, which is responsible for the absence of L-type Ca^{2+} current. YS mice carry heterozygously a malignant hyperthermia (MH) causative mutation in the RyR1, which exhibited altered DHPR inactivation. The L-type Ca^{2+} current was measured with the two-electrode voltage clamp technique, the Ca^{2+} signals were measured using the internally loaded fluorescent indicators Fura-2 or Fura-FF.

In the first part, the NC mouse model with non-conducting $Ca_v1.1$ was used to assess the functionality of the L-type Ca^{2+} current and the effect of the mutation on the voltage-dependent availability. The Ca^{2+} release properties (Ca^{2+} flux, permeability, and kinetics) obtained from a removal model analysis of the NC fibers were similar as in the WT fibers. Additionally, the mutation did not change the Ca^{2+} load in the SR. It was the first opportunity to investigate the adult muscle fibers from animals that lacked L-type Ca^{2+} current.

The influence of the extracellular Ca^{2+} concentration on the Ca^{2+} release activation and availability were studied by comparing measurements under 10 mM and 0.1 mM $[Ca^{2+}]_e$. The results showed almost equal negative shifts in the voltage dependence of the Ca^{2+} release activation in both genotypes. This shift can possibly be attributed to Ca^{2+} ions unbinding from surface charges on the outside of the membrane which is not completely compensated by Mg^{2+} binding.

Availability curves for Ca^{2+} release were stronger left-shifted due to the reduced $[Ca^{2+}]_e$ than the activation curves. A stronger left shift in the availability curve of NC fibers was discovered in 0.1 mM external $[Ca^{2+}]$. It is relevant to the N617D mutation which facilitates stronger Ca^{2+} binding due to the extra negative charge. It may either lower the probability of binding at the pore resulting in the voltage-dependent inactivation to shift to the left; or shift the inactivation to the right according to the metal ion binding theory, causing stronger depletion, then indirectly shift the availability curve to the left.

The window curves in both genotypes under 10 mM external [Ca^{2+}] corresponded well to the steady-state fluorescence ratio measurements. Under 0.1 mM external [Ca^{2+}], the baseline fluorescence ratios displayed little voltage dependence. Overall, the NC mutation did not influence the steady-state Ca^{2+} level.

The second part aimed to test the hypothesis of whether excessive cytosolic Ca^{2+} was involved in the retrograde pathway that has altered the Ca^{2+} signals and current in the MH mouse model Y524S. SR depletion conditions were applied to restrict intracellular Ca^{2+} distribution and to promote depletion: Ca^{2+} free internal solution containing a high concentration of Ca^{2+} chelator BAPTA plus the introduction of the SERCA blocker CPA. A strong slowing down in the Ca^{2+} transient time course was observed resulting from the rapid binding kinetics of BAPTA to Ca^{2+} ions.

The activation curve of the Ca^{2+} release signals displayed a substantial left shift in YS compared to WT fibers, similar to the reported results under less effective Ca^{2+} buffering and is in agreement with the known disrupted Ca^{2+} homeostasis in MH. The Ca^{2+} inward current activation in YS and WT fibers showed the same characteristics.

A negative shift was observed in the availability curve for Ca^{2+} release in the YS fibers. This limited the peak amplitude of the Ca^{2+} release window, avoiding massive Ca^{2+} leak from the SR that would take place otherwise. It may reflect a compensatory mechanism. The YS Ca^{2+} current availability curve also exhibited a negative shift comparing to WT fibers. This argues against that Ca^{2+} feedback from the local Ca^{2+} transient during rapid Ca^{2+} release caused the observed changes in the availability curves of YS fibers. The local Ca^{2+} rise at the mouth of the ryanodine receptor should have been blocked or reduced by the use of BAPTA and CPA.

The fluorescence baseline ratios aligned well with the predicted Ca^{2+} release window and were also left-shifted in YS fibers. The Ca^{2+} current window of the YS was attenuated which restricts the Ca^{2+} influx via the DHPR as a second source of Ca^{2+}. SR depletion conditions did not block the retrograde signalling that caused the alterations in the release and current availabilities in YS fibers.

In summary, this dissertation investigated properties of two key proteins involved in e-c coupling, DHPR and RyR1; provided new insights into alterations of skeletal muscle Ca^{2+} signalling caused by specific mutations with a focus on the voltage-dependent availability. It would require more structural and functional studies to gain a deeper understanding of the determinants and regulators of the voltage-dependent inactivation in Ca^{2+} channels.

6 References

Ackermann, U., 2002. PDQ physiology. BC Decker Inc, Hamilton.

Adams, B., Tanabe, T., Mikami, A., Numa, S., Beam, K.G., 1990. Intramembrane charge movement restored in dysgenic skeletal muscle by injection of dihydropyridine receptor cDNAs. Nature 346 (6284), 569–572. 10.1038/346569a0.

Adrian, R.H., Almers, W., 1976. Charge movement in the membrane of striated muscle. The Journal of physiology 254 (2), 339–360.

Adrian, R.H., Peres, A., 1979. Charge movement and membrane capacity in frog muscle. The Journal of physiology 289 (1), 83–97. 10.1113/jphysiol.1979.sp012726.

Allen, D.G., Lamb, G.D., Westerblad, H., 2008. Skeletal muscle fatigue: Cellular mechanisms. Physiological reviews 88 (1), 287–332. 10.1152/physrev.00015.2007.

Almers, W., 1975. Observations on intramembrane charge movements in skeletal muscle. Philosophical transactions of the Royal Society of London. Series B, Biological sciences 270 (908), 507–513. 10.1098/rstb.1975.0027.

Almers, W., Adrian, R.H., Levinson, S.R., 1975. Some dielectric properties of muscle membrane and their possible importance for excitation-contraction coupling. Ann NY Acad Sci 264 (1), 278–292. 10.1111/j.1749-6632.1975.tb31489.x.

Almers, W., McCleskey, E.W., Palade, P.T., 1984. A non-selective cation conductance in frog muscle membrane blocked by micromolar external calcium ions. The Journal of physiology 353, 565–583.

Anderson, K., Meissner, G., 1995. T-tubule depolarization-induced SR Ca2+ release is controlled by dihydropyridine receptor- and Ca2+-dependent mechanisms in cell homogenates from rabbit skeletal muscle. The Journal of general physiology 105 (3), 363–383.

Andronache, Z., 2008. Voltage-Gated Calcium Fluxes Studied in Skeletal Muscle Fibers of Genetically Engineered Mice. Dr. biol. hum., Dissertation, Medical Faculty, Ulm University.

Andronache, Z., Hamilton, S.L., Dirksen, R.T., Melzer, W., 2009. A retrograde signal from RyR1 alters DHP receptor inactivation and limits window Ca2+ release in muscle fibers of Y522S RyR1 knock-in mice. Proceedings of the National Academy of Sciences of the United States of America 106 (11), 4531–4536. 10.1073/pnas.0812661106.

Armstrong, C.M., Bezanilla, F.M., Horowicz, P., 1972. Twitches in the presence of ethylene glycol bis(β-aminoethyl ether)-N,N′-tetraacetic acid. Biochimica et Biophysica Acta (BBA) - Bioenergetics 267 (3), 605–608. 10.1016/0005-2728(72)90194-6.

Armstrong, C.M., Hollingworth, S., 2018. A perspective on Na and K channel inactivation. The Journal of general physiology 150 (1), 7–18. 10.1085/jgp.201711835.

Armstrong, R.A., 2014. When to use the Bonferroni correction. Ophthalmic & physiological optics: the journal of the British College of Ophthalmic Opticians (Optometrists) 34 (5), 502–508. 10.1111/opo.12131.

Avila, G., Dirksen, R.T., 2000. Functional impact of the ryanodine receptor on the skeletal muscle L-type Ca2+ channel. The Journal of general physiology 115 (4), 467–480.

Avila, G., Dirksen, R.T., 2001. Functional Effects of Central Core Disease Mutations in the Cytoplasmic Region of the Skeletal Muscle Ryanodine Receptor. The Journal of general physiology 118 (3), 277–290.

Bannister, R.A., 2007. Bridging the myoplasmic gap: recent developments in skeletal muscle excitation-contraction coupling. Journal of muscle research and cell motility 28 (4-5), 275–283. 10.1007/s10974-007-9118-5.

Bannister, R.A., 2016. Bridging the myoplasmic gap II: more recent advances in skeletal muscle excitation-contraction coupling. The Journal of experimental biology 219 (Pt 2), 175–182. 10.1242/jeb.124123.

Bannister, R.A., Beam, K.G., 2013. CaV1.1: The atypical prototypical voltage-gated Ca^{2+} channel. Biochimica et biophysica acta 1828 (7), 1587–1597. 10.1016/j.bbamem.2012.09.007.

Bannister, R.A., Papadopoulos, S., Haarmann, C.S., Beam, K.G., 2009a. Effects of inserting fluorescent proteins into the alpha1S II-III loop: insights into excitation-contraction coupling. The Journal of general physiology 134 (1), 35–51. 10.1085/jgp.200910241.

Bannister, R.A., Pessah, I.N., Beam, K.G., 2009b. The Skeletal L-type Ca2+ Current Is a Major Contributor to Excitation-coupled Ca2+ entry. The Journal of general physiology 133 (1), 79–91. 10.1085/jgp.200810105.

Bannister, R.A., Sheridan, D.C., Beam, K.G., 2016. Distinct Components of Retrograde CaV1.1-RyR1 Coupling Revealed by a Lethal Mutation in RyR1. Biophysical Journal 110 (4), 912–921. 10.1016/j.bpj.2015.12.031.

Baylor, S.M., Chandler, W.K., Marshall, M.W., 1983. Sarcoplasmic reticulum calcium release in frog skeletal muscle fibres estimated from Arsenazo III calcium transients. The Journal of physiology 344, 625–666.

Baylor, S.M., Hollingworth, S., 1988. Fura-2 calcium transients in frog skeletal muscle fibres. The Journal of physiology 403, 151–192.

Baylor, S.M., Hollingworth, S., 1998. Model of sarcomeric Ca2+ movements, including ATP Ca2+ binding and diffusion, during activation of frog skeletal muscle. The Journal of general physiology 112, 297–316.

Beam, K.G., Knudson, C.M., Powell, J.A., 1986. A lethal mutation in mice eliminates the slow calcium current in skeletal muscle cells. Nature 320 (6058), 168–170. 10.1038/320168a0.

Bekoff, A., Betz, W., 1977. Properties of isolated adult rat muscle fibres maintained in tissue culture. The Journal of physiology 271 (2), 537–547.

Beqollari, D., Dockstader, K., Bannister, R.A., 2018. A skeletal muscle L-type Ca2+channel with a mutation in the selectivity filter (CaV1.1 E1014K) conducts K. The Journal of biological chemistry 293 (9), 3126–3133. 10.1074/jbc.M117.812446.

Bers, D.M., 2002. Cardiac excitation-contraction coupling. Nature 415 (6868), 198–205. 10.1038/415198a.

Block, B.A., 1988. Structural evidence for direct interaction between the molecular components of the transverse tubule/sarcoplasmic reticulum junction in skeletal muscle. The Journal of cell biology 107 (6), 2587–2600. 10.1083/jcb.107.6.2587.

Boncompagni, S., Rossi, A.E., Micaroni, M., Hamilton, S.L., Dirksen, R.T., Franzini-Armstrong, C., Protasi, F., 2009. Characterization and temporal development of cores in a mouse model of malignant hyperthermia. PNAS 106 (51), 21996–22001. 10.1073/pnas.0911496106.

Brum, G., Fitts, R., Pizarro, G., Ríos, E., 1988a. Voltage sensors of the frog skeletal muscle membrane require calcium to function in excitation-contraction coupling. The Journal of physiology 398, 475–505.

Brum, G., Ríos, E., 1987. Intramembrane charge movement in frog skeletal muscle fibres. Properties of charge 2. The Journal of physiology 387. 10.1113/jphysiol.1987.sp016586.

Brum, G., Ríos, E., Stefani, E., 1988b. Effects of extracellular calcium on calcium movements of excitation-contraction coupling in frog skeletal muscle fibres. The Journal of physiology 398, 441–473.

Cairns, S.P., Hing, W.A., Slack, J.R., Mills, R.G., Loiselle, D.S., 1997. Different effects of raised K+o on membrane potential and contraction in mouse fast- and slow-twitch muscle. The American journal of physiology 273 (2 Pt 1), C598-611. 10.1152/ajpcell.1997.273.2.C598.

Calderon-Rivera, A., Andrade, A., Hernandez-Hernandez, O., Gonzalez-Ramirez, R., Sandoval, A., Rivera, M., Gomora, J.C., Felix, R., 2012. Identification of a disulfide bridge essential for structure and function of the voltage-gated Ca2+ channel alpha2delta-1 auxiliary subunit. Cell calcium 51 (1), 22–30. 10.1016/j.ceca.2011.10.002.

Campbell, K.P., Leung, A.T., Sharp, A.H., 1988. The biochemistry and molecular biology of the dihydropyridine-sensitive calcium channel. Trends in Neurosciences 11 (10), 425–430. 10.1016/0166-2236(88)90193-2.

Canato, M., Capitanio, P., Reggiani, C., Cancellara, L., 2015. The disorders of the calcium release unit of skeletal muscles: what have we learned from mouse models? Journal of muscle research and cell motility 36 (1), 61–69. 10.1007/s10974-014-9396-7.

Capacchione, J.F., Sambuughin, N., Bina, S., Mulligan, L.P., Lawson, T.D., Muldoon, S.M., 2010. Exertional rhabdomyolysis and malignant hyperthermia in a patient with ryanodine receptor type 1 gene, L-type calcium channel alpha-1 subunit gene, and calsequestrin-1 gene polymorphisms. Anesthesiology 112 (1), 239–244. 10.1097/ALN.0b013e3181c29504.

Cech, D., Martin, S., 2012. Functional movement development across the life span, 3rd ed. Saunders, St. Louis.

Chandler, W.K., Rakowski, R.F., Schneider, M.F., 1976. Effects of glycerol treatment and maintained depolarization on charge movement in skeletal muscle. The Journal of physiology 254 (2), 285–316. 10.1113/jphysiol.1976.sp011233.

Chelu, M.G., Goonasekera, S.A., Durham, W.J., Tang, W., Lueck, J.D., Riehl, J., Pessah, I.N., Zhang, P., Bhattacharjee, M.B., Dirksen, R.T., Hamilton, S.L., 2006. Heat- and anesthesia-induced malignant hyperthermia in an RyR1 knock-in mouse. FASEB

journal: official publication of the Federation of American Societies for Experimental Biology 20 (2), 329–330. 10.1096/fj.05-4497fje.

Chen, F., Liu, Y., Sugiura, Y., Allen, P.D., Gregg, R.G., Lin, W., 2011. Neuromuscular synaptic patterning requires the function of skeletal muscle dihydropyridine receptors. Nature neuroscience 14 (5), 570–577. 10.1038/nn.2792.

Cherednichenko, G., Hurne, A.M., Fessenden, J.D., Lee, E.H., Allen, P.D., Beam, K.G., Pessah, I.N., 2004. Conformational activation of Ca2+ entry by depolarization of skeletal myotubes. PNAS 101 (44), 15793–15798. 10.1073/pnas.0403485101.

Csernoch, L., Jacquemond, V., Schneider, M.F., 1993. Microinjection of strong calcium buffers suppresses the peak of calcium release during depolarization in frog skeletal muscle fibers. The Journal of general physiology 101 (2), 297–333.

Dalgaard, P., 2008. Introductory Statistics with R, 2008th ed. Springer e-books, Berlin, Heidelberg, 1 online resource.

Dayal, A., Grabner, M., 2016. Atypical high-affinity Ca2+ binding within the pore of the mutant mammalian skeletal muscle DHPR(N617D) prevents Ca2+ permeation. Biophys. J 110 (L3629-Pos).

Dayal, A., Schrötter, K., Pan, Y., Föhr, K.J., Melzer, W., Grabner, M., 2017. The Ca2+ influx through the mammalian skeletal muscle dihydropyridine receptor is irrelevant for muscle performance. Nature communications 8 (1), 475. 10.1038/s41467-017-00629-x.

Denborough, M.A., Dennett, X., Anderson, R.M., 1973. Central-core disease and malignant hyperpyrexia. British medical journal 1 (5848), 272–273.

Di Biase, V., Franzini-Armstrong, C., 2005. Evolution of skeletal type e-c coupling: a novel means of controlling calcium delivery. The Journal of cell biology 171 (4), 695–704. 10.1083/jcb.200503077.

Dietze, B., Henke, J., Eichinger, H.M., Lehmann-Horn, F., Melzer, W., 2000. Malignant hyperthermia mutation Arg615Cys in the porcine ryanodine receptor alters voltage dependence of Ca2+ release. The Journal of physiology 526 Pt 3, 507–514.

Dirksen, R.T., 2009. Checking your SOCCs and feet: The molecular mechanisms of Ca2+ entry in skeletal muscle. The Journal of physiology 587 (13), 3139–3147. 10.1113/jphysiol.2009.172148.

Dirksen, R.T., Beam, K.G., 1999. Role of calcium permeation in dihydropyridine receptor function. Insights into channel gating and excitation-contraction coupling. The Journal of general physiology 114 (3), 393–403.

Dolphin, A.C., 2003. Beta subunits of voltage-gated calcium channels. Journal of bioenergetics and biomembranes 35 (6), 599–620.

Dolphin, A.C., 2013. The alpha2delta subunits of voltage-gated calcium channels. Biochimica et biophysica acta 1828 (7), 1541–1549. 10.1016/j.bbamem.2012.11.019.

Donatelli, R. (Ed.), 2007. Sports-specific rehabilitation. Churchill Livingstone/Elsevier, St. Louis, Mo.

Dörrscheidt-Käfer, M., 1976. The action of Ca2+, Mg2+ and H+ on the contraction threshold of frog skeletal muscle. Pflügers Archiv 362 (1), 33–41. 10.1007/BF00588678.

Dowling, J.J., Lawlor, M.W., Dirksen, R.T., 2014. Triadopathies: an emerging class of skeletal muscle diseases. Neurotherapeutics: the journal of the American Society for Experimental NeuroTherapeutics 11 (4), 773–785. 10.1007/s13311-014-0300-3.

Dulhunty, A.F., Gage, P.W., 1989. Effects of cobalt, magnesium, and cadmium on contraction of rat soleus muscle. Biophysical Journal 56 (1), 1–14. 10.1016/S0006-3495(89)82647-5.

Edwards, J.N., Friedrich, O., Cully, T.R., Wegner, F. von, Murphy, R.M., Launikonis, B.S., 2010. Upregulation of store-operated Ca2+ entry in dystrophic mdx mouse muscle. American journal of physiology. Cell physiology 299 (1), C42-50. 10.1152/ajpcell.00524.2009.

El-Hayek, R., Antoniu, B., Wang, J., Hamilton, S.L., Ikemoto, N., 1995. Identification of Calcium Release-triggering and Blocking Regions of the II-III Loop of the Skeletal Muscle Dihydropyridine Receptor. J. Biol. Chem. 270 (38), 22116–22118. 10.1074/jbc.270.38.22116.

Endo, M., 2009. Calcium-induced calcium release in skeletal muscle. Physiological reviews 89 (4), 1153–1176. 10.1152/physrev.00040.2008.

Endo, M., Tanaka, M., Ogawa, Y., 1970. Calcium Induced Release of Calcium from the Sarcoplasmic Reticulum of Skinned Skeletal Muscle Fibres. Nature 228 (5266), 34–36. 10.1038/228034a0.

Endo, M., Yagi, S., Ishizuka, T., Horiuti, K., Koga, Y., Amaha, K., 1983. Changes in the Ca-induced Ca release mechanism in the sarcoplasmic reticulum on the muscle from a patient with malignant hyperthermia. Biomed. Res. 4 (1), 83–92. 10.2220/biomedres.4.83.

Ferreira Gregorio, J., Pequera, G., Manno, C., Ríos, E., Brum, G., 2017. The voltage sensor of excitation-contraction coupling in mammals: Inactivation and interaction with Ca2+. The Journal of general physiology. 10.1085/jgp.201611725.

Ferreiro, A., Monnier, N., Romero, N.B., Leroy, J.-P., Bönnemann, C., Haenggeli, C.-A., Straub, V., Voss, W.D., Nivoche, Y., Jungbluth, H., Lemainque, A., Voit, T., Lunardi, J., Fardeau, M., Guicheney, P., 2002. A recessive form of central core disease, transiently presenting as multi-minicore disease, is associated with a homozygous mutation in the ryanodine receptor type 1 gene. Annals of neurology 51 (6), 750–759. 10.1002/ana.10231.

Flucher, B.E., Obermair, G.J., Tuluc, P., Schredelseker, J., Kern, G., Grabner, M., 2005. The role of auxiliary dihydropyridine receptor subunits in muscle. Journal of muscle research and cell motility 26 (1), 1–6. 10.1007/s10974-005-9000-2.

Föhr, K.J., Warchol, W., Gratzl, M., 1993. Calculation and control of free divalent cations in solutions used for membrane fusion studies. Methods in enzymology 221, 149–157.

Ford, L.E., Podolsky, R.J., 1970. Regenerative calcium release within muscle cells. Science (New York, N.Y.) 167 (3914), 58–59.

Fox, S.I., 2004. Human physiology, 8th ed. McGraw-Hill, Boston, xxv, 726.

Franzini-Armstrong, C., 1970. Studies of the triad: I. Structure of the Junction in Frog Twitch Fibers. J Cell Biol 47 (2), 488–499.

Freise, D., 2000. Absence of the gamma Subunit of the Skeletal Muscle Dihydropyridine Receptor Increases L-type Ca2+ Currents and Alters Channel Inactivation Properties. Journal of Biological Chemistry 275 (19), 14476–14481. 10.1074/jbc.275.19.14476.

Frontera, W.R., Ochala, J., 2015. Skeletal muscle: a brief review of structure and function. Calcified tissue international 96 (3), 183–195. 10.1007/s00223-014-9915-y.

Georgiou, D.K., Dagnino-Acosta, A., Lee, C.S., Griffin, D.M., Wang, H., Lagor, W.R., Pautler, R.G., Dirksen, R.T., Hamilton, S.L., 2015. Ca2+ Binding/Permeation via Calcium Channel, CaV1.1, Regulates the Intracellular Distribution of the Fatty Acid Transport Protein, CD36, and Fatty Acid Metabolism. The Journal of biological chemistry 290 (39), 23751–23765. 10.1074/jbc.M115.643544.

Ghasemi, A., Zahediasl, S., 2012. Normality tests for statistical analysis: a guide for non-statisticians. International journal of endocrinology and metabolism 10 (2), 486–489. 10.5812/ijem.3505.

Golini, L., Chouabe, C., Berthier, C., Cusimano, V., Fornaro, M., Bonvallet, R., Formoso, L., Giacomello, E., Jacquemond, V., Sorrentino, V., 2011. Junctophilin 1 and 2 proteins interact with the L-type Ca2+ channel dihydropyridine receptors (DHPRs) in skeletal muscle. The Journal of biological chemistry 286 (51), 43717–43725. 10.1074/jbc.M111.292755.

Gommans, I.M.P., Vlak, M.H.M., Haan, A. de, van Engelen, B.G.M., 2002. Calcium regulation and muscle disease. Journal of Muscle Research & Cell Motility 23 (1), 59–63. 10.1023/A:1019984714528.

González, A., Ríos, E., 1993. Perchlorate enhances transmission in skeletal muscle excitation-contraction coupling. The Journal of general physiology 102 (3), 373–421.

Gonzalez-Serratos, H., Valle-Aguilera, R., Lathrop, D.A., Garcia, M.d.C., 1982. Slow inward calcium currents have no obvious role in muscle excitation–contraction coupling. Nature 298 (5871), 292. 10.1038/298292a0.

Grabner, M., Dirksen, R.T., Suda, N., Beam, K.G., 1999. The II-III Loop of the Skeletal Muscle Dihydropyridine Receptor Is Responsible for the Bi-directional Coupling with the Ryanodine Receptor. Journal of Biological Chemistry 274 (31), 21913–21919. 10.1074/jbc.274.31.21913.

Gregg, R.G., Messing, A., Strube, C., Beurg, M., Moss, R., Behan, M., Sukhareva, M., Haynes, S., Powell, J.A., Coronado, R., Powers, P.A., 1996. Absence of the β subunit (cchb1) of the skeletal muscle dihydropyridine receptor alters expression of the α1 subunit and eliminates excitation-contraction coupling. PNAS 93 (24), 13961–13966.

Hagiwara, S., Henkart, M.P., Kidokoro, Y., 1971. Excitation—contraction coupling in amphioxus muscle cells. The Journal of physiology 219 (1), 233–251.

Hahin, R., Campbell, D.T., 1983. Simple shifts in the voltage dependence of sodium channel gating caused by divalent cations. The Journal of general physiology 82 (6), 785–805.

Hakamata, Y., Nakai, J., Takeshima, H., Imoto, K., 1992. Primary structure and distribution of a novel ryanodine receptor/calcium release channel from rabbit brain. FEBS Letters 312 (2-3), 229–235.

Hanlon, M.R., Berrow, N.S., Dolphin, A.C., Wallace, B.A., 1999. Modelling of a voltage-dependent Ca2+ channel β subunit as a basis for understanding its functional properties. FEBS Letters 445 (2-3), 366–370. 10.1016/S0014-5793(99)00156-8.

Hess, P., Tsien, R.W., 1984. Mechanism of ion permeation through calcium channels. Nature 309 (5967), 453. 10.1038/309453a0.

Hille, B., 1992. Ionic channels of excitable membranes, 2nd ed. Sinauer Associates, Sunderland, XIII, 607 str.

Hodgkin, A.L., Horowicz, P., 1960. Potassium contractures in single muscle fibres. The Journal of physiology 153 (2), 386–403.

Hoshi, T., Armstrong, C.M., 2013. C-type inactivation of voltage-gated K+ channels: pore constriction or dilation? The Journal of general physiology 141 (2), 151–160. 10.1085/jgp.201210888.

Hoshi, T., Zagotta, W.N., Aldrich, R.W., 1990a. Biophysical and molecular mechanisms of Shaker potassium channel inactivation. Science 250 (4980), 533–538. 10.1126/science.2122519.

Hoshi, T., Zagotta, W.N., Aldrich, R.W., 1990b. Two types of inactivation in Shaker K+ channels: Effects of alterations in the carboxy-terminal region. Neuron 250 (4980), 533–538. 10.1126/science.2122519.

Hu, H., Wang, Z., Wei, R., Fan, G., Wang, Q., Zhang, K., Yin, C.-c., 2015. The molecular architecture of dihydropyrindine receptor/L-type Ca2+ channel complex. Scientific reports 5, 8370. 10.1038/srep08370.

Hurne, A.M., O'Brien, J.J., Wingrove, D., Cherednichenko, G., Allen, P.D., Beam, K.G., Pessah, I.N., 2005. Ryanodine receptor type 1 (RyR1) mutations C4958S and C4961S reveal excitation-coupled calcium entry (ECCE) is independent of sarcoplasmic reticulum store depletion. The Journal of biological chemistry 280 (44), 36994–37004. 10.1074/jbc.M506441200.

Imagawa, T., Smith, J.S., Coronado, R., Campbell, K.P., 1987. Purified ryanodine receptor from skeletal muscle sarcoplasmic reticulum is the Ca2+-permeable pore of the calcium release channel. The Journal of biological chemistry 262 (34), 16636–16643.

Inoue, I., Tsutsui, I., Bone, Q., Brown, E.R., 1994. Evolution of Skeletal Muscle Excitation-Contraction Coupling and the Appearance of Dihydropyridine-Sensitive Intramembrane Charge Movement. Proceedings of the Royal Society B: Biological Sciences 255 (1343), 181–187. 10.1098/rspb.1994.0026.

Ito, K., Komazaki, S., Sasamoto, K., Yoshida, M., Nishi, M., Kitamura, K., Takeshima, H., 2001. Deficiency of triad junction and contraction in mutant skeletal muscle lacking junctophilin type 1. J Cell Biol 154 (5), 1059–1067. 10.1083/jcb.200105040.

Jacquemond, V., Csernoch, L., Klein, M.G., Schneider, M.F., 1991. Voltage-gated and calcium-gated calcium release during depolarization of skeletal muscle fibers. Biophysical Journal 60 (4), 867–873. 10.1016/S0006-3495(91)82120-8.

Jiang, Y.-H., Klein, M.G., Schneider, M.F., 1999. Numerical Simulation of Ca2+ “Sparks” in Skeletal Muscle. Biophysical Journal 77 (5), 2333–2357. 10.1016/S0006-3495(99)77072-4.

Jungbluth, H., 2007. Central core disease. Orphanet journal of rare diseases 2, 25. 10.1186/1750-1172-2-25.

Jurkat-Rott, K., McCarthy, T., Lehmann-Horn, F., 2000. Genetics and pathogenesis of malignant hyperthermia. Muscle & nerve 23 (1), 4–17.

Kabacoff, R.I., 2015. R in action: Data analysis and graphics with R. Manning, Shelter Island, NY, xxviii, 579.

Kanzaki, K., Watanabe, D., Kuratani, M., Yamada, T., Matsunaga, S., Wada, M., 2017. Role of calpain in eccentric contraction-induced proteolysis of Ca2+-regulatory proteins and force depression in rat fast-twitch skeletal muscle. Journal of applied physiology (Bethesda, Md.: 1985) 122 (2), 396–405. 10.1152/japplphysiol.00270.2016.

Kawana, Y., Iino, M., Horiuti, K., Matsumura, N., Ohta, T., Matsui, K., Endo, M., 1992. Acceleration in calcium-induced calcium release in the biopsied muscle fibers from patients with malignant hyperthermia. Biomed. Res. 13 (4), 287–297. 10.2220/biomedres.13.287.

Kirsch, G.E., Pascual, J.M., Shieh, C.C., 1995. Functional role of a conserved aspartate in the external mouth of voltage-gated potassium channels. Biophysical Journal 68 (5), 1804–1813. 10.1016/S0006-3495(95)80357-7.

Klein, M.G., Simon, B.J., Szucs, G., Schneider, M.F., 1988. Simultaneous recording of calcium transients in skeletal muscle using high- and low-affinity calcium indicators. Biophysical Journal 53 (6), 971–988. 10.1016/S0006-3495(88)83178-3.

Kugler, G., Weiss, R.G., Flucher, B.E., Grabner, M., 2004. Structural requirements of the dihydropyridine receptor alpha1S II-III loop for skeletal-type excitation-contraction coupling. The Journal of biological chemistry 279 (6), 4721–4728. 10.1074/jbc.M307538200.

Kurebayashi, N., Ogawa, Y., 2001. Depletion of Ca2+ in the sarcoplasmic reticulum stimulates Ca2+ entry into mouse skeletal muscle fibres. The Journal of physiology 533 (1), 185–199. 10.1111/j.1469-7793.2001.0185b.x.

Lamb, G.D., Junankar, P.R., Stephenson, D.G., 1995. Raised intracellular Ca2+ abolishes excitation-contraction coupling in skeletal muscle fibres of rat and toad. The Journal of physiology 489 (Pt 2), 349–362.

Lanner, J.T., Georgiou, D.K., Joshi, A.D., Hamilton, S.L., 2010. Ryanodine receptors: structure, expression, molecular details, and function in calcium release. Cold Spring Harbor perspectives in biology 2 (11), a003996. 10.1101/cshperspect.a003996.

Launikonis, B.S., Stephenson, D.G., Friedrich, O., 2009. Rapid Ca2+ flux through the transverse tubular membrane, activated by individual action potentials in mammalian skeletal muscle. The Journal of physiology 587 (Pt 10), 2299–2312. 10.1113/jphysiol.2009.168682.

Laver, D.R., Baynes, T.M., Dulhunty, A.F., 1997. Magnesium Inhibition of Ryanodine-Receptor Calcium Channels: Evidence for Two Independent Mechanisms. Journal of Membrane Biology 156 (3), 213–229. 10.1007/s002329900202.

Lee, C.S., Dagnino-Acosta, A., Yarotskyy, V., Hanna, A., Lyfenko, A., Knoblauch, M., Georgiou, D.K., Poché, R.A., Swank, M.W., Long, C., Ismailov, I.I., Lanner, J.T., Tran,

T., Dong, K., Rodney, G.G., Dickinson, M.E., Beeton, C., Zhang, P., Dirksen, R.T., Hamilton, S.L., 2015. Ca2+ permeation and/or binding to CaV1.1 fine-tunes skeletal muscle Ca2+ signaling to sustain muscle function. Skeletal muscle 5, 4. 10.1186/s13395-014-0027-1.

Lee, E.H., Lopez, J.R., Li, J., Protasi, F., Pessah, I.N., Kim, D.H., Allen, P.D., 2004. Conformational coupling of DHPR and RyR1 in skeletal myotubes is influenced by long-range allosterism: Evidence for a negative regulatory module. American journal of physiology. Cell physiology 286 (1), C179-89. 10.1152/ajpcell.00176.2003.

Liu, Y., Holmgren, M., Jurman, M.E., Yellen, G., 1997. Gated Access to the Pore of a Voltage-Dependent K+ Channel. Neuron 19 (1), 175–184. 10.1016/S0896-6273(00)80357-8.

Lopez-Barneo, J., Hoshi, T., Heinemann, S.H., Aldrich, R.W., 1993. Effects of external cations and mutations in the pore region on C-type inactivation of Shaker potassium channels. Receptors & channels 1 (1), 61–71.

Lüttgau, H.C., Spiecker, W., 1979. The effects of calcium deprivation upon mechanical and electrophysiological parameters in skeletal muscle fibres of the frog. The Journal of physiology 296 (1), 411–429. 10.1113/jphysiol.1979.sp013013.

Lynch, P.J., Tong, J., Lehane, M., Mallet, A., Giblin, L., Heffron, J.J., Vaughan, P., Zafra, G., MacLennan, D.H., McCarthy, T.V., 1999. A mutation in the transmembrane/luminal domain of the ryanodine receptor is associated with abnormal Ca2+ release channel function and severe central core disease. Proceedings of the National Academy of Sciences of the United States of America 96 (7), 4164–4169.

MacLennan, D.H., Duff, C., Zorzato, F., Fujii, J., Phillips, M., Korneluk, R.G., Frodis, W., Britt, B.A., Worton, R.G., 1990. Ryanodine receptor gene is a candidate for predisposition to malignant hyperthermia. Nature 343 (6258), 559–561. 10.1038/343559a0.

MacLennan, D.H., Zvaritch, E., 2011. Mechanistic models for muscle diseases and disorders originating in the sarcoplasmic reticulum. Biochimica et biophysica acta 1813 (5), 948–964. 10.1016/j.bbamcr.2010.11.009.

Magee, K.R., Shy, G.M., 1956. A new congenital non-progressive myopathy. Brain: a journal of neurology 79 (4), 610–621.

Manno, C., Figueroa, L., Royer, L., Pouvreau, S., Lee, C.S., Volpe, P., Nori, A., Zhou, J., Meissner, G., Hamilton, S.L., Ríos, E., 2013. Altered Ca2+ concentration, permeability and buffering in the myofibre Ca2+ store of a mouse model of malignant hyperthermia. The Journal of physiology 591 (18), 4439–4457. 10.1113/jphysiol.2013.259572.

Margreth, A., Damiani, E., Tobaldin, G., 1993. Ratio of Dihydropyridine to Ryanodine Receptors in Mammalian and Frog Twitch Muscles in Relation to the Mechanical Hypothesis of Excitation-Contraction Coupling. Biochemical and Biophysical Research Communications 197 (3), 1303–1311. 10.1006/bbrc.1993.2619.

McCoy, J.G., Nimigean, C.M., 2012. Structural correlates of selectivity and inactivation in potassium channels. Biochimica et biophysica acta 1818 (2), 272–285. 10.1016/j.bbamem.2011.09.007.

Meissner, G., 1984. Adenine nucleotide stimulation of Ca2+-induced Ca2+ release in sarcoplasmic reticulum. The Journal of biological chemistry 259 (4), 2365–2374.

Meissner, G., 1986. Ryanodine activation and inhibition of the Ca2+ release channel of sarcoplasmic reticulum. The Journal of biological chemistry 261 (14), 6300–6306.

Meissner, G., 1994. Ryanodine receptor/Ca2+ release channels and their regulation by endogenous effectors. Annual review of physiology 56, 485–508. 10.1146/annurev.ph.56.030194.002413.

Melzer, W., 2013. Skeletal muscle fibers: Inactivated or depleted after long depolarizations? The Journal of general physiology 141 (5), 517–520. 10.1085/jgp.201310997.

Melzer, W., Herrmann-Frank, A., Lüttgau, H.C., 1995. The role of Ca2+ ions in excitation-contraction coupling of skeletal muscle fibres. Biochimica et biophysica acta 1241 (1), 59–116.

Melzer, W., Schneider, M.F., Simon, B.J., Szucs, G., 1986. Intramembrane charge movement and calcium release in frog skeletal muscle. The Journal of physiology 373, 481–511.

Menezes-Rodrigues, F.S., Pires-Oliveira, M., Duarte, T., Paredes-Gamero, E.J., Chiavegatti, T., Godinho, R.O., 2013. Calcium influx through L-type channels attenuates skeletal muscle contraction via inhibition of adenylyl cyclases. European journal of pharmacology 720 (1-3), 326–334. 10.1016/j.ejphar.2013.10.009.

Mickelson, J.R., Louis, C.F., 1996. Malignant hyperthermia: excitation-contraction coupling, Ca2+ release channel, and cell Ca2+ regulation defects. Physiological reviews 76 (2), 537–592.

Murphy, R.M., Dutka, T.L., Horvath, D., Bell, J.R., Delbridge, L.M., Lamb, G.D., 2013. Ca2+-dependent proteolysis of junctophilin-1 and junctophilin-2 in skeletal and cardiac muscle. The Journal of physiology 591 (3), 719–729. 10.1113/jphysiol.2012.243279.

Murray, B.E., Froemming, G.R., Maguire, P.B., Ohlendieck, K., 1998. Excitation-contraction-relaxation cycle: role of Ca2+-regulatory membrane proteins in normal, stimulated and pathological skeletal muscle (review). Int J Mol Med. 10.3892/ijmm.1.4.677.

Nagai, T., Takauji, M., Kosaka, I., Tsutsu-ura, M., 1979. Biphasic time course of inactivation of potassium contractures in single twitch muscle fibers of the frog. The Japanese journal of physiology 29 (5), 539–549.

Nakai, J., Dirksen, R.T., Nguyen, H.T., Pessah, I.N., Beam, K.G., Allen, P.D., 1996. Enhanced dihydropyridine receptor channel activity in the presence of ryanodine receptor. Nature 380 (6569), 72–75. 10.1038/380072a0.

Nakai, J., Imagawa, T., Hakamata, Y., Shigekawa, M., Takeshima, H., Numa, S., 1990. Primary structure and functional expression from cDNA of the cardiac ryanodine receptor/calcium release channel. FEBS Letters 271 (1-2), 169–177.

Nakai, J., Sekiguchi, N., Rando, T.A., Allen, P.D., Beam, K.G., 1998a. Two regions of the ryanodine receptor involved in coupling with L-type Ca2+ channels. The Journal of biological chemistry 273 (22), 13403–13406.

Nakai, J., Tanabe, T., Konno, T., Adams, B., Beam, K.G., 1998b. Localization in the II-III loop of the dihydropyridine receptor of a sequence critical for excitation-contraction coupling. The Journal of biological chemistry 273 (39), 24983–24986.

Obermair, G.J., Kugler, G., Baumgartner, S., Tuluc, P., Grabner, M., Flucher, B.E., 2005. The Ca2+ channel alpha2delta-1 subunit determines Ca2+ current kinetics in skeletal muscle but not targeting of alpha1S or excitation-contraction coupling. The Journal of biological chemistry 280 (3), 2229–2237. 10.1074/jbc.M411501200.

Ohta, T., Endo, M., Nakano, T., Morohoshi, Y., Wanikawa, K., Ohga, A., 1989. Ca-induced Ca release in malignant hyperthermia-susceptible pig skeletal muscle. The American journal of physiology 256 (2 Pt 1), C358-67. 10.1152/ajpcell.1989.256.2.C358.

Otsu, K., Willard, H.F., Khanna, V.K., Zorzato, F., Green, N.M., MacLennan, D.H., 1990. Molecular cloning of cDNA encoding the Ca2+ release channel (ryanodine receptor) of rabbit cardiac muscle sarcoplasmic reticulum. The Journal of biological chemistry 265 (23), 13472–13483.

Paolini, C., Fessenden, J.D., Pessah, I.N., Franzini-Armstrong, C., 2004. Evidence for conformational coupling between two calcium channels. Proceedings of the National Academy of Sciences of the United States of America 101 (34), 12748–12752. 10.1073/pnas.0404836101.

Pape, P.C., Jong, D.S., Chandler, W.K., 1995. Calcium release and its voltage dependence in frog cut muscle fibers equilibrated with 20 mM EGTA. The Journal of general physiology 106 (2), 259–336.

Pape, P.C., Jong, D.S., Chandler, W.K., 1998. Effects of partial sarcoplasmic reticulum calcium depletion on calcium release in frog cut muscle fibers equilibrated with 20 mM EGTA. The Journal of general physiology 112 (3), 263–295.

Paredes, R.M., Etzler, J.C., Watts, L.T., Zheng, W., Lechleiter, J.D., 2008. Chemical calcium indicators. Methods 46 (3), 143–151. 10.1016/j.ymeth.2008.09.025.

Perni, S., Lavorato, M., Beam, K.G., 2017. De novo reconstitution reveals the proteins required for skeletal muscle voltage-induced Ca2+ release. Proceedings of the National Academy of Sciences of the United States of America 114 (52), 13822–13827. 10.1073/pnas.1716461115.

Perozo, E., MacKinnon, R., Bezanilla, F., Stefani, E., 1993. Gating currents from a nonconducting mutant reveal open-closed conformations in Shaker K+ channels. Neuron 11 (2), 353–358. 10.1016/0896-6273(93)90190-3.

Pickering, J.D., White, E., Duke, A.M., Steele, D.S., 2009. DHPR activation underlies SR Ca2+ release induced by osmotic stress in isolated rat skeletal muscle fibers. The Journal of general physiology 133 (5), 511–524. 10.1085/jgp.200910191.

Pizarro, G., Csernoch, L., Uribe, I., Rodriguez, M., Ríos, E., 1991. The relationship between Q gamma and Ca release from the sarcoplasmic reticulum in skeletal muscle. The Journal of general physiology 97 (5), 913–947.

Pizarro, G., Fitts, R., Uribe, I., Ríos, E., 1989. The voltage sensor of excitation-contraction coupling in skeletal muscle. Ion dependence and selectivity. The Journal of general physiology 94 (3), 405–428.

Polster, A., Perni, S., Filipova, D., Moua, O., Ohrtman, J.D., Bichraoui, H., Beam, K.G., Papadopoulos, S., 2018. Junctional trafficking and restoration of retrograde signaling by the cytoplasmic RyR1 domain. The Journal of general physiology 150 (2), 293–306. 10.1085/jgp.201711879.

Pragnell, M., Waard, M. de, Mori, Y., Tanabe, T., Snutch, T.P., Campbell, K.P., 1994. Calcium channel beta-subunit binds to a conserved motif in the I-II cytoplasmic linker of the alpha 1-subunit. Nature 368 (6466), 67–70. 10.1038/368067a0.

Prakriya, M., Feske, S., Gwack, Y., Srikanth, S., Rao, A., Hogan, P.G., 2006. Orai1 is an essential pore subunit of the CRAC channel. Nature 443 (7108), 230–233. 10.1038/nature05122.

Protasi, F., Franzini-Armstrong, C., Flucher, B.E., 1997. Coordinated incorporation of skeletal muscle dihydropyridine receptors and ryanodine receptors in peripheral couplings of BC3H1 cells. The Journal of cell biology 137 (4), 859–870.

Protasi, F., Paolini, C., Nakai, J., Beam, K.G., Franzini-Armstrong, C., Allen, P.D., 2002. Multiple Regions of RyR1 Mediate Functional and Structural Interactions with α1S-Dihydropyridine Receptors in Skeletal Muscle. Biophysical Journal 83 (6), 3230–3244. 10.1016/S0006-3495(02)75325-3.

Quane, K.A., Keating, K.E., Healy, J.M., Manning, B.M., Krivosic-Horber, R., Krivosic, I., Monnier, N., Lunardi, J., McCarthy, T.V., 1994. Mutation screening of the RYR1 gene in malignant hyperthermia: detection of a novel Tyr to Ser mutation in a pedigree with associated central cores. Genomics 23 (1), 236–239. 10.1006/geno.1994.1483.

R Core Team, 2017. R: A Language and Environment for Statistical Computing. R Foundation for Statistical Computing, Vienna, Austria.

Rakowski, R.F., 1981. Immobilization of membrane charge in frog skeletal muscle by prolonged depolarization. The Journal of physiology 317, 129–148.

Ríos, E., 2010. The cell boundary theorem: A simple law of the control of cytosolic calcium concentration. The journal of physiological sciences: JPS 60 (1), 81–84. 10.1007/s12576-009-0069-z.

Ríos, E., 2018. Calcium-induced release of calcium in muscle: 50 years of work and the emerging consensus. The Journal of general physiology 150 (4), 521–537. 10.1085/jgp.201711959.

Ríos, E., Brum, G., 1987. Involvement of dihydropyridine receptors in excitation-contraction coupling in skeletal muscle. Nature 325 (6106), 717–720. 10.1038/325717a0.

Ríos, E., Figueroa, L., Manno, C., Kraeva, N., Riazi, S., 2015. The couplonopathies: A comparative approach to a class of diseases of skeletal and cardiac muscle. The Journal of general physiology 145 (6), 459–474. 10.1085/jgp.201411321.

Ríos, E., Karhanek, M., Ma, J., González, A., 1993. An allosteric model of the molecular interactions of excitation-contraction coupling in skeletal muscle. The Journal of general physiology 102 (3), 449–481.

Ríos, E., Pizarro, G., 1988. Voltage Sensors and Calcium Channels of Excitation-Contraction Coupling. Physiology 3 (6), 223–227. 10.1152/physiologyonline.1988.3.6.223.

Ríos, E., Pizarro, G., 1991. Voltage Sensor of Excitation-Contraction Coupling in Skeletal Muscle. Physiological reviews 71, 849–908.

Robin, G., Allard, B., 2013. Major contribution of sarcoplasmic reticulum Ca2+ depletion during long-lasting activation of skeletal muscle. The Journal of general physiology 141 (5), 557–565. 10.1085/jgp.201310957.

Robin, G., Allard, B., 2015. Voltage-gated Ca2+ influx through L-type channels contributes to sarcoplasmic reticulum Ca2+ loading in skeletal muscle. The Journal of physiology 593 (21), 4781–4797. 10.1113/JP270252.

Robinson, R., Carpenter, D., Shaw, M.-A., Halsall, J., Hopkins, P., 2006. Mutations in RYR1 in malignant hyperthermia and central core disease. Human mutation 27 (10), 977–989. 10.1002/humu.20356.

Rosenberg, H., Pollock, N., Schiemann, A., Bulger, T., Stowell, K., 2015. Malignant hyperthermia: a review. Orphanet journal of rare diseases 10, 93. 10.1186/s13023-015-0310-1.

Royer, L., Pouvreau, S., Ríos, E., 2008. Evolution and modulation of intracellular calcium release during long-lasting, depleting depolarization in mouse muscle. The Journal of physiology 586 (19), 4609–4629. 10.1113/jphysiol.2008.157990.

Samso, M., 2015. 3D Structure of the Dihydropyridine Receptor of Skeletal Muscle. European journal of translational myology 25 (1), 4840. 10.4081/ejtm.2015.4840.

Schneider, M.F., Chandler, W.K., 1973. Voltage Dependent Charge Movement in Skeletal Muscle: A Possible Step in Excitation–Contraction Coupling. Nature 242 (5395), 244–246. 10.1038/242244a0.

Schneider, M.F., Simon, B.J., Szucs, G., 1987. Depletion of calcium from the sarcoplasmic reticulum during calcium release in frog skeletal muscle. The Journal of physiology 392, 167–192.

Schnier, A., Lüttgau, C., Melzer, W., 1993. Role of extracellular metal cations in the potential dependence of force inactivation in skeletal muscle fibres. Journal of muscle research and cell motility 14, 565–572.

Schredelseker, J., Dayal, A., Schwerte, T., Franzini-Armstrong, C., Grabner, M., 2009. Proper restoration of excitation-contraction coupling in the dihydropyridine receptor beta1-null zebrafish relaxed is an exclusive function of the beta1a subunit. The Journal of biological chemistry 284 (2), 1242–1251. 10.1074/jbc.M807767200.

Schredelseker, J., Di Biase, V., Obermair, G.J., Felder, E.T., Flucher, B.E., Franzini-Armstrong, C., Grabner, M., 2005. The β1a subunit is essential for the assembly of dihydropyridine-receptor arrays in skeletal muscle. PNAS 102 (47), 17219–17224. 10.1073/pnas.0508710102.

Schredelseker, J., Shrivastav, M., Dayal, A., Grabner, M., 2010. Non-Ca2+-conducting Ca2+ channels in fish skeletal muscle excitation-contraction coupling. Proceedings of the National Academy of Sciences of the United States of America 107 (12), 5658–5663. 10.1073/pnas.0912153107.

Schrötter, K., Dayal, A., Grabner, M., 2016. The mammalian skeletal muscle DHPR has larger Ca2+ conductance and is phylogenetically ancient to the early ray-finned fish sterlet (Acipenser ruthenus). Cell calcium. 10.1016/j.ceca.2016.10.002.

Schuhmeier, R.P., Dietze, B., Ursu, D., Lehmann-Horn, F., Melzer, W., 2003. Voltage-Activated Calcium Signals in Myotubes Loaded with High Concentrations of EGTA. Biophysical Journal 84 (2), 1065–1078. 10.1016/S0006-3495(03)74923-6.

Schuhmeier, R.P., Melzer, W., 2004. Voltage-dependent Ca2+ fluxes in skeletal myotubes determined using a removal model analysis. The Journal of general physiology 123 (1), 33–51. 10.1085/jgp.200308908.

Sejersted, O.M., Sjøgaard, G., 2000. Dynamics and consequences of potassium shifts in skeletal muscle and heart during exercise. Physiological reviews 80 (4), 1411–1481. 10.1152/physrev.2000.80.4.1411.

Sheridan, D.C., Takekura, H., Franzini-Armstrong, C., Beam, K.G., Allen, P.D., Perez, C.F., 2006. Bidirectional signaling between calcium channels of skeletal muscle requires multiple direct and indirect interactions. Proceedings of the National Academy of Sciences of the United States of America 103 (52), 19760–19765. 10.1073/pnas.0609473103.

Shirokova, N., 1996. Ca2+ release from the sarcoplasmic reticulum compared in amphibian and mammalian skeletal muscle. The Journal of general physiology 107 (1), 1–18. 10.1085/jgp.107.1.1.

Stern, M.D., Pizarro, G., Ríos, E., 1997. Local Control Model of Excitation–Contraction Coupling in Skeletal Muscle. The Journal of general physiology 110 (4), 415–440. 10.1085/jgp.110.4.415.

Strube, C., Beurg, M., Powers, P.A., Gregg, R.G., Coronado, R., 1996. Reduced Ca2+ current, charge movement, and absence of Ca2+ transients in skeletal muscle deficient in dihydropyridine receptor beta 1 subunit. Biophysical Journal 71 (5), 2531–2543. 10.1016/S0006-3495(96)79446-8.

Sztretye, M., Yi, J., Figueroa, L., Zhou, J., Royer, L., Allen, P.D., Brum, G., Ríos, E., 2011. Measurement of RyR permeability reveals a role of calsequestrin in termination of SR Ca2+ release in skeletal muscle. The Journal of general physiology 138 (2), 231–247. 10.1085/jgp.201010592.

Takekura, H., Bennett, L., Tanabe, T., Beam, K.G., Franzini-Armstrong, C., 1994. Restoration of junctional tetrads in dysgenic myotubes by dihydropyridine receptor cDNA. Biophysical Journal 67 (2), 793–803. 10.1016/S0006-3495(94)80539-9.

Takekura, H., Franzini-Armstrong, C., 2002. The Structure of Ca2+ Release Units in Arthropod Body Muscle Indicates an Indirect Mechanism for Excitation-Contraction Coupling. Biophysical Journal 83 (5), 2742–2753. 10.1016/S0006-3495(02)75284-3.

Takekura, H., Paolini, C., Franzini-Armstrong, C., Kugler, G., Grabner, M., Flucher, B.E., 2004. Differential contribution of skeletal and cardiac II-III loop sequences to the assembly of dihydropyridine-receptor arrays in skeletal muscle. Molecular biology of the cell 15 (12), 5408–5419. 10.1091/mbc.E04-05-0414.

Takeshima, H., Nishimura, S., Matsumoto, T., Ishida, H., Kangawa, K., Minamino, N., Matsuo, H., Ueda, M., Hanaoka, M., Hirose, T., 1989. Primary structure and expression

from complementary DNA of skeletal muscle ryanodine receptor. Nature 339 (6224), 439–445. 10.1038/339439a0.

Tanabe, T., Beam, K.G., Adams, B., Niidome, T., Numa, S., 1990. Regions of the skeletal muscle dihydropyridine receptor critical for excitation-contraction coupling. Nature 346 (6284), 567–569. 10.1038/346567a0.

Tanabe, T., Beam, K.G., Powell, J.A., Numa, S., 1988. Restoration of excitation-contraction coupling and slow calcium current in dysgenic muscle by dihydropyridine receptor complementary DNA. Nature 336 (6195), 134–139. 10.1038/336134a0.

Tang, L., Gamal El-Din, T.M., Payandeh, J., Martinez, G.Q., Heard, T.M., Scheuer, T., Zheng, N., Catterall, W.A., 2014. Structural basis for Ca2+ selectivity of a voltage-gated calcium channel. Nature 505 (7481), 56–61. 10.1038/nature12775.

The European Malignant Hyperpyrexia Group, 1984. A Protocol for the Investigation of Malignant Hyperpyrexia (MH) Susceptibility. British Journal of Anaesthesia 56 (11), 1267–1269. 10.1093/bja/56.11.1267.

Tong, J., McCarthy, T.V., MacLennan, D.H., 1999. Measurement of resting cytosolic Ca2+ concentrations and Ca2+ store size in HEK-293 cells transfected with malignant hyperthermia or central core disease mutant Ca2+ release channels. The Journal of biological chemistry 274 (2), 693–702.

Tuluc, P., Molenda, N., Schlick, B., Obermair, G.J., Flucher, B.E., Jurkat-Rott, K., 2009. A CaV1.1 Ca2+ channel splice variant with high conductance and voltage-sensitivity alters EC coupling in developing skeletal muscle. Biophysical Journal 96 (1), 35–44. 10.1016/j.bpj.2008.09.027.

Ursu, D., 2004. Excitation-Contraction Coupling in a Mouse Deficient of the Dihydropyridine Receptor g1 Subunit. Dr. biol. hum., Dissertation, Medical Faculty, Ulm University, 151 pp.

Ursu, D., Schuhmeier, R.P., Freichel, M., Flockerzi, V., Melzer, W., 2004. Altered inactivation of Ca2+ current and Ca2+ release in mouse muscle fibers deficient in the DHP receptor gamma1 subunit. The Journal of general physiology 124 (5), 605–618. 10.1085/jgp.200409168.

Ursu, D., Schuhmeier, R.P., Melzer, W., 2005. Voltage-controlled Ca2+ release and entry flux in isolated adult muscle fibres of the mouse. The Journal of physiology 562 (Pt 2), 347–365. 10.1113/jphysiol.2004.073882.

Vallejo-Illarramendi, A., Toral-Ojeda, I., Aldanondo, G., López de Munain, A., 2014. Dysregulation of calcium homeostasis in muscular dystrophies. Expert reviews in molecular medicine 16, e16. 10.1017/erm.2014.17.

van Petegem, F., 2012. Ryanodine receptors: structure and function. The Journal of biological chemistry 287 (38), 31624–31632. 10.1074/jbc.R112.349068.

van Petegem, F., Clark, K.A., Chatelain, F.C., Minor, D.L., JR, 2004. Structure of a complex between a voltage-gated calcium channel beta-subunit and an alpha-subunit domain. Nature 429 (6992), 671–675. 10.1038/nature02588.

Verburg, E., Murphy, R.M., Richard, I., Lamb, G.D., 2009. Involvement of calpains in Ca2+-induced disruption of excitation-contraction coupling in mammalian skeletal muscle

fibers. American journal of physiology. Cell physiology 296 (5), C1115-22. 10.1152/ajpcell.00008.2009.

Walker, D., Waard, M. de, 1998. Subunit interaction sites in voltage-dependent Ca2+ channels: Role in channel function. Trends in Neurosciences 21 (4), 148–154. 10.1016/S0166-2236(97)01200-9.

Ward, A., Chaffman, M.O., Sorkin, E.M., 1986. Dantrolene. A review of its pharmacodynamic and pharmacokinetic properties and therapeutic use in malignant hyperthermia, the neuroleptic malignant syndrome and an update of its use in muscle spasticity. Drugs 32 (2), 130–168.

Wilkens, C.M., Kasielke, N., Flucher, B.E., Beam, K.G., Grabner, M., 2001. Excitation-contraction coupling is unaffected by drastic alteration of the sequence surrounding residues L720-L764 of the alpha 1S II-III loop. Proceedings of the National Academy of Sciences of the United States of America 98 (10), 5892–5897. 10.1073/pnas.101618098.

Wu, J., Yan, Z., Li, Z., Qian, X., Lu, S., Dong, M., Zhou, Q., Yan, N., 2016. Structure of the voltage-gated calcium channel Cav1.1 at 3.6 A resolution. Nature 537 (7619), 191–196. 10.1038/nature19321.

Wu, J., Yan, Z., Li, Z., Yan, C., Lu, S., Dong, M., Yan, N., 2015. Structure of the voltage-gated calcium channel Cav1.1 complex. Science (New York, N.Y.) 350 (6267), aad2395. 10.1126/science.aad2395.

Wu, Y.C., Tucker, T., Fettiplace, R., 1996. A theoretical study of calcium microdomains in turtle hair cells. Biophysical Journal 71 (5), 2256–2275. 10.1016/S0006-3495(96)79429-8.

Yang, J., Ellinor, P.T., Sather, W.A., Zhang, J.F., Tsien, R.W., 1993. Molecular determinants of Ca2+ selectivity and ion permeation in L-type Ca2+ channels. Nature 366 (6451), 158–161. 10.1038/366158a0.

Yang, T., Riehl, J., Esteve, E., Matthaei, K.I., Goth, S., Allen, P.D., Pessah, I.N., Lopez, J.R., 2006. Pharmacologic and Functional Characterization of Malignant Hyperthermia in the R163C RyR1 Knock-in Mouse. Anesthesiology 105 (6), 1164–1175. 10.1097/00000542-200612000-00016.

Yang, Y., Yan, Y., Sigworth, F.J., 1997. How Does the W434F Mutation Block Current in Shaker Potassium Channels? The Journal of general physiology 109 (6), 779–789.

Yellen, G., Sodickson, D., Chen, T.Y., Jurman, M.E., 1994. An engineered cysteine in the external mouth of a K+ channel allows inactivation to be modulated by metal binding. Biophysical Journal 66 (4), 1068–1075. 10.1016/S0006-3495(94)80888-4.

Zalk, R., Clarke, O.B., Des Georges, A., Grassucci, R.A., Reiken, S., Mancia, F., Hendrickson, W.A., Frank, J., Marks, A.R., 2015. Structure of a mammalian ryanodine receptor. Nature 517 (7532), 44–49. 10.1038/nature13950.

Zhang, S.L., Yu, Y., Roos, J., Kozak, J.A., Deerinck, T.J., Ellisman, M.H., Stauderman, K.A., Cahalan, M., 2005. STIM1 is a Ca2+ sensor that activates CRAC channels and migrates from the Ca2+ store to the plasma membrane. Nature 437 (7060), 902–905. 10.1038/nature04147.

Zhang, X., Xia, M., Li, Y., Liu, H., Jiang, X., Ren, W., Wu, J., DeCaen, P., Yu, F., Huang, S., He, J., Clapham, D.E., Yan, N., Gong, H., 2013. Analysis of the selectivity filter of the voltage-gated sodium channel Na(v)Rh. Cell research 23 (3), 409–422. 10.1038/cr.2012.173.

Zhang, Y., Chen, H.S., Khanna, V.K., Leon, S. de, Phillips, M.S., Schappert, K., Britt, B.A., Browell, A.K., MacLennan, D.H., 1993. A mutation in the human ryanodine receptor gene associated with central core disease. Nature genetics 5 (1), 46–50. 10.1038/ng0993-46.

Zhao, F., Li, P., Chen, S.R., Louis, C.F., Fruen, B.R., 2001. Dantrolene inhibition of ryanodine receptor Ca2+ release channels. Molecular mechanism and isoform selectivity. The Journal of biological chemistry 276 (17), 13810–13816. 10.1074/jbc.M006104200.

Zhou, H., Lillis, S., Loy, R.E., Ghassemi, F., Rose, M.R., Norwood, F., Mills, K., Al-Sarraj, S., Lane, R.J.M., Feng, L., Matthews, E., Sewry, C.A., Abbs, S., Buk, S., Hanna, M., Treves, S., Dirksen, R.T., Meissner, G., Muntoni, F., Jungbluth, H., 2010. Multi-minicore disease and atypical periodic paralysis associated with novel mutations in the skeletal muscle ryanodine receptor (RYR1) gene. Neuromuscular disorders: NMD 20 (3), 166–173. 10.1016/j.nmd.2009.12.005.

Zorzato, F., Fujii, J., Otsu, K., Phillips, M., Green, N.M., Lai, F.A., Meissner, G., MacLennan, D.H., 1990. Molecular cloning of cDNA encoding human and rabbit forms of the Ca2+ release channel (ryanodine receptor) of skeletal muscle sarcoplasmic reticulum. The Journal of biological chemistry 265 (4), 2244–2256.